

Optical Characterization of 2D Metals and Dielectric
Nano-structures via MoM-based Numerical Technique, and
Development of DCIM with Spatial Error Criterion and
Automatic Order Selection

by

Emine Pınar Karabulut

A Thesis Submitted to the
Graduate School of Engineering
in Partial Fulfillment of the Requirements for
the Degree of

Doctorate of Philosophy

in

Electrical & Electronics Engineering

Koç University

December, 2011

Koç University
Graduate School of Sciences and Engineering

This is to certify that I have examined this copy of a doctoral dissertation by

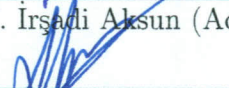
Emine Pınar Karabulut

and have found that it is complete and satisfactory in all respects,
and that any and all revisions required by the final
examining committee have been made.

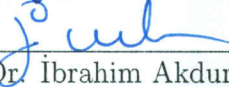
Committee Members:



Prof. Dr. M. İrsadi Aksun (Advisor)



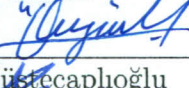
Assoc. Prof. Dr. Alper T. Erdoğan (Advisor)



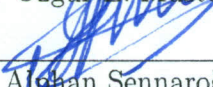
Prof. Dr. İbrahim Akduman



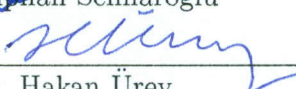
Assoc. Prof. Dr. Vakur Ertürk



Assoc. Prof. Dr. Özgür E. Müstecaplıoğlu



Prof. Dr. Alphan Sennaroğlu



Prof. Dr. Hakan Ürey

Date: January 12, 2012

To my family

Abstract

The main goal in this study is to develop an efficient and accurate numerical technique that could help to simulate and analyze two-dimensional nano-structures in multilayered environment in the optical regime. Since the Method of Moments (MoM) has been one of the most widely-used numerical techniques for electromagnetic problems in layered open environment, it has been employed in this study as the main numerical tool that the development is based on. As the MoM solves mixed-potential integral equations in electromagnetic and optic problems, it translates the integral equations into a set of algebraic equations by expanding the unknown functions under the integral sign into a series of known functions with unknown coefficients, referred to as basis functions. It should be remembered that converting governing differential equations into integral equations requires the knowledge of Green's functions, which is the response of the medium of interest to a point source. In this endeavor, there are couple of computational difficulties that need to be overcome, which are mainly in the computations of Green's functions in multilayered media via Discrete Complex Image Method (DCIM), and in the computations of the entries of resulting algebraic equations, i.e., MoM matrix entries. In this thesis, primarily these difficulties have been addressed properly and their efficient and robust remedies have been proposed, demonstrated and verified.

Before providing some more details on the contributions in this thesis, it should be remembered that the performance of the MoM for the problems in layered media is strongly dependent on the accurate and efficient evaluation of the spatial-domain

Green's functions in layered media. Although the DCIM has eliminated some of the major bottlenecks in the efficient computation of Green's function in the spatial domain, there still exist two hurdles that render the DCIM not robust and reliable to be employed in the development of CAD tools for EM and optics simulations, which are namely the lack of a spatial-domain error metric assuring the accuracy of the end result and an automatic order selection algorithm finding the optimum number of complex images. Therefore, in the first part of the dissertation, covering the first two chapters, these two remaining issues in the core of the original and improved DCIMs have been discussed, and theoretically sound, easy-to-implement and computationally efficient novel remedies have been proposed, developed and demonstrated. As a result of these improvements, the DCIM is now ready to be used, not only in the calculations of Green's functions but also in the evaluations of Fourier, Laplace and Hankel transformations, accurately and reliably in commercial softwares.

As it was stated in the opening sentence, the ultimate goal is to develop an efficient, accurate and robust algorithm for the analysis of 2D metal and dielectric nano-structures in multilayered media. In the last part of the dissertation, a novel MoM-based approach has been proposed and developed for the analysis of such structures in free space. The main power of the developed method is that it provides a closed-form expression for a generic matrix entry of the MoM, and, without referring to any numerical integration algorithms, all matrix entries can be obtained by a simple evaluation of the closed-form expression at the location of the point of interest. Although this method can be extended to multilayered environment in a straightforward manner by considering each term in the closed-form approximation of the Green's function as the Green's function in free space with complex source location, this part has been left for the future study because of its numerical inefficiency.

ÖZETÇE

Bu çalışmanın esas amacı, optik frekanslarda çok katmanlı ortama gömülü iki-boyuttaki yapıların gerçekleştirilmesini ve analizini yapmaya yardımcı olabilecek verimli ve doğru bir sayısal yöntem geliştirmektir. Momentler yöntemi (MoM) özellikle katmanlı açık ortamlardaki elektromanyetik problemler için en çok tercih edilen tekniklerden biri olduğundan, bu çalışmada temel sayısal yöntem olarak MoM kullanılmıştır. Elektromanyetik ve optik problemlerde, karışık-potansiyel-integral denklemleri MoM ile çözülürken, söz konusu integral denklemleri bir takım cebirsel denklemlere dönüştürülür. Bu da; integralin içindeki bilinmeyen fonksiyonu, başında bilinmeyen katsayılar bulunan bilinen fonksiyonlar (taban fonksiyonları) cinsinden tanımlayarak gerçekleştirilir. Hatırlanmalıdır ki, problemin türevsel denklemlerinin integral denklemlerine dönüşmesi ancak ortamın Green fonksiyonunu bilerek mümkün olabilir. Green fonksiyon ise basitçe o ortamın noktasal bir kaynağa verdiği yanıt olarak tanımlanabilir. Yukarıda belirtilen amaca ulaşmak için aşılması gereken bir takım önemli sayısal zorluklar bulunmaktadır. Bunlardan ilki ayrık karmaşık imaj yöntemi (DCIM) ile katmanlı-yapı Green fonksiyonlarının, ikincisi ise MoM cebirsel denklemlerinin yani MoM matrisi elemanlarının doğru ve verimli bir şekilde hesaplanmasıdır. Bu tezde söz konusu zorluklar doğru bir şekilde tanımlanmış ve çözülmüştür.

Bu çalışmanın getirdiği katkılar hakkındaki detaylardan bahsetmeden önce, hatırlanmalıdır ki katmanlı yapılarda MoM'nin performansı uzamsal-bölge katmanlı-yapı Green fonksiyonlarının verimli bir şekilde hesaplanmasına bağlıdır. DCIM uzamsal-bölge katmanlı-yapı Green fonksiyonlarının hesaplanmasında bir çok problemi el-

emiş olsa da, DCIM'nin elektromanyetik ve optik simülasyon programlarında kullanılmasından kaçınılmasına sebep olan iki önemli eksiği bulunmaktadır. Bu problemlerin ilki, çıkan sonucun doğruluğunu gösteren uzamsal alanda tanımlı bir hata ölçütünün yokluğu ve ikincisi de en iyi karmaşık imaj sayısını veren otomatik bir algoritmanın bulunmayışıdır. Bu sebeple, tezin ilk iki bölümünde DCIM'nin ortaya atıldığından beri cevap bulunamamış bu iki problemi tartışılmış, sağlam bir teoriye oturtulmuş ve kolay gerçekleştirilebilen verimli yeni bir DCIM sunulmuştur. Sonuç olarak bu gelişmelerle DCIM, sadece Green fonksiyonların hesaplanması değil aynı zamanda Fourier, Laplace ve Hankel dönüşümlerini de doğru bir şekilde yapmaya hazır hale gelmiştir.

İlk cümlede belirtildiği gibi, bu çalışmanın en üst düzeydeki amacı çok katmanlı bir ortama gömülü iki-boyuttaki yalıtkan ve metal yapıların analizi için verimli, doğru ve güvenilir bir sayısal yöntem geliştirmektir. Tezin son bölümünde MoM'ye dayalı yeni bir yöntem, boşlukta uzanan iki-boyuttaki yalıtkan ve metal yapıların analizi için önerilmektedir. Geliştirilen yöntemin başarısı genel bir MoM matrisi elemanı için kapalı-biçimde bir ifade bulunmuş olmasından ileri gelmektedir. Yani herhangi bir integral alma işlemi yapmadan tüm matris elemanları bu kapalı-biçimdeki ifadenin hesaplanması ile bulunabilir. Green fonksiyonun kapalı-biçim yaklaşımının her bir terimini, kaynağı karmaşık konumda olan boşluk Green fonksiyonu olarak düşünürsek, önerdiğimiz yöntem çok katmanlı ortamdaki yapıların analizi için genişletilebilir. Ancak şu anki durumuyla sayısal olarak verimsiz olduğu görüldüğünden bu kısım gelecek bir araştırma konusu olarak bırakılmıştır.

Acknowledgments

I am deeply indebted to my supervisor M. İrşadi Aksun for his enthusiasm, creativity, kindness and endless patience. Throughout my thesis study, he shared his valuable experience and provided me a perfect work environment, sound advise and inspiration. Furthermore it is a pleasure to thank my co-advisor Alper T. Erdoğan whose stimulating suggestions and ideas helped me in all the time of my research. It was a great pleasure to work with them.

I would like to thank my thesis committee İbrahim Akduman, Özgür Müstecaplıoğlu and Hakan Ürey and the other two members of my oral defense committee Vakur Ertürk and Alphan Sennaroğlu for their time, sincere interest and suggestions. Likewise, I would like to thank Lale Alatan for her guidance and valuable comments.

I would send my deepest gratitude to my parents and my sister Deniz for their unflagging love and tireless support throughout my life. I would not be the person that I am without the perfect combination of the encouragement and constructive criticism they always gave me.

I heartily wish to thank Ahmet Cihat for being my backbone and making me a more optimistic and happier person. His support especially during the most challenging period of my thesis study is so appreciated.

My thanks also go to my friends and colleagues Aytaç Alparslan, Engin Çetin, Gökçen Mahmutoğlu and Ozan Yıldırım for their immensely valuable support.

Finally I would like to thank Dostoyevsky, Oğuz Atay and Werner Herzog for their genius that took me into the different human minds and worlds and relieved me of the stress during hard times associated with my research.

Table of Contents

List of Tables	xii
List of Figures	xiv
Nomenclature	xx
Chapter 1: Introduction	1
1.1 Contributions	10
Chapter 2: Discrete Complex Image Method with Spatial Error Criterion	12
2.1 Introduction	12
2.2 Overview of DCIM	14
2.3 Connection Between Spectral- and Spatial-Domain Errors	20
2.3.1 Parseval-like identity for Deformed Paths	21
2.3.2 Practical Application	24
2.3.3 DCIM with Spatial Error Criterion	28
2.3.4 Improvement for the Multilevel DCIM	30
2.4 Numerical Examples and Discussions	31
2.4.1 Link between spectral- and spatial-domains	31
2.4.2 Verification of the proposed method	34
2.4.3 More about the leakage	37

2.5	Conclusion	40
Chapter 3: Discrete Complex Image Method with Automatic Order Selection		42
3.1	Introduction	42
3.2	Model Selection	44
3.3	DCIM with Model Order Selection	52
3.3.1	Brief Overview of DCIM	52
3.3.2	Automatic Order Selection for DCIM	54
3.4	Results and Discussions	58
3.5	Conclusion	72
Chapter 4: A Novel MoM-based Approach for Accurate and Efficient Analysis of 2D Structures		75
4.1	Introduction	75
4.2	The Method of Moments	78
4.3	Theory and General Formulation in Free Space	80
4.4	MoM Analysis of 2D structures	82
4.4.1	TM Mode	83
4.4.2	TE Mode	90
4.4.3	Field Calculation	99
4.5	Numerical Examples and Discussions	103
4.6	Conclusion	112
Chapter 5: Conclusion and Recommendations for Future Work		118
Appendices		123
Appendix A: Derivations of the second EFIE for the TE mode excitation		123

Appendix B: A Novel Approach for Fast Evaluation of Infinite Sum-	
mations	128
B.1 Abstract	128
B.2 Introduction	128
B.3 Theory of the Method	130
B.4 Numerical Results	132
B.5 Conclusion	134
Bibliography	135
Vita	145

List of Tables

2.1	Error and energy (E) of the spatial- and spectral-domain Green's functions estimated by the standard and proposed 3-level DCIM for <i>Case-1</i> .	32
2.2	Error and energy (E) of the spatial- and spectral-domain Green's functions estimated by the standard and proposed 3-level DCIM for <i>Case-2</i> .	33
3.1	Order selection for the 3-level DCIM for the geometry in Fig. 3.8. $f = 4.075 \text{ GHz}$, $\sigma_{PRE} = 10^3 \sigma_{MDL}$.	63
3.2	Order selection for the 3-level DCIM for the geometry in Fig. 3.8. $f = 3 \text{ GHz}$, $\sigma_{PRE} = 10^3 \sigma_{MDL}$.	63
3.3	Order selection for the 3-level DCIM for the geometry in Fig. 3.11. $f = 30 \text{ GHz}$, $\sigma_{PRE} = 10^3 \sigma_{MDL}$.	65
3.4	Order selection for the 3-level DCIM for the geometry in Fig. 3.13. $f = 10 \text{ GHz}$, $\sigma_{PRE} = \sqrt{10} \sigma_{MDL}$ when SWPs are not extracted, $\sigma_{PRE} = 10^3 \sigma_{MDL}$ when SWPs are extracted.	68
3.5	Order selection for the 3-level DCIM for the geometry in Fig. 3.15. $f = 4 \text{ GHz}$, $\sigma_{PRE} = \sqrt{10} \sigma_{MDL}$ when SWPs are not extracted, $\sigma_{PRE} = 10^3 \sigma_{MDL}$ when SWPs are extracted.	70
B.1	The performance comparison of the proposed method and direct summation for 1-D infinite summation with regard to CPU-time.	133

B.2	The performance comparison of the proposed method and the Ewald method for the evaluation of FSPGF with regard to CPU-time. . . .	134
-----	---	-----

List of Figures

2.1	A general multi-layer planar medium	15
2.2	Paths for approximation for 3-level DCIM on the complex (a) k_z plane and (b) k_ρ plane.	17
2.3	A lossy material in air. The locations of the observation and the horizontal electric dipole (HED) are at the interface between the air and the upper boundary of the dielectric layer.	26
2.4	Integration path for the 3-level DCIM on complex k_ρ -plane.	27
2.5	Spatial-domain weighted energy and its estimates via three different metrics.	28
2.6	The magnitude of the spatial-domain Green's function for the vector potential obtained by a) the standard DCIM and b) the proposed DCIM. The numerical integration result is presented for verification. Parameters of the geometry are given in Fig. 2.3 and the frequency of operation is 4 GHz.	36
2.7	The magnitude of the spatial-domain Green's function for the vector potential. Parameters of the geometry are given in Fig. 2.3 and the frequency of operation is 4 GHz.	37
2.8	The magnitude of the spatial-domain Green's function for the vector potential. Parameters of the geometry are given in Fig. 2.3 and the frequency of operation is 4 GHz.	38

2.9	Demonstration of the Leakage: Leakage from Region-2 to Region-1, Leakage from Region-3 to Region-2 and to Region-1, the region specific errors and the overall error for the standard DCIM. Parameters of the geometry are given in Fig. 2.3 and the frequency of operation is 4 GHz.	39
3.1	Third order polynomial with and without noise. Noise is iid gaussian with zero mean and $\sigma^2 = 0.01$	49
3.2	Description length vs. polynomial order. Minimum description length is achieved at $r = 3$.	50
3.3	$f(x) = \cos(0.5x) + \cos(3x)$. Normally distributed iid noise with zero mean and $\sigma^2 = 0.005$	51
3.4	Average description length vs. number of exponentials. Minimum description length appears at $r = 4$ as expected.	51
3.5	$f(x) = \cos(0.5x) + \cos(3x) + e^{5x}$. Normally distributed iid noise with zero mean and $\sigma^2 = 0.005$	52
3.6	Average description length vs. number of exponentials. Minimum description length appears at $r = 5$.	53
3.7	A general multilayer planar medium	53
3.8	Geometry for Example-1 and Example-2. A PEC backed lossless dielectric material in free space.	61
3.9	Magnitudes of the Green's functions of a) the vectoral potential for $\mathbf{r}_{PRE} = (1, 2, 4)$; and b) the scalar potential for $\mathbf{r}_{PRE} = (1, 1, 2)$, for the geometry in Fig. 3.8. $f = 4.075GHz$, $\sigma_{PRE} = 10^3\sigma_{MDL}$.	62
3.10	Magnitude of the Green's functions of a) the vectoral potential for $\mathbf{r}_{PRE} = (9, 2, 6)$; and b) the scalar potential for $\mathbf{r}_{PRE} = (6, 3, 1)$, for the geometry in Fig. 3.8. $f = 3.0 GHz$, $\sigma_{PRE} = 10^3\sigma_{MDL}$.	64
3.11	Geometry for Example-3. A lossless PEC backed material.	65

3.12	Magnitude of the Green's functions of a) the vector potential for $\mathbf{r}_{PRE} = (7, 4, 6)$; and b) the scalar potential for $\mathbf{r}_{PRE} = (7, 2, 10)$, for the geometry in Fig. 3.11 . $f = 30 GHz$, $\sigma_{PRE} = 10^3\sigma_{MDL}$	66
3.13	Geometry for Example-4. A lossy PEC backed material.	67
3.14	Magnitude of the Green's functions of a) the vector potential for $\mathbf{r}_{PRE} = (7, 4, 5)$; and b) the scalar potential for $\mathbf{r}_{PRE} = (11, 3, 11)$, for the geometry in Fig. 3.13. $f = 10 GHz$, $\sigma_{PRE} = 10^3\sigma_{MDL}$	69
3.15	Geometry for Example-5. A lossy material in air.	70
3.16	Magnitude of the Green's functions of a) the vector potential for $\mathbf{r}_{PRE} = (7, 5, 10)$; and b) the scalar potential for $\mathbf{r}_{PRE} = (8, 2, 7)$, for the geometry in Fig. 3.15. $f = 4.0 GHz$, $\sigma_{PRE} = 10^3\sigma_{MDL}$	71
3.17	Relative error in g_{xx}^A (example-3) introduced by the choice of different error parameters σ as compared to the parameter provided by the algorithm itself. $\mathbf{r}_{MDL} = (18, 3, 14)$, and $\mathbf{r}_{PRE} = (12, 5, 7)$ for $\sigma_{PRE} = 10\sigma_{MDL}$, $\mathbf{r}_{PRE} = (11, 3, 8)$ for $\sigma_{PRE} = 10^2\sigma_{MDL}$ and $\mathbf{r}_{PRE} = (7, 5, 10)$ for $\sigma_{PRE} = 10^3\sigma_{MDL}$	73
4.1	A single dielectric rod in a background medium of free-space extending in z direction. The direction of electric and magnetic fields are shown for <i>TE</i> and <i>TM</i> mode excitations.	83
4.2	A line source at the origin	86
4.3	Basis and testing functions selected for the MoM application.	90
4.4	The finite PhC consisting of 25 square lattice of dielectric columns with relative permittivity $\epsilon_r = 8$, the lattice constant $a = 400nm$ and the width of a dielectric column $d = 120nm$. The PhC is excited by the plane waves in TM and TE mode and the resulting fields are calculated for the cross-section shown as a line.	104

4.5	Magnitude of the field in z -direction due to the normal incident TM mode plane wave at 500 THz. The field is calculated over the finite photonic crystal shown in Fig. 4.4. The PhC covers the region from 0 to $1.72 \times 10^{-6}m$, which is demonstrated as an additional grid on x	105
4.6	Magnitude of the fields in $a)$ y -direction and $b)$ x -direction due to the normal incident TE mode plane wave at 500 THz. The field is calculated over the finite photonic crystal shown in Fig. 4.4. The PhC covers the region from 0 to $1.72 \times 10^{-6}m$, which is demonstrated as an additional grid on x	106
4.7	Magnitude of the field in z -direction due to the oblique incident TM mode plane wave at 500 THz with $\theta = 15$. The field is calculated over the finite photonic crystal shown in Fig. 4.4. The PhC covers the region from 0 to $1.72 \times 10^{-6}m$, which is demonstrated as an additional grid on x	107
4.8	Magnitude of the fields in $a)$ y -direction and $b)$ x -direction due to the oblique incident TE mode plane wave at 500 THz with $\theta = 15$. The field is calculated over the finite photonic crystal shown in Fig. 4.4. The PhC covers the region from 0 to $1.72 \times 10^{-6}m$, which is demonstrated as an additional grid on x	108
4.9	The finite PhC with defect consisting of 24 square lattice of dielectric columns with relative permittivity $\epsilon_r = 8$, the lattice constant $a = 400nm$ and the width of a dielectric column $d = 120nm$. The defect is introduced by removing the central dielectric column. The PhC is excited by the plane waves in TM and TE mode and the resulting fields are calculated for the cross-section shown as a line.	109

4.10	Magnitude of the field in z -direction due to the normal incident TM mode plane wave at 500 THz. The field is calculated over the finite photonic crystal with defect shown in Fig. 4.9. The PhC covers the region from 0 to $1.72 \times 10^{-6}m$, which is demonstrated as an additional grid on x	109
4.11	Magnitude of the fields in $a)$ y -direction and $b)$ x -direction due to the normal incident TE mode plane wave at 500 THz. The field is calculated over the finite photonic crystal with defect shown in Fig. 4.9. The PhC covers the region from 0 to $1.72 \times 10^{-6}m$, which is demonstrated as an additional grid on x	110
4.12	Dielectric and metallic structure in free space with the relative permittivities $\epsilon_{r1} = 4$ and $\epsilon_{r2}(Ag) = -15.91j - j0.43$ at 500 THz, respectively. The system is excited by the plane waves in TM and TE mode and the resulting fields are calculated for the cross-section shown as a line. . .	111
4.13	Magnitude of the field in z -direction due to the normal incident TM mode plane wave at 500 THz. The field is calculated over the cross-section shown as a line in Fig. 4.12. The dielectric material is between $y = 0$ and $y = 500$ nm.	112
4.14	Magnitude of the field in x and y -direction due to the normal incident TE mode plane wave at 500 THz. The field is calculated over the cross-section shown as a line in Fig. 4.12. The dielectric material is between $y = 0$ and $y = 500$ nm.	113
4.15	A metallic structure with a single slit in free space with the relative permittivity $\epsilon_r = -16.19j - j1.05$ where free-space wavelength is $\lambda_0 = 650$ nm. The width and height of the metallic bars are 200nm and $2\mu m$, respectively. The width of the slit is 80nm. The system is excited by the plane waves in TM and TE mode and the resulting fields are calculated for the cross-section shown as a line.	114

4.16	Magnitude of the field in z -direction due to the normal incident TM mode plane wave at 500 THz. The field is calculated over the cross-section shown as a line in Fig. 4.15. The slit region is demonstrated with two additional grids at the center of the figure.	115
4.17	Magnitude of the field in x and y -direction due to the normal incident TE mode plane wave at 500 THz. The field is calculated over the cross-section shown as a line in Fig. 4.15. The slit region is demonstrated with two additional grids at the center of the figure.	116
B.1	S vs. m of the summation in (B.8), where $m = 1, \dots, N_s = 43$. $S = 7.41858$ is equivalent to the zero frequency term of its complex-exponential approximation and hence the result of the summation. . .	133

Nomenclature

CAD	Computer Aided Design
CEM	Computational Electromagnetics
DCIM	Discrete Complex Image Method
EFIE	Electric Field Integral Equation
ESPRIT	Estimation of Signal Parameters via Rotational Invariant Techniques
FDTD	Finite Difference Time Domain
FEM	Finite Element Method
GPOF	Generalized Pencil of Function Method
MDL	Minimum Description Length
MoM	Method of Moments
MPIE	Mixed Potential Integral Equation
OLS	Ordinary Least Squares
PEC	Perfect Electric Conductor
PhC	Photonic Crystal
SNR	Signal to Noise Ratio
SPP	Surface Plasmon Polariton
SWP	Surface Wave Pole
TE	Transverse Electric
TM	Transverse Magnetic
WLS	Weighted Least Squares

Chapter 1

Introduction

Before the advent of digital computers, most of the analysis and design of high-frequency circuits and structures were mainly performed manually and experimentally, respectively. However, during this era, lots of analytical solutions and techniques for the analysis of such systems have been developed and, perhaps more importantly, the theoretical background of today's numerical techniques have been laid down. Once high-speed computers have been accessible by the researchers in universities and research labs, analytical solutions have been widely replaced by their numerical approximations or by more efficient but approximate numerical techniques. Therefore, with the further advancement of computers and numerical techniques, many powerful numerical analysis and design methods have been developed, and a new field of computational electromagnetics (CEM) has arisen.

The fundamental significance of CEM stems from the fact that the simulation of electromagnetic behavior of devices and structures can be achieved by CEM algorithms before they are actually built. This allows the scientists and engineers to perform any necessary optimization for the customization of design, and therefore, saves them from the laborious process of trial-and-error experimentation, being quite expensive in terms of money, manpower and time. In addition, since fast desktop or

laptop computers are far more accessible by researchers and engineers than an experimental setup nowadays, gaining insight and intuition into electromagnetic problems have become much easier through the use of computer simulations and visualizations.

Due to the extremely wide range of EM problems in engineering applications, many different CEM algorithms have been developed in years. Depending upon the application and structure, each algorithm has its own advantages and limitations. Since plenty of algorithms have been developed for different kinds of problems, their categorization may differ in terms of the aspects of interest. Mainly, these methods can be classified into two primary groups: *i*) approximate methods like quasi-static methods such as conformal mapping [1] and equivalent capacitance methods [2–4]; and *ii*) numerically exact methods, also referred to as full-wave methods, like the finite element method (FEM) [5,6], the finite-difference time-domain (FDTD) method [7,8] and the method of moments (MOM) [9,10]. As expected, the approximate methods are, in general, numerically more efficient but less accurate than the full-wave methods. Most of these numerical techniques basically transform integral, differential, or integro-differential equations into a set of algebraic equations. Note that, with today's technology of high-speed computers, full-wave methods have already become the preferred choice for the analysis of a wide range of EM problems, except for electrically very large ones. For EM problems of large size, many approximations are to be imposed on the equations of radiation and scattering to provide the tractability of the problems. Since such electrically large structures are out of the scope of this thesis, they are not discussed any further, and the focus of the study has been on the efficient implementation of full-wave methods.

Among the widely used full-wave methods, the FEM has been one of the most popular approach for the analysis of general arbitrary structures, and is conceptually simple and straightforward to implement for the solution of governing differential equations in the frequency domain. In general, the FEM is employed for the solution of frequency-domain electromagnetic scattering problems by dividing the entire volume of interest into sub-volumes, and solving the Helmholtz equation as a boundary value

problem. One of the main advantages of FEM is that it can be applied to almost any geometry such as arbitrarily shaped and inhomogeneous structures. In addition, as it is based on a differential equation, the coefficient matrix to be solved is sparse, reducing the memory usage and the solution time of the matrix equations. However, necessity for the discretization of the entire volume of interest renders the method computationally expensive and costly, especially for radiation and scattering problems of open structures.

The FDTD method is based on approximating the governing differential equations, is very straightforward to implement: the FDTD approach uses the method of finite differencing to solve Maxwell's curl equations by discretizing both time and space. The equations are solved in a cyclic manner in time by computing the electric and magnetic fields from one another. Similar to the FEM, the FDTD method is very versatile and applicable to many different electromagnetic problems. Due to the fact that the FDTD is a time-domain method, the frequency response of a structure can be obtained in one step. However, since the entire solution domain must be discretized as in the case of the FEM, the solution of the scattering problems of open geometries can take a relatively long time compared to integral equation algorithms.

In spite of the fact that the numerical procedures in the FEM and FDTD method are quite different, they share conceptual similarities as both are quite general and versatile differential equation solvers. Therefore, after the development of high speed computers, they have attracted much attention among the researchers and commercial software developers. However, both methods are not well-suited for radiation and scattering problems since these problems ideally require the discretization of an infinite region in the implementation of the FEM and FDTD methods. To circumvent this problem, one must truncate the entire domain to a limited region by introducing some artificial boundary conditions, also known as absorbing boundary conditions, without altering the boundary conditions of the original problem.

Contrary to the FEM and FDTD method, the MoM is usually used to solve integral equations in EM problems, although generally it can be used to solve the problems in

differential or integro-differential forms as well. The reason for the choice of integral equation problems is that unknown for the integral equations of EM problems are current densities while unknowns for differential equations are the fields. Since the current densities are bounded in a volume, the discretization and the computation is confined to the volume of the scatterer only, which results in fewer unknown. This property of MoM is significant especially for the analysis of open geometries since the fields in an open geometry extend to infinity which makes the domain of differential equation infinite while the bounded current densities yield a finite domain for integral equations. In general, MoM transforms an operator equation (differential, integral or integro-differential form) into a set of algebraic equations in three main steps: *i*) segmenting the structure, *ii*) expanding the unknown quantity using a set of known functions (called as the basis functions) with unknown coefficients and *iii*) enforcing the boundary conditions by defining an appropriate inner product (or also called as *moment*) between a basis function and a weighting function (or also called as the testing function). The basis functions should be coherent to the expected behavior of the unknown function throughout its domain and the testing functions should be in the range of the operator equation to model the set of equations correctly. In MoM, the contribution of each basis function affects all others with testing operation therefore the resulting matrix becomes full. Therefore calculation of the matrix elements and solution of the matrix equation must be performed efficiently for the sake of the method's performance. For small or moderate-size structures (occupying the space in several wavelengths in two dimensions) the matrix filling time dominates the CPU time, while the matrix solution time is more significant for larger geometries.

In this thesis, the main goal was to develop an efficient and accurate numerical technique that could help to simulate and analyze two-dimensional nano-structures in multilayered environment in the optical regime. Since the MoM has been one of the most widely-used and suitable numerical techniques for electromagnetic problems in layered open environment, it has been employed in this study as the main numerical tool that the development is based on. In this endeavor, there are couple of

computational difficulties that need to be overcome, which are mainly in the computations of Green's functions in multilayered media via Discrete Complex Image Method (DCIM), and in the computations of the entries of resulting algebraic equations, i.e., MoM matrix entries. In this thesis, primarily these difficulties have been addressed properly and their efficient and robust remedies have been proposed, demonstrated and verified.

For the MoM formulation in EM, Green's functions play an important role as they are required to transform governing wave equations to the integral equations. For the rigorous analysis of planar layered structures (such as ground plane of the earth, stratified printed or integrated circuits, etc.) the use of the mixed-potential integral equation (MPIE) in conjunction with the spatial-domain MoM is the mostly preferred choice [11–14], requiring the knowledge of the Green's functions of the vector and scalar potentials in the spatial domain. However, especially for the structures in multi-layer planar media, the spatial-domain Green's functions are quite complicated to evaluate than those for free space. In order to compute them, Hankel transform, referred to as Sommerfeld integrals in EM community, must be implemented over the analytically expressible spectral-domain Green's functions. However it's well known that the direct numerical evaluation of the Sommerfeld integrals is a time consuming and computationally expensive process due to its oscillatory and slowly decaying nature [15]. To solve this problem, DCIM was developed to evaluate the spatial-domain Green's functions more efficiently and also in closed forms. The method attracted much attention among the researchers and it was improved several times [16–32] and finally became a powerful method with regard to the computational efficiency and the capability of representing all the natural wave constituents of a dipole in any configuration of planar layered media. The main idea of all DCIM algorithms can be summarized in two steps: *i*) approximating the closed-form spectral-domain Green's functions as a sum of complex exponentials and *ii*) using Sommerfeld integral identity to evaluate the Sommerfeld integrals. As a result, the spatial-domain Green's functions are written as a sum of complex images.

However all DCIM approaches developed so far have been suffering from two major issues for a long time, which are the lack of *i)* a proper error metric incorporated in the DCIM algorithm that would ensure the end result in the spatial domain and *ii)* an order selection algorithm that would find the optimal number of complex images automatically. Since the latter issue can not be solved unless the former one is remedied, the error metric issue is solved first. In DCIM, the approximation of the spectral-domain Green's function in terms of complex exponentials is performed without considering the spatial-domain error, i.e. error minimization in the spectral domain is not equivalent to the one in the spatial domain. Hence, the increase in the number of complex exponentials does not guarantee a decrease in the spatial-domain error. Therefore, although many robust and efficient algorithms with good results have been developed, the accuracy of the method has always been questionable as clearly stated in [33]. For this reason, engineers avoid using it in the development of commercial softwares and simulation tools. In this thesis, an algorithm is proposed to solve this long-standing shortcoming of the method. For this purpose, a general weighted norm of the spatial-domain error is defined and transformed to the spectral domain and a metric is proposed to be used in the implementation of DCIM. It is observed that the Weighted Least Squares (WLS) optimization needs to be employed to map the error-criterion from the spatial to the spectral domain. In addition, the leakage problem, which is inherent to multi-level DCIM algorithms due to the semi-independent procedure among the levels, is addressed and eliminated by applying a final WLS optimization. The proposed spatial error criterion together with the leakage elimination is applied to the latest three-level DCIM [32] and the spatial-domain Green's functions of vector and scalar potential for some typical planar media are found by the proposed method. These examples verified that the WLS optimization assures the accuracy of the end result. The details of this study is given in Chapter 2.

Establishing an error metric to DCIM opens the way to find an automatic order selection method since the spatial-domain error is now guaranteed to be smaller in

the weighted least squares sense as the number of terms increases. Typically, no matter which version of the DCIM is employed, the number of exponentials used to express the spectral-domain Green's functions is designated by the number of the dominant eigenvalues of a selection matrix in the subspace method, and these eigenvalues are selected manually or by the computer based on a predefined tolerance, that is, user intervention is needed in either case. However there is no underlying theory or practical evidence that this approach provides an optimum number of terms in any measure. To eliminate this shortcoming of the DCIM, an automatic order selection approach based on the minimum description length (MDL) concept has been adopted to the DCIM approach successfully with the combination of the spatial error criterion. One of the main reasons for the choice of the MDL approach is that it is one of the most practical and robust model selection approaches in the community of information theory. The MDL approach refers to finding the most suitable choice of model from a set of candidates. According to the MDL idea, the most suitable model is the one that leads to the most compression in the representation of the data and provides the shortest description length from the limited observations. This is achieved by finding the optimum balance between the error and complexity of the approximation. Furthermore, the MDL approach does not assume the existence of a true model, but tries to find the most suitable candidate. Before adopting the MDL approach to DCIM, it was investigated carefully and applied some simpler examples such as polynomial and basic exponential fitting problems. After getting successful results on the order selection issue, the error criterion developed for the DCIM is implemented to the MDL approach successfully. As a result the new DCIM approach, referred to as DCIM with model order selection is proposed. The method provides a choice of the model with the least code length, reflecting an optimal balance between the fitting error level in the spatial domain versus model complexity. As an additional utility, this balance can be tuned by the user in favor of accuracy or computational cost. If the user desires to set a predefined SNR level to the problem at hand, she/he can manipulate the parameters of the MDL optimization accordingly. Similarly, this

proposed approach is also implemented on the latest three-level DCIM algorithm and tested on some typical three-layered geometries for verification. The details of this study is given in Chapter 3.

As it was stated before, the ultimate goal is to develop an efficient, accurate and robust algorithm for the analysis of 2D metal and dielectric nano-structures in multilayered media. In the last part of the dissertation, a novel MoM-based approach has been proposed and developed for the analysis of such structures in free space. The efficiency of the method is achieved by obtaining only two analytical expressions depending on the indexes of the basis and testing functions for all entries of the MoM matrix explicitly. Therefore the matrix entries are obtained by evaluating one of the two expressions for the corresponding indices of the matrix. Additionally extending and/or modifying the geometry do not require the calculation of MoM matrix entries from the rough. One needs to evaluate the corresponding expression only for the new indices of the added or modified portion of the geometry. The idea of the study is originated from one of the proposed methods in [34] for which the EM characterization of the planar structures in the multilayered media is obtained by a technique based on the spectral-domain MoM. In [34] the resulting spectral-domain MoM matrix entries are single integrals over an infinite domain which results from the testing procedure. To evaluate the integral, its integrand, except for the exponential term, is approximated in terms of complex exponentials and by getting the inverse Fourier transform with the help of the Sommerfeld integral identity, a closed form expression is obtained analytically. In addition, a single closed-form expression becomes valid for all entries which is the main advantage of the method. The geometry in [34] leads the unknown functions to be the functions of a single variable since the structures are planar and extending infinitely on the plane. Therefore the variation occurs in one dimension only and hence testing procedure requires a single integral. However for 2D structures the testing procedure in the spectral domain results in double integrals over the infinite domain to implement the boundary conditions in two-dimensional space. Therefore we employ the spatial-domain MoM instead of the

spectral-domain MoM but similarly, at final stage, the MoM matrix entries become single integrals over an infinite domain to be evaluated analytically by exponential approximation. The spatial-domain MoM for a 2D structure in free space yields a quinary integral; two for the convolution of the basis and Green's functions and two for the testing procedure. Since these integrals are definite over a finite domain, they can be evaluated analytically. The only integral left without to be evaluated comes from the expression of the spatial-domain Green's function which is written intentionally as the inverse Fourier transform of the known spectral-domain Green's function. As a result, the integral is evaluated in a similar manner discussed in [34]. In Chapter 4, the derivations of MoM approach is given by discussing the different propagation modes in detail and the analyses of some 2D dielectric and metallic systems in optical regime performed by the proposed MoM approach are compared to the results of a reference simulation tool, called *Comsol Multiphysics* by Comsol Inc., for verification. Although this method can be extended to multilayered environment in a straightforward manner by considering each term in the closed-form approximation of the Green's function as the Green's function in free space with complex source location, this part has been left for the future study because of its numerical inefficiency.

As the final study in this thesis, a novel computational method is proposed to evaluate 1-D and 2-D integrals and summations which are relatively difficult to be computed numerically. During the study on MoM, we encountered many relatively difficult and usually infinite integrals with quite complicated functions. In Chapter 4, we proposed a method for 1D integrals for the evaluation of the MoM matrix entries. Since evaluating these integrals via numerical integration was usually time consuming and also sometimes unreliable, we searched for an alternative method to use it for the verification of our proposed method. Finally we developed a method which is versatile to be used for the evaluation of 1D and 2D integrations and summations encountered in many engineering applications. The method is based on applying a subspace algorithm to the samples of partial sums (integrations) and approximating them in terms of complex exponentials. For a convergent summation (integral), the

residue of the exponential term with zero complex pole of this approximation corresponds to the result of the summation (integral). Since the procedure requires the evaluation of relatively less number of terms, the computation time for the evaluation of the summation (integral) is reduced significantly. The method is quite efficient and robust because of the fact that the partial sums (integrals) of an infinite summation (integral) always exhibit an oscillating or monotonic or saturating behavior and if the summation (integral) is convergent, the behavior dies out and leaves a DC term, which is the result of the summation (integral). Therefore, the partial sums (integrals) are approximated in terms of exponentials to find this zero frequency term. The method is applied to various 1-D and 2-D problems with known or unknown analytical results and their performance is verified regarding the computation time. Since this study proposes a general tool (not only related to the main concern of this thesis), it is presented in the Appendix.

Mr. Harrington, the originator of the MoM, once said that the MoM is more a concept than a method and hence almost any solution can be interpreted according to the method of moments [35]. These words proves that the MoM will be always needed and the research on MoM will be a never ending road in CEM.

1.1. Contributions

In this thesis, we have provided remedies for the long-lasting two important problems of the DCIM, by which the proposed new DCIM has become very reliable, robust and accurate, rendering the approach very friendly for CAD tool development.

The first problem was the lack of a spatial-domain error metric assuring the accuracy of the end result. As discussed in the main section, a suitable and convenient method is proposed by introducing a proper WLS into the DCIM algorithm. The corresponding work was presented in [36,37] and can be found in [38].

Second shortcoming of the DCIM was the lack of an automatic order selection routine to decide the number of exponentials to be used in DCIM. With the combina-

tion of the spatial error criterion, an order selection algorithm based on the MDL is introduced. The corresponding work was presented in [37] and can be found in [39].

These two problems were considered as the only remaining hurdles of the DCIM obstructing its usage in the CAD tools and commercial softwares. The improvements, discussed in this thesis, result in a robust, accurate, very reliable and automatic DCIM algorithm which is suitable for the implementation to commercial tools .

The study on MoM for 2D structures was a novel and numerically efficient MoM based method for the characterization of 2D structures in free space. The power of the method arises from obtaining analytical expressions with explicitly written indexes for MoM matrix entries. With these expressions filling the MoM matrix entries and modifying the geometry can be performed efficiently. The corresponding work was presented in [40].

Finally, an additional study presented in Appendix was developed for the evaluation of 1D and 2D summations and integrals. The approach uses a set of partial summations (integrations) to find the result of the summation (integral). The procedure requires the evaluation of relatively less number of terms, therefore the computation time is reduced significantly. The corresponding work was presented in [41].

Chapter 2

Discrete Complex Image Method with Spatial Error Criterion

2.1. Introduction

Green's Functions play an important role in computational electromagnetics, as they help transform governing wave equations to integral equations [10, 42, 43], and in turn, facilitate the use of the well-known Method of Moments (MoM) in the analysis of printed structures in multilayered media [11, 44–47]. Since the implementation of the MoM in the spatial-domain requires the knowledge of the spatial-domain Green's functions, computing the spatial-domain Green's functions from their analytically expressible spectral-domain counterparts requires the implementation of the Hankel transform, generally referred to as Sommerfeld integrals in the literature. It is very well known that direct numerical evaluation of the Sommerfeld integrals is a time-consuming and computationally expensive process due to its oscillatory and slowly decaying nature [15, 48]. However, with the introduction of the DCIM method [49, 50], a new approach has emerged to get the spatial-domain Green's functions more efficiently and also in closed forms. Starting from its first introduction up to the latest development, all proposed approaches based on the DCIM suffer from the fact that

there is no proper error minimization in the spatial-domain. As a result, even though some robust algorithms with very good approximate results have been developed, the accuracy of the method has always been questionable, and no high level confidence is established for the method [33]. In this paper, it is intended to develop an algorithm that would answer this long standing shortcoming of the method.

In order to put things into perspective, a brief chronological overview of the development of DCIM-based methods for the computation of the spatial-domain Green's functions is provided below. Before the introduction of the DCIM, there was mainly one general approach for the evaluation of Sommerfeld-type integrals: numerical integration in conjunction with some transform techniques [15, 16, 48]. Because this approach can provide the value of the integral for a fixed spatial distance ρ one at a time, and because one needs to know the spatial-domain Green's functions for a range of spatial distances in order to use them in conjunction with the MoM, it was not considered to be efficient and suitable for that purpose. Therefore, the proposal for approximating the spatial-domain Green's functions in closed forms in [49] and [50] attracted much interest, and they were followed by a series of related work [17–32, 51]. The original work [49] and its follow-up [50] proposed approximating the spectral-domain Green's functions in terms of complex exponentials, and transforming them into the spatial-domain analytically with the help of the Sommerfeld identity. Although the idea was quite innovative, its implementation was not as robust and efficient as desired, and because of that, the method was restricted for a rather narrow class of geometries, namely for a thick slab backed by a ground plane. This was first followed by an extension that improved its coverage of geometries to multilayered structures [17, 18], and then followed by a rather major extension that has significantly improved the efficiency and robustness of the method (with the introduction of the 2-level algorithm [19]). Although the 2-level DCIM, when coupled with the analytical inclusion of the surface wave contributions, provided very good approximations in closed forms for the spatial-domain Green's functions over a distance well beyond a few wavelengths from the source [25, 26, 52], the far-field behavior in the vicinity of

interfaces for some configurations is not accurate. This was rightly attributed to the lack of the lateral wave contribution in the closed-form representation, as it was shown that these configurations dominantly support lateral waves in the far-field region [31]. Since lateral waves in the spatial-domain are due to the branch-point contributions in the spectral-domain, the sampling path of the 2-level DCIM has recently been modified in such a way that the new path passes very close to the branch point and thus capture the branch-point contribution [32]. Consequently, by this latest version of the DCIM, it was demonstrated that all the natural wave constituents of a dipole in any configuration of planar layered media have been accounted for, and represented very accurately in the closed-form approximations of the spatial-domain Green's functions. Although such a powerful tool has been established to get the closed-form Green's functions quite efficiently, this would not be enough to increase confidence of CAD tool developers unless some sort of error metric is incorporated in the algorithm that would ensure the accuracy of the end result [33].

Since the proposed error metric will be implemented on the latest version of the DCIM, i.e., the 3-level algorithm, it would be instructive to briefly review the key steps of the algorithm in Section 2.2. It is followed, in Section 2.3, by the introduction of errors in the spatial and the spectral-domains, and their connections under the Hankel transformation. Section 2.4 provides some numerical examples to validate the robustness, accuracy and ease of implementation of the algorithm for a typical geometry, and some conclusions are drawn in Section 2.5.

2.2. Overview of DCIM

For the sake of illustration, consider a typical planar multilayered structure as shown in Fig. 2.1, where the electromagnetic properties of the layers vary in z-direction only.

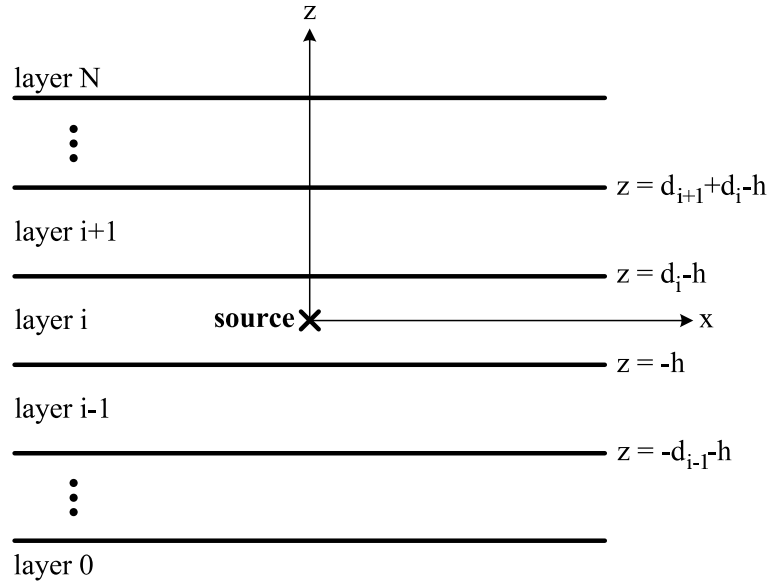


Figure 2.1: A general multi-layer planar medium

It is well-known that Green's functions for planar layered media are obtained recursively as closed-form expressions in the spectral-domain, and can be transformed to the spatial-domain by the following Hankel transform integral, also known as Sommerfeld integral:

$$g(\rho) = \frac{1}{2\pi} \int_S dk_\rho k_\rho J_0(k_\rho \rho) G(k_\rho) \quad (2.1)$$

where g and G are the spatial- and spectral-domain Green's functions, respectively, J_0 is a zeroth order Bessel function of the first kind and S denotes the integration path defined over the first quadrant in k_ρ -plane.

Since it is generally computationally intensive to evaluate Sommerfeld integrals using numerical integration algorithms, the DCIM has been developed to avoid this expensive step by mainly introducing two critical steps: i) approximate the closed-form spectral-domain Green's functions as the linear combinations of complex exponentials; and ii) evaluate the Sommerfeld integrals in closed forms via the Sommerfeld integral identity

$$\frac{e^{-jk_0 r}}{r} = \int_S dk_\rho k_\rho J_0(k_\rho \rho) \frac{e^{-jk_z z}}{jk_z} \quad (2.2)$$

where $r = \sqrt{\rho^2 + z^2}$ and $k_0 = \sqrt{k_\rho^2 + k_z^2}$. As a result, the spatial-domain Green's

functions can be written analytically as a sum of complex images

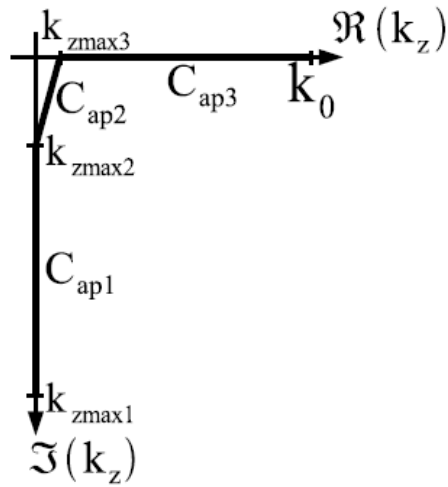
$$\underbrace{\frac{1}{4\pi} \sum_{l=1}^M \alpha^{(l)} \frac{e^{-jk_0 r^{(l)}}}{r^{(l)}}}_{g(\rho)} = \frac{1}{2\pi} \int_S dk_\rho k_\rho J_0(k_\rho \rho) \underbrace{\frac{1}{2jk_z} \sum_{l=1}^M \alpha^{(l)} e^{-\beta^{(l)} k_z}}_{G(k_\rho)} \quad (2.3)$$

where $r^{(l)} = \sqrt{\rho^2 + (-j\beta^{(l)})^2}$ is a complex distance, due to which the method is referred to as discrete complex image method.

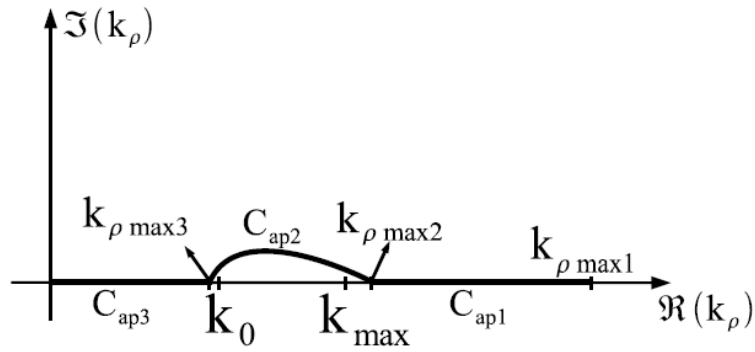
As discussed in Introduction, 2-level DCIM was a significant improvement regarding the reduction in the number of samples required for the exponential approximation and the relatively low noise sensitivity. It is achieved by dividing the integration path and introducing two level sampling algorithm together with a less noise sensitive exponential approximation routine GPOF. In the 3-level DCIM, the sampling path of the 2-level DCIM is modified such a way that the new path passes very close to branch point and so captures its contribution. The modification results in a three level sampling algorithm. Note that there can be many different alternatives for the deformed paths, we use the paths shown in Fig. 2.2 on k_ρ and k_z planes, respectively, for the implementation of the error criterion. The parametrization of the paths between the linear sampling variable t and wave vector component k_z (to be able to use the integral identity given in (3.17)) is as follows:

$$\begin{aligned} C_{ap1} : \quad k_z &= jk_0 \left[\frac{T_{02}}{T_{03} + 1} + 1 \right] & 0 \leq t \leq T_{01} \\ C_{ap2} : \quad k_z &= k_0 \left[\frac{1}{T_{03} + 1} + 1 \right] \left[-jt + \left(1 - \frac{t}{T_{02}} \right) \right] & 0 \leq t \leq T_{02} \\ C_{ap3} : \quad k_z &= k_0 \left[1 - \frac{t}{T_{03} + 1} + 1 \right] & 0 \leq t \leq T_{03} \end{aligned} \quad (2.4)$$

By employing the mappings given in (2.4), the values of k_{zmax1} , k_{zmax2} and k_{zmax3}



(a)



(b)

Figure 2.2: Paths for approximation for 3-level DCIM on the complex (a) k_z plane and (b) k_ρ plane.

shown in Fig. 2.2(a) are given by

$$\begin{aligned} k_{zmax1} &= -jk_0 \left(\frac{T_{02}}{T_{03} + 1} + T_{01} \right) \\ k_{zmax2} &= -jk_0 \left(\frac{T_{02}}{T_{03} + 1} \right) \\ k_{zmax3} &= \frac{k_0}{T_{03} + 1} \end{aligned} \quad (2.5)$$

and by using (2.5) the values of $k_{\rho max1}$, $k_{\rho max2}$ and $k_{\rho max3}$ shown in Fig. 2.2(b) are found to be:

$$\begin{aligned} k_{\rho max1} &= k_0 \sqrt{1 + \left(\frac{T_{02}}{T_{03} + 1} + T_{01} \right)^2} \\ k_{\rho max2} &= k_0 \sqrt{1 + \left(\frac{T_{02}}{T_{03} + 1} \right)^2} \\ k_{\rho max3} &= k_0 \sqrt{1 + \left(\frac{k_0}{T_{03} + 1} \right)^2} \end{aligned} \quad (2.6)$$

After specification of the path, the first step of the method is sampling the spectral domain Green's function $\tilde{G}(k_\rho)$ along the path C_{ap1} and approximating it by a set of complex exponentials using GPOF:

$$f_1(k_\rho) = \left(\tilde{G}(k_\rho) \times 2jk_z; k_\rho \in C_{ap1} \right) \cong \sum_{l=1}^{M_1} a_1^{(l)} e^{b_1^{(l)} k_z} \cong \sum_{l=1}^{M_1} \alpha_1^{(l)} e^{-\beta_1^{(l)} k_z} \quad (2.7)$$

where $a_1^{(l)}$ and $b_1^{(l)}$ are the coefficients and exponents obtained from GPOF method and M_1 is the number of exponentials used in the first level of the approximation. In order to employ Sommerfeld identity, the coefficients and exponents need to be transformed in to the k_z domain by using the corresponding parameterizations of the sampling path as follows:

$$\beta_1^{(l)} = \frac{b_1^{(l)}}{jk_0} \quad \alpha_1^{(l)} = a_1^{(l)} e^{-jk_0 \beta_1^{(l)} \frac{T_{02}}{T_{03}+1}} \quad (2.8)$$

As the set of parameters along the first path is obtained, they are subtracted from the spectral domain Green's function and the remaining function is sampled along the path C_{ap2} and approximated as a sum of exponentials via GPOF in the same manner:

$$f_2(k_\rho) = \left(\tilde{G}(k_\rho) \times 2jk_z - f_1(k_\rho); k_\rho \in C_{ap2} \right) \cong \sum_{l=1}^{M_2} a_2^{(l)} e^{b_2^{(l)} k_z} \cong \sum_{l=1}^{M_2} \alpha_2^{(l)} e^{-\beta_2^{(l)} k_z} \quad (2.9)$$

where $a_2^{(l)}$ and $b_2^{(l)}$ are the coefficients and exponents obtained from GPOF method and M_2 is the number of exponentials used in the second level of the approximation. The transformation of the coefficients in to the k_z domain is achieved by using the parametrization of the second sampling path as follows:

$$\beta_2^{(l)} = \frac{b_2^{(l)} T_{02} (T_{03} + 1)}{k_0 (1 + jT_{02})} \quad \alpha_2^{(l)} = a_2^{(l)} e^{k_0 \beta_2^{(l)} \frac{1}{T_{03} + 1}} \quad (2.10)$$

The similar step is repeated for the sampled data over the path C_{ap3} to find the last coefficients:

$$f_3(k_\rho) = \left(\tilde{G}(k_\rho) \times 2jk_z - f_1(k_\rho) - f_2(k_\rho); k_\rho \in C_{ap3} \right) \cong \sum_{l=1}^{M_3} a_3^{(l)} e^{b_3^{(l)} k_z} \cong \sum_{l=1}^{M_3} \alpha_3^{(l)} e^{-\beta_3^{(l)} k_z} \quad (2.11)$$

where $a_3^{(l)}$ and $b_3^{(l)}$ are the coefficients and exponents obtained from GPOF method and M_3 is the number of exponentials used in the third level of the approximation. The transformation yields

$$\beta_3^{(l)} = \frac{b_3^{(l)} (T_{03} + 1)}{k_0} \quad \alpha_3^{(l)} = a_3^{(l)} e^{k_0 \beta_3^{(l)}} \quad (2.12)$$

Finally, the spatial domain Green's function can be written in closed form by using the coefficients found in each sampling region by using the relation in (2.3) as

$$g(\rho) = \frac{1}{4\pi} \sum_{n=1}^3 \sum_{l=1}^{M_n} \alpha_n^{(l)} \frac{e^{-jk_0 r_n^{(l)}}}{r_n^{(l)}} \quad (2.13)$$

where $r_n^{(l)} = \sqrt{\rho^2 + (-j\beta_n^{(l)})^2}$ is the complex distance. Although the proposed error criterion is developed for all kinds of DCIM algorithms, the details discussed in this section will be quite instructive to understand the additional improvement achieved for the multilevel DCIM algorithms which will be presented in this study.

2.3. Connection Between Spectral- and Spatial-Domain Errors

As stated above, the main contribution of this article is to propose a DCIM-based algorithm that minimizes the spatial-domain error. Remembering that the DCIM-based algorithms perform most of the error-prone processing in the spectral-domain, to achieve this goal, one needs to develop some sort of mapping algorithm that would *transform* or *reflect* the error criterion in the spatial-domain to the one in the spectral-domain, as will be detailed below in this section.

Before getting into the details, it is necessary to set the stage for the development of the method by stating the problem formally as follows: for a given Hankel transform pair with a spatial-domain function $g(\rho)$ and its spectral-domain counterpart $G(k_\rho)$, construct an approximate spatial-domain function $\hat{g}(\rho)$ from the spectral-domain samples ($\{G(k_\rho^{(l)}) : k_\rho^{(l)} \in \mathcal{K}\}$ where \mathcal{K} is a finite, discrete, ordered set with elements $\{k_\rho^{(1)}, k_\rho^{(2)}, \dots, k_\rho^{(N)}\}$) such that the distance between the true spatial-domain function $g(\rho)$ and its estimate $\hat{g}(\rho)$ is minimized. According to the statement of the problem, it is necessary to define a distance between the two functions; as it is well-known in functional analysis, all norms defined over the space of continuous variable functions qualify as valid metric choices, among which the weighted p-norm is chosen as a suitable distance metric in this work, and defined by

$$C_p(e) = \left(\int_0^\infty w(\rho) |e(\rho)|^p d\rho \right)^{1/p}, \quad (2.14)$$

where $w(\rho)$ is the non-negative weighting function, $e(\rho)$ ($= g(\rho) - \hat{g}(\rho)$) is the error function, and $p \geq 1$ is a rational number. The selection of the weighting function $w(\rho)$ and the constant p determines how error values at different locations contribute to the overall error magnitude, that is, to the distance metric. To be more specific, one can choose the weighting function i) to give more weight to a certain region of interest by using an appropriate window function, or ii) to enforce similar signal to error magnitude ratios at all distances. Although the latter criterion requires the

knowledge of the spatial-domain function $g(\rho)$, which is an unknown for the problem at hand, knowing or having some educated guess about its asymptotic behavior for large distances would be sufficient. For example, if $g(\rho) \propto 1/\rho^\alpha$ for large ρ , then a sensible choice for the weighting function would be $w(\rho) = \rho^{2\alpha}$ in order to achieve signal level dependent error weighting. Regarding the choice of the constant p , a typical choice is 2, which is a continuous extension of the Euclidean norm. This choice is mainly motivated by its algorithmic convenience as well as the tractability of the corresponding analysis. In addition, it also plays an important role in terms of bridging the spatial-domain goals to the spectral-domain ones, as will be detailed below.

It is important to note that, unlike Parseval relation in Fourier Transform, minimizing the 2-norm in the Hankel Transform domain is not equivalent to minimizing 2-norm in the spatial-domain (with $w(\rho) = 1$). Therefore, the use of Ordinary Least Squares (OLS) in the spectral-domain, as it is the case in the standard DCIM procedure, is not justified from the error minimization point of view in the spatial-domain. As a result, the cost function for the choice of $p = 2$ is written as

$$C_2(e) = \int_0^\infty w(\rho)|e(\rho)|^2 d\rho, \quad (2.15)$$

where the power term $1/2$ is dropped and $C_2(e)$ is referred to as the weighted error energy. Once the cost function is defined in the spatial-domain, it needs to be mapped onto the spectral-domain involving the error function $E(k_\rho)$, which is defined as the difference between the exact value of the spectral-domain expression and its approximation over the integration path S .

2.3.1. Parseval-like identity for Deformed Paths

In the DCIM approach, the core of the algorithm is to approximate a spectral-domain Green's function with a linear combination of rational functions containing exponentials. The conventional algorithm involves the computation of the exponents, through a subspace approach such as GPOF [53] or ESPRIT [54], and the computation of the

weights of the corresponding exponentials by using OLS. However, the (unweighted) energy minimization in the spectral-domain, as enforced by the OLS step, is not equivalent to energy minimization in the spatial-domain. For this reason, in this section, the spectral-domain equivalent of the spatial-domain error criterion given in (2.15) is to be obtained, so that the spectral-domain approximation could be executed in a spatially meaningful way.

The spectral-domain equivalent of the metric in (2.15) can be obtained by substituting the definition of the Hankel transform (3.16) into (2.15), as

$$\begin{aligned} C_2(e) &= \int_0^\infty w(\rho)e(\rho)e^*(\rho)d\rho \\ &= \frac{1}{4\pi^2} \int_S \int_S E(k_{\rho_1})E(k_{\rho_2})^* K(k_{\rho_1}, k_{\rho_2})k_{\rho_1}k_{\rho_2}^* dk_{\rho_1} dk_{\rho_2}^* \end{aligned} \quad (2.16)$$

where

$$K(k_{\rho_1}, k_{\rho_2}) = \int_0^\infty w(\rho)J_0(k_{\rho_1})J_0^*(k_{\rho_2})d\rho. \quad (2.17)$$

Note that the change of the order of integration in obtaining the final expression in (2.16) can be justified by the uniform convergence arguments supported by the choice of the weighting function $w(\rho)$ [55]. As a special case, when the weighting function is selected as

$$w(\rho) = \begin{cases} \rho & 0 \leq \rho \leq R, \\ 0 & \text{otherwise,} \end{cases} \quad (2.18)$$

the integration kernel K in (2.17) can be simplified to

$$L_R(k_{\rho_1}, k_{\rho_2}) = \int_0^R \rho J_0(k_{\rho_1})J_0(k_{\rho_2}^*)d\rho, \quad (2.19)$$

which is known as the Lommel integral [56], and has a closed-form expression as

$$\begin{aligned} L_R(k_{\rho_1}, k_{\rho_2}) &= \\ &\begin{cases} \frac{1}{k_{\rho_1}^2 - k_{\rho_2}^2} (k_{\rho_2} J_0(k_{\rho_1} R) J_0^*(k_{\rho_2} R) \\ \quad - k_{\rho_1} J_0(k_{\rho_2} R) J_0^*(k_{\rho_1} R)) & k_{\rho_1} \neq k_{\rho_2}, \\ \frac{k_{\rho_1}^2}{2} (J_0^2(k_{\rho_1} R) + J_1^2(k_{\rho_1} R)) & k_{\rho_1} = k_{\rho_2}. \end{cases} \end{aligned} \quad (2.20)$$

In the DCIM approach, the numerical approximation is performed over a discrete set of frequencies, as specified by the set $\mathcal{K}=\{k_\rho^{(1)}, k_\rho^{(2)}, \dots, k_\rho^{(N)}\}$. Therefore, the spectral-domain metric in (2.16) can be approximately evaluated as follows:

$$\begin{aligned} \mathcal{C}_\mathcal{K}(E) &= \frac{1}{4\pi^2} \mathbf{E}^H \mathbf{\Gamma}_\mathcal{K} \mathbf{E} \\ &= \frac{1}{4\pi^2} \sum_{k_{\rho_1}, k_{\rho_2} \in \mathcal{K}} \sum E(k_{\rho_1}) E^*(k_{\rho_2}) K(k_{\rho_1}, k_{\rho_2}) k_{\rho_1} k_{\rho_2}^* \Delta_{k_{\rho_1}} \Delta_{k_{\rho_2}}^* \end{aligned} \quad (2.21)$$

where \mathbf{E} is a vector containing the spectral-domain error values as

$$\mathbf{E} = \begin{bmatrix} E(k_\rho^{(1)}) & E(k_\rho^{(2)}) & \dots & E(k_\rho^{(N)}) \end{bmatrix}^T, \quad (2.22)$$

$\mathbf{\Gamma}_\mathcal{K}$ is an $N \times N$ matrix, whose element at row m and column n is given by

$$\Gamma_{mn} = k_\rho^{(n)} k_\rho^{(m)*} \Delta_{k_\rho^{(n)}} \Delta_{k_\rho^{(m)}}^* K(k_\rho^{(n)}, k_\rho^{(m)}), \quad (2.23)$$

and $\Delta_{k_\rho^{(n)}}$ is the (backward or forward) difference of the spectral grid sequence evaluated at $k_\rho^{(n)}$.

Remembering that, for a positive definite matrix \mathbf{W} , the weighted 2-norm is defined in general as

$$\|\mathbf{x}\|_\mathbf{W} \triangleq \sqrt{\mathbf{x}^H \mathbf{W} \mathbf{x}}, \quad (2.24)$$

the spectral-domain reflection of the weighted error metric in the spatial-domain becomes equivalent to a squared weighted 2-norm,

$$\mathcal{C}_\mathcal{K}(E) = \frac{1}{4\pi^2} \|\mathbf{E}\|_{\mathbf{\Gamma}_\mathcal{K}}^2, \quad (2.25)$$

as $\mathbf{\Gamma}_\mathcal{K}$ is a Hermitian (positive definite) weighting matrix. Since it is only a function of the spectral-domain grid points, which are known a priori depending upon the choice of the paths in the DCIM implementation, it can be pre-calculated for once and employed in all other computations. Consequently, in order to incorporate the spatial-domain error criterion into the DCIM algorithm, the Weighted Least Squares (WLS) approach with the weighting matrix $\mathbf{\Gamma}_\mathcal{K}$ needs to replace the OLS used in the conventional approach. This would cause the spectral shaping of the errors in favor of the desired spatial performance.

For multi-level DCIM algorithms, the integration path in the spectral-domain is divided into multiple connected regions, on each of which the DCIM algorithm is applied separately. Since the weighting matrix is formed from the spectral grid as described in (2.23), its diagonal sub-matrices correspond to the sub-regions of the spectral grid, and therefore, they should be used as the weighting matrices for the corresponding regions. For example, for the three-level DCIM [57], the set \mathcal{K} can be written as the union of three disjoint (ordered) sets, in the form of

$$\mathcal{K} = \mathcal{K}_1 \cup \mathcal{K}_2 \cup \mathcal{K}_3, \quad (2.26)$$

where \mathcal{K}_i denotes the set of spectral points for Region- i , with cardinality n_i . In this case, the weighting matrix $\mathbf{\Gamma}_{\mathcal{K}}$ can be partitioned as

$$\mathbf{\Gamma}_{\mathcal{K}} = \begin{bmatrix} \mathbf{\Gamma}_{\mathcal{K}_1} & \mathbf{\Gamma}_{\mathcal{K}_1, \mathcal{K}_2} & \mathbf{\Gamma}_{\mathcal{K}_1, \mathcal{K}_3} \\ \mathbf{\Gamma}_{\mathcal{K}_1, \mathcal{K}_2}^H & \mathbf{\Gamma}_{\mathcal{K}_2} & \mathbf{\Gamma}_{\mathcal{K}_2, \mathcal{K}_3} \\ \mathbf{\Gamma}_{\mathcal{K}_1, \mathcal{K}_3}^H & \mathbf{\Gamma}_{\mathcal{K}_2, \mathcal{K}_3}^H & \mathbf{\Gamma}_{\mathcal{K}_3} \end{bmatrix} \quad (2.27)$$

and, for Region- i , the sub-matrix $\mathbf{\Gamma}_{\mathcal{K}_i}$ is to be used as the weighting matrix in the implementation of WLS.

2.3.2. Practical Application

Once the mapping of the error criterion from the spatial-domain to the spectral-domain has been established by introducing a proper WLS, for its practical application, the only thing left is the judicious choice of weighting function $w(\rho)$ in (2.15). As it is demonstrated in the previous section, the choice of linear weighting over a window (2.18) seems to be quite convenient, referred to as Metric-1 throughout this work, as it results in a weighting matrix that can be written in terms of the kernel function L_R in the form of

$$\Gamma_{mn} = k_{\rho}^{(n)} k_{\rho}^{(m)*} \Delta_{k_{\rho}^{(n)}} \Delta_{k_{\rho}^{(m)}}^* L_R(k_{\rho}^{(n)}, k_{\rho}^{(m)}), \quad (2.28)$$

where L_R has a closed form expression (2.20). However, such a convenience would not be enough if the choice of the weighting function were not suitable for the type

of functions to be approximated, namely Green's functions in layered media. That is, the choice of the weighting function needs to take into consideration of the asymptotic behavior of the function to be approximated, otherwise, undue weight may be given to rather less significant parts of the function, possibly leading to erroneous estimate of the function. Since surface waves are the slowest decaying wave components of Green's functions in planar layered media, with the rate of $\rho^{-1/2}$, the relative biasing of the error for large distances requires a linear weighting function for the weighted error energy (2.15). Therefore, in addition to its algebraic convenience, the asymptotic nature of the functions to be approximated also justifies the use of such weighting function.

However, in the numerical implementation of (2.20), especially for relatively large values of the radius R , the arguments of Bessel functions may grow to an extent that the values of Bessel functions may not be reliable, and, as a result, the resulting error may cause critical inaccuracies in (2.20) due to the ill-conditioned subtraction process. In order to circumvent this numerical problem, a simple approximation for the weighting $\mathbf{\Gamma}_{\mathcal{K}}$ can be proposed (referred to as Metric-2) as follows: if row- i (or column- i) of $\mathbf{\Gamma}_{\mathcal{K}}$ requires the evaluation of a Bessel function with argument greater than a chosen threshold τ_{th} , then all the elements in row- and column- i are set to 0 except

$$\Gamma_{ii} = \mathcal{R}e\{k_{\rho}^{(i)}\}\mathcal{R}e\{\Delta_{k_{\rho}^{(i)}}\}. \quad (2.29)$$

This approximation on the entries of the weighting matrix $\mathbf{\Gamma}$ is justified by the following identity [58]:

$$\int_0^{\infty} \rho J_0(\alpha\rho) J_0(\beta\rho) d\rho = \frac{1}{\alpha} \delta(\alpha - \beta). \quad (2.30)$$

As an alternative approach, one can use the Parseval identity for the Hankel Transform (Metric-3):

$$\int_0^{\infty} \rho |e(\rho)|^2 d\rho = \frac{1}{4\pi^2} \int_0^{\infty} k |E(k)|^2 dk. \quad (2.31)$$

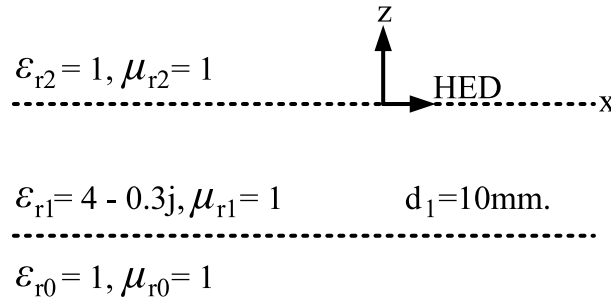


Figure 2.3: A lossy material in air. The locations of the observation and the horizontal electric dipole (HED) are at the interface between the air and the upper boundary of the dielectric layer.

which is valid for cases where the integration path aligns with the real axis in the spectral-domain. For the cases where the integration path S doesn't align with the real axis, it could be approximated as

$$\int_0^\infty \rho |e(\rho)|^2 d\rho \approx \frac{1}{4\pi^2} \int_S |E(k_\rho)|^2 \mathcal{R}e\{k_\rho\} \mathcal{R}e\{dk_\rho\}, \quad (2.32)$$

which can be justified by the closeness of the integration path to the real axis. The spectral-domain weighting matrix corresponding to this case can be written as

$$\begin{aligned} \mathbf{\Gamma}_{\mathcal{K}} = & \text{diag}([\mathcal{R}e\{k_\rho^{(1)}\} \mathcal{R}e\{\Delta_{k_\rho^{(1)}}\} \quad \mathcal{R}e\{k_\rho^{(2)}\} \mathcal{R}e\{\Delta_{k_\rho^{(2)}}\} \\ & \dots \quad \mathcal{R}e\{k_\rho^{(N)}\} \mathcal{R}e\{\Delta_{k_\rho^{(N)}}\}]). \end{aligned} \quad (2.33)$$

Note that although there is no spatial selectivity, when compared to the weighting matrices of Metric-1 and Metric-2 as given in (2.28) and (2.29), respectively, it is a convenient choice because of its computational efficiency.

In order to assess the performance of the proposed three different implementations of the spectral-domain weighted energy, namely Metric-1, Metric-2 and Metric-3, Green's functions in the spectral and spatial-domains are obtained for a lossy slab with $\epsilon_r = 4 - j0.3$ in air at $4GHz$, Fig. 2.3. The spatial-domain Green's functions are obtained from their spectral-domain counterparts by using the 3-level DCIM, where the integration path S is divided into three sub-regions such that they all pass very close to the real axis, as shown in Fig. 2.4. Based on this geometry and the choice of

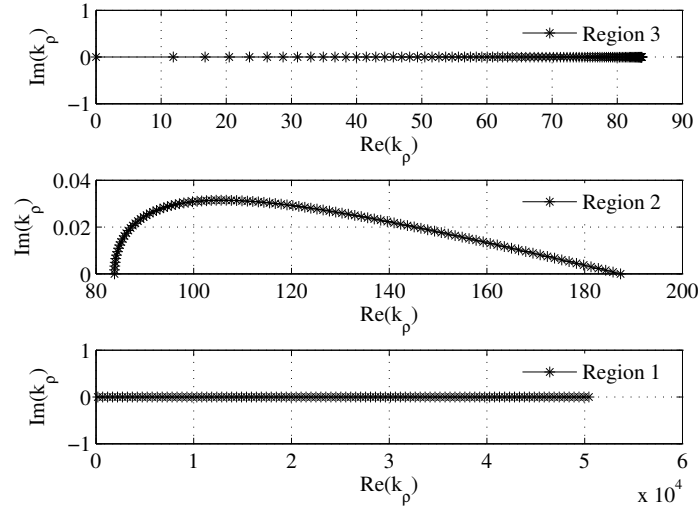


Figure 2.4: Integration path for the 3-level DCIM on complex k_ρ -plane.

the path, Fig. 2.5 shows the estimates of the spatial-domain weighted energy obtained by the three different spectral-domain implementations (2.28), (2.29) and (2.33), and compares them with the true value obtained from the spatial-domain implementation of the metric (2.15) with the weighting function (2.18) via numerical integration. While Metric-1 employs a Parseval-like identity, Metric-2 modifies this approach by introducing a threshold for distance and Metric-3 uses the Parseval identity as if the integration path aligns with the real axis in the spectral-domain. It is observed from Fig. 2.5 that the spatial-domain estimate of the weighted energy by Metric-1 is not reliable for large values of R as expected. On the other hand, Metric-2 and Metric-3 seem to have fixed the problem and the weighted energy obtained via these metrics converge to the true value for large R values. As a result of this assessment, in addition to comparing computational efficiency of the metrics, Metric-3 is chosen and employed throughout this work to minimize the spatial-domain weighted error energy of Green's functions approximated by the DCIM.

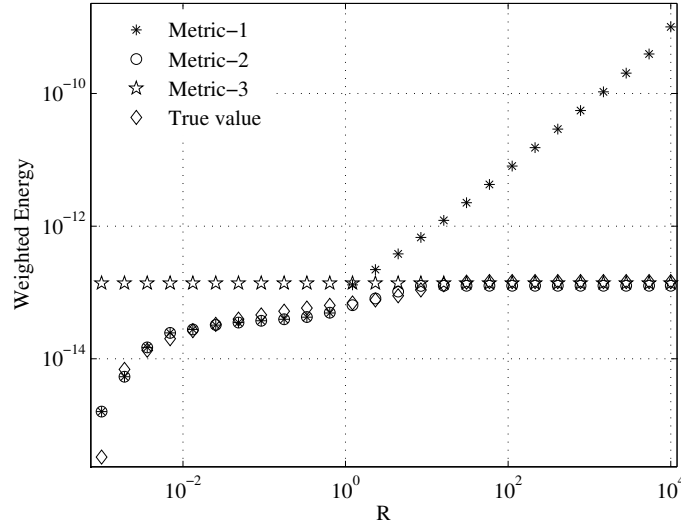


Figure 2.5: Spatial-domain weighted energy and its estimates via three different metrics.

2.3.3. DCIM with Spatial Error Criterion

Based on the discussion in the previous section about bridging the spatial- and spectral-domain metrics, the details of the DCIM with the spatial-domain error criterion, as applied to Green's functions, are provided in this section.

The DCIM for Green's functions is based on the approximation of the spectral-domain Greens functions in terms of a special class of functions as

$$G_a(k_\rho) = \sum_{l=1}^M \alpha^{(l)} \frac{e^{-\beta^{(l)} k_z}}{jk_z} \quad (2.34)$$

where M is the number of fractional terms containing exponentials used in the approximation, $\beta^{(l)}$'s are the constants of the exponents, and $\alpha^{(l)}$'s are the weights of the fractional terms. The goal is to choose the parameters β and α to minimize

$$\|\mathbf{G} - \mathbf{G}_a\|_{\Gamma_K}^2 \quad (2.35)$$

where \mathbf{G} is the vector containing the samples of the spectral-domain Green's function and \mathbf{G}_a is the vector containing the samples of the corresponding approximation

function. This optimization setting is a nonlinear-least-squares problem, and as such it is computationally quite expensive. Therefore, in the implementation of the DCIM, the constant parameters β and α are obtained in separate steps: first, a subspace based approach, such as GPOF or ESPRIT methods, is applied to $H(k_\rho) = jk_z G(k_\rho)$ to obtain the constant parameters of the exponents β , and then, an optimization procedure is employed to get the weight parameters α . Since the first step involves a non-linear approximation, the error criterion is introduced into the second step, that is, into the calculation of the weight parameters. Therefore, to elucidate the difference between the traditional use of the DCIM and the proposed one, the main steps of the computation of the weight parameters in both approaches are provided below.

In the traditional DCIM, the weight parameters α are computed as the solution of the ordinary least squares problem:

$$\text{minimize } \|\mathbf{H} - \mathbf{H}_a\|_2, \quad (2.36)$$

where

$$\mathbf{H} = \left[H(k_\rho^{(1)}) \ H(k_\rho^{(2)}) \ \dots \ H(k_\rho^{(N)}) \right]^T, \quad (2.37)$$

$$H(k_\rho^{(n)}) = 2jk_z^{(n)} G(k_\rho^{(n)}), \quad n = 1, \dots, N \quad (2.38)$$

and

$$\mathbf{H}_a = \left[H_a(k_\rho^{(1)}) \ H_a(k_\rho^{(2)}) \ \dots \ H_a(k_\rho^{(N)}) \right]^T, \quad (2.39)$$

$$\begin{aligned} H_a(k_\rho^{(n)}) &= 2jk_z^{(n)} G_a(k_\rho^{(n)}) \\ &= \sum_{l=1}^M \alpha^{(l)} e^{-\beta^{(l)} k_z^{(n)}}, \quad n = 1, \dots, N. \end{aligned} \quad (2.40)$$

Therefore, $\alpha^{(l)}$'s are obtained by matching the jk_z -scaled version of the spectrum via the solution of the OLS problem as

$$\alpha_{OLS} = \mathbf{A}^\dagger \mathbf{H}, \quad (2.41)$$

where \mathbf{A}^\dagger is the Moore-Penrose pseudo-inverse of \mathbf{A} , and

$$\mathbf{A} = \begin{bmatrix} e^{-\beta^{(1)}k_z^{(1)}} & e^{-\beta^{(2)}k_z^{(1)}} & \dots & e^{-\beta^{(M)}k_z^{(1)}} \\ e^{-\beta^{(1)}k_z^{(2)}} & e^{-\beta^{(2)}k_z^{(2)}} & \dots & e^{-\beta^{(M)}k_z^{(2)}} \\ \vdots & \vdots & \dots & \vdots \\ e^{-\beta^{(1)}k_z^{(N)}} & e^{-\beta^{(2)}k_z^{(N)}} & \dots & e^{-\beta^{(M)}k_z^{(N)}} \end{bmatrix}. \quad (2.42)$$

However, for the proposed DCIM algorithm, the weight parameters $\alpha^{(l)}$'s are obtained from the solution of the weighted least squares problem, whose formal statement is given as

$$\text{minimize} \quad \|\mathbf{G} - \mathbf{G}_a\|_{\Gamma_{\mathcal{K}}}^2, \quad (2.43)$$

and its solution can be compactly written as

$$\alpha_{WLS} = (\mathbf{\Gamma}_{\mathcal{K}}^{1/2}\mathbf{B})^\dagger(\mathbf{\Gamma}_{\mathcal{K}}^{1/2}\mathbf{G}), \quad (2.44)$$

where

$$\mathbf{B} = \begin{bmatrix} \frac{e^{-\beta^{(1)}k_z^{(1)}}}{2jk_z^{(1)}} & \frac{e^{-\beta^{(2)}k_z^{(1)}}}{2jk_z^{(1)}} & \dots & \frac{e^{-\beta^{(M)}k_z^{(1)}}}{2jk_z^{(1)}} \\ \frac{e^{-\beta^{(1)}k_z^{(2)}}}{2jk_z^{(2)}} & \frac{e^{-\beta^{(2)}k_z^{(2)}}}{2jk_z^{(2)}} & \dots & \frac{e^{-\beta^{(M)}k_z^{(2)}}}{2jk_z^{(2)}} \\ \vdots & \vdots & \dots & \vdots \\ \frac{e^{-\beta^{(1)}k_z^{(N)}}}{2jk_z^{(N)}} & \frac{e^{-\beta^{(2)}k_z^{(N)}}}{2jk_z^{(N)}} & \dots & \frac{e^{-\beta^{(M)}k_z^{(N)}}}{2jk_z^{(N)}} \end{bmatrix}, \quad (2.45)$$

and $\mathbf{\Gamma}_{\mathcal{K}}^{1/2}$ is a matrix square-root of $\mathbf{\Gamma}_{\mathcal{K}}$, satisfying $\mathbf{\Gamma}_{\mathcal{K}}^{1/2H}\mathbf{\Gamma}_{\mathcal{K}}^{1/2} = \mathbf{\Gamma}_{\mathcal{K}}$.

In summary, the proposed DCIM approach with the spatial-domain error criterion has two major differences from the conventional DCIM approach in obtaining the weight parameters $\alpha^{(l)}$'s: i) the use of the weighted least-squares instead of the ordinary least squares, and ii) fitting directly the spectral-domain function $G(k_\rho)$, rather than its scaled version $H(k_\rho)$.

2.3.4. Improvement for the Multilevel DCIM

In addition to incorporating the spatial-domain error criterion into the DCIM, there is another source of improvement for the multilevel DCIM approach. In a typical multilevel applications, the domain over which the spectral-domain function is sampled

is divided into sub-regions, which are processed in order, starting from the highest end of the spectrum to the lowest end. The DCIM procedure outlined in the previous section is applied to each region, but their implementations are not independent: once the fitting parameters for Region- l are obtained, the corresponding exponentials are subtracted from the original function used for Region- l , in order to get the function to be approximated over the subsequent regions as discussed in Section 2.2. Therefore, the multilevel DCIM algorithm based on this exponential peeling has the basic advantage that the number of spectral-domain samples required for the whole process and their processing costs by the DCIM are greatly reduced. However, this causally semi-independent processing of the subregions has the basic problem of leakage from regions with larger indices to regions with smaller indices.

In order to alleviate this leakage problem, the whole DCIM algorithm is implemented as usual, except the final (weighted) least squares optimization that provides the weight parameters for the last region. At this stage, all the weight parameters computed in the previous steps are completely ignored, and a fresh (weighted) least squares optimization is applied, over all or a part of the spectral samples that were already used, to obtain the weight parameters for all the exponentials found by the multilevel procedure. This approach makes use of the fact that while the subspace-based frequency estimation step (GPOF or ESPRIT) requires uniformly spaced samples, there is no such requirement for the least-squares applications.

2.4. Numerical Examples and Discussions

2.4.1. Link between spectral- and spatial-domains

Recall that the motivation of this study is to achieve spatial-domain error minimization from the spectral-domain processing. Since minimizing 2-norm in the Hankel Transform domain is not equivalent to minimizing 2-norm in the spatial-domain, the use of OLS in the spectral-domain, which is the case in the standard DCIM applications, may not achieve the spatial-domain error minimization. To illustrate this

fact, the standard and proposed 3-level DCIM algorithms were employed to find the vector-potential Green's function, for the geometry and the path of integration given in Fig. 2.3 and Fig. 2.4, respectively. Since one needs to settle on the number of exponentials M_i to express the signal in each region, where i represents the region for the multilevel DCIM, for the example, the following two cases were used to obtain the spectral- and spatial-domain errors in the fitting by the standard and proposed 3-level DCIM: *case-1*: $M_1 = 3, M_2 = 5, M_3 = 5$ and *case-2*: $M_1 = 3, M_2 = 5, M_3 = 7$, as given in Table 1 and Table 2, respectively. In comparing the two cases, the aim is to demonstrate whether the improvement or deterioration in the spatial-domain error is mapped onto the spectral-domain error consistently. Note that while the true function in the spectral-domain corresponds to the closed-form expression, the true function in the spatial-domain is obtained by the numerical integration of (3.16).

Table 2.1: Error and energy (E) of the spatial- and spectral-domain Green's functions estimated by the standard and proposed 3-level DCIM for *Case-1*.

<i>Case-1</i> (3-5-5)	Proposed DCIM		Standard DCIM	
	Spectral	Spatial	Spectral	Spatial
Error	1.63E-15	8.54E-15	1.23E-15	1.03E-10
E-True Signal	1.38E-13	1.46E-13	2.52E-14	0.00117558
E-Fitting Signal	1.36E-13	1.48E-13	2.23E-14	0.00117544

Table 2.2: Error and energy (E) of the spatial- and spectral-domain Green's functions estimated by the standard and proposed 3-level DCIM for *Case-2*.

<i>Case-2</i> (3-5-7)	Proposed DCIM		Standard DCIM	
	Spectral	Spatial	Spectral	Spatial
Error	1.65E-15	1.55E-14	1.12E-15	1.66E-10
E-True Signal	1.38E-13	1.46E-13	2.52E-14	0.00117558
E-Fitting Signal	1.36E-13	1.48E-13	2.22E-14	0.00117526

Examining the results of the standard DCIM in Table I and Table II, it is observed that while the OLS fitting error of *Case-1* is greater than the error of *Case-2* in the spectral-domain, the error of *Case-1* is smaller than the error of *Case-2* in the spatial-domain. It shows that under the same number of samples, when the number of complex images is changed, the increase (decrease) in the spectral-domain error does not necessarily imply an increase (decrease) in the spatial-domain error for the OLS fitting. This is due to the fact that, the spectral-domain fitting in the standard DCIM is performed without a correct link to the spatial-domain. Since only spectral-domain information is available in reality, the user unwittingly chooses *Case-2* as a better fitting. However, for the proposed DCIM, the consistency between the errors in the spectral and spatial-domain is achieved by the weighted energy minimization in the spectral-domain, which is equivalent to the weighted energy minimization in the spatial-domain, as can be observed from Table I and Table II: The WLS fitting error of *Case-1* is smaller than the error of *Case-2* both in the spectral-domain and in the spatial-domain. In addition to the error values, the values of the signal energies obtained by the standard DCIM are quite different for the spatial- and spectral-domains, which contradicts the Parseval-like relation of the signals, whereas the energies of the signals in the two domains are very close in the case of the proposed DCIM, as they should.

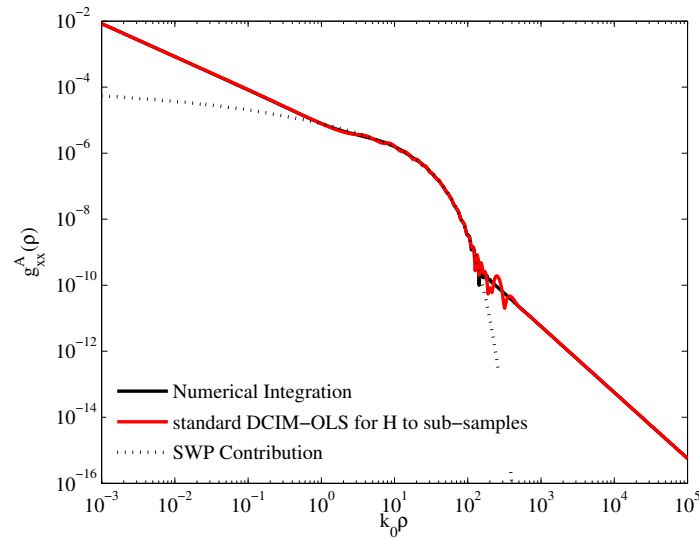
2.4.2. Verification of the proposed method

In this section, some numerical examples are provided to assess and to validate the proposed DCIM for its ability to control errors in the spatial-domain as well as in the spectral-domain. For the sake of coherence in the discussions, the same example used in the previous sections is employed, Fig. 2.3, and for the sake of brevity in the presentation, only the vector potential Green's function in the spatial-domain, as obtained from the standard and the proposed DCIM, are presented and compared with those obtained by the numerical integration of its spectral-domain counterpart, Fig. 2.6. A few notes on the chosen geometry and Green's function for the example are in order: i) the proposed method has been successfully applied to many geometries for all components of Green's dyadic of the vector potential and the Green's functions of the scalar potentials; ii) the geometry has a surface wave pole (SWP), but since the slab is lossy, its contribution decays exponentially in the far-field region, resulting in a dominating lateral wave component in that region; and iii) although SWPs are generally extracted a priori in the application of the multilevel DCIM as suggested in [32], they are not extracted in this example just to see their influence on the approximation. Before introducing the results and accompanying discussions, it would be instructive first to recall the major differences between the proposed DCIM approach with the spatial-domain error criterion and the standard DCIM approach:

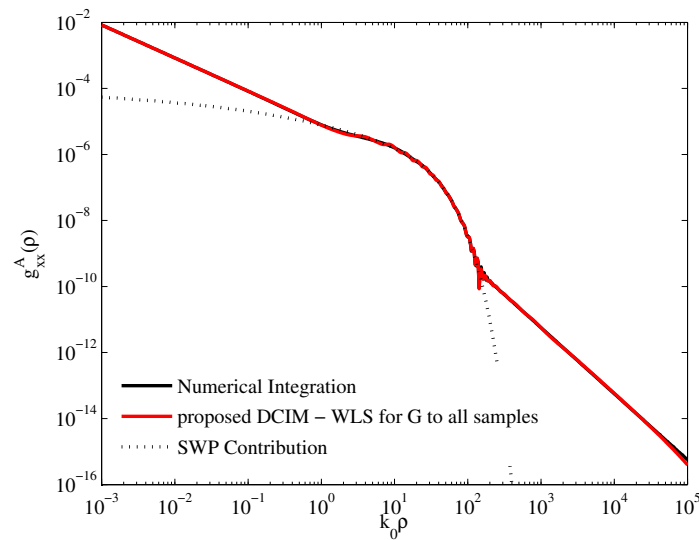
- Use of the weighted least-squares, instead of using the ordinary least-squares (WLS vs. OLS)
- Direct fitting of the spectral-domain function $G(k_\rho)$, instead of its scaled version $H(k_\rho)$ (G vs. H).
- Applying the final weighted least-squares optimization to all spectral samples to obtain all the weight parameters, instead of obtaining the weight parameters of each region separately (all samples vs. sub-samples).

As the first example, the spatial-domain Green's function for the vector potential is presented, is obtained from the standard DCIM and the proposed DCIM with all other improvements, Fig. 2.6(a) and Fig. 2.6(b), respectively. Note that all the results obtained throughout this work are compared to the one obtained by the numerical integration of the spectral-domain Green's functions (3.16). After a brief study on the magnitudes of the spatial-domain Green's function in Figs. 2.6, It's quite clear that both approaches perform quite satisfactorily as far as the accuracy of the results are concerned. However, the slight oscillations around the region where the lateral wave begins to dominate are completely eliminated by the proposed DCIM, predicting the true nature of the Green's function better than the standard DCIM.

To assess the sole contribution of the weighted least squares optimization, and the influence of the additional improvements, to the final result, these improvements are also employed with the standard DCIM. To equalize the effects of the second and third proposed differences stated above, the conventional application of the standard DCIM is modified to the use of the OLS optimization with the spectral-domain function $G(k_\rho)$ over all samples, instead of its scaled version $H(k_\rho)$ over the sub-samples corresponding to the individual regions of the multilevel algorithm. It is observed from Fig. 2.7 that although the results obtained by the modified version of the standard DCIM have been improved in the middle, where the lateral wave begins to dominate, as compared with the results presented in Fig. 2.6(a), they deteriorate at the far end as compared to those obtained by the proposed DCIM Fig. 2.6(b). As a result, improvements on the leakage and on the implementation of the method to the actual function rather than its scaled version have resulted in some improvements in the intermediate region, which seems to be at the expense of the results in the very far region. To distinguish the effects of the leakage in this work, the region-specific weight parameters are used to calculate the spatial-domain Green's function during the implementation of the proposed DCIM, i.e. the leakage alleviation is not performed. It is observed from Fig. 2.8 that the resulting spatial-domain Green's function exhibits some oscillatory behavior in the middle, and can safely be attributed to the leakages



(a)



(b)

Figure 2.6: The magnitude of the spatial-domain Green's function for the vector potential obtained by a) the standard DCIM and b) the proposed DCIM. The numerical integration result is presented for verification. Parameters of the geometry are given in Fig. 2.3 and the frequency of operation is 4 GHz.

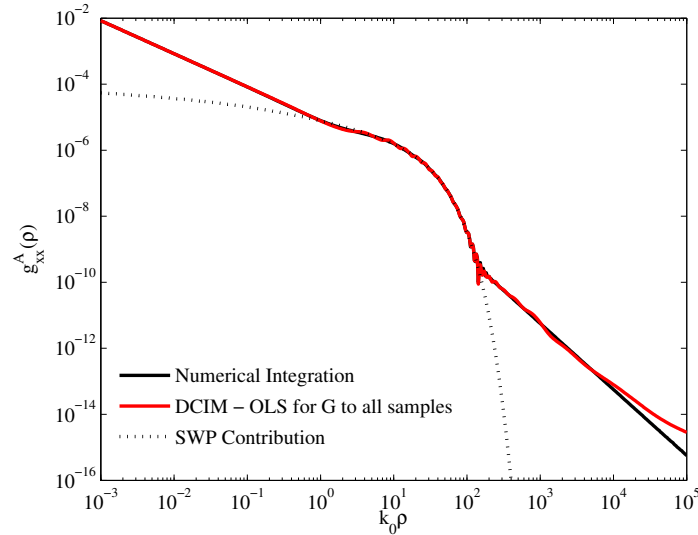


Figure 2.7: The magnitude of the spatial-domain Green's function for the vector potential. Parameters of the geometry are given in Fig. 2.3 and the frequency of operation is 4 GHz.

between the subregions.

2.4.3. More about the leakage

As discussed in the previous section, the proposed DCIM brings in significant improvements to the multilevel fitting not only by introducing WLS to incorporate the spatial-domain error criterion but also by eliminating the possible leakages. In this section, the leakage problem in a standard multilevel DCIM is discussed over the same example that was examined in the previous sections.

As discussed in Section 2.2, in the 3-level DCIM, the spectral-domain sample points are split into three sets in C_{ap1} , C_{ap2} and C_{ap3} as in Fig 2.2, and the approximation is performed over these sets to obtain the corresponding approximating functions, i.e., exponentials, with their exponents and coefficients. During the process, once the fitting parameters for Region-1 are obtained, the corresponding exponentials (composing $f_1(k_\rho)$) are subtracted from the original function in C_{ap2} , and the resulting function $f_2(k_\rho)$ is used for the approximation in Region-2. Following that, $f_1(k_\rho)$

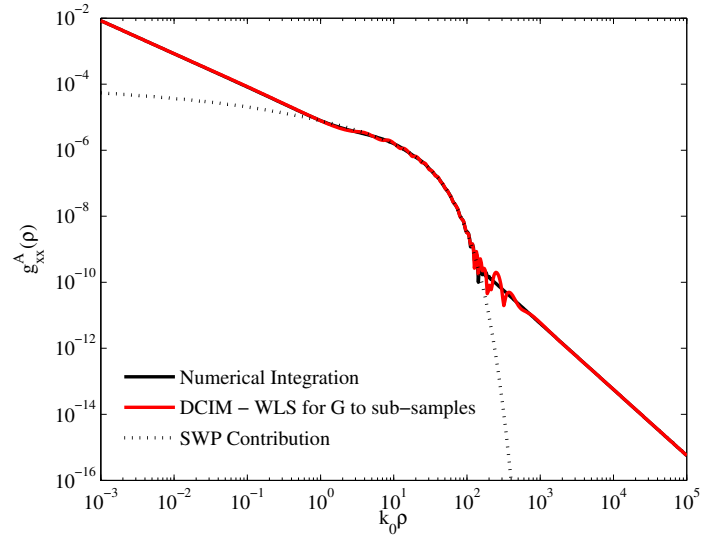


Figure 2.8: The magnitude of the spatial-domain Green's function for the vector potential. Parameters of the geometry are given in Fig. 2.3 and the frequency of operation is 4 GHz.

and $f_2(k_\rho)$ are subtracted from the original function over C_{ap3} to form $f_3(k_\rho)$. Finally, fitting in Region-3 is performed on $f_3(k_\rho)$. Wherever this idea of exponential peeling is applied, it simply assumes that the function calculated by the parameters found from the fitting in Region-2 is 0 in Region-1, i.e.,

$$f_2(k_\rho) = 0 \quad , k_\rho \in C_{ap1} \quad (2.46)$$

and similarly, the function calculated by the parameters found from the fitting in Region-3 is 0 in Region-2 and Region-1:

$$f_3(k_\rho) = 0 \quad , k_\rho \in C_{ap1} \cup C_{ap2}. \quad (2.47)$$

However, since there is no enforcement in the algorithm to guarantee these assumptions, the leakage from regions of low frequencies to the regions of high frequencies may occur, as shown in Fig. 2.9, where different error calculations are presented in the spectral-domain. As Fig. 2.9 seems to be quite complicated, to make it comprehensible, the curves in the figure are explained as follows:

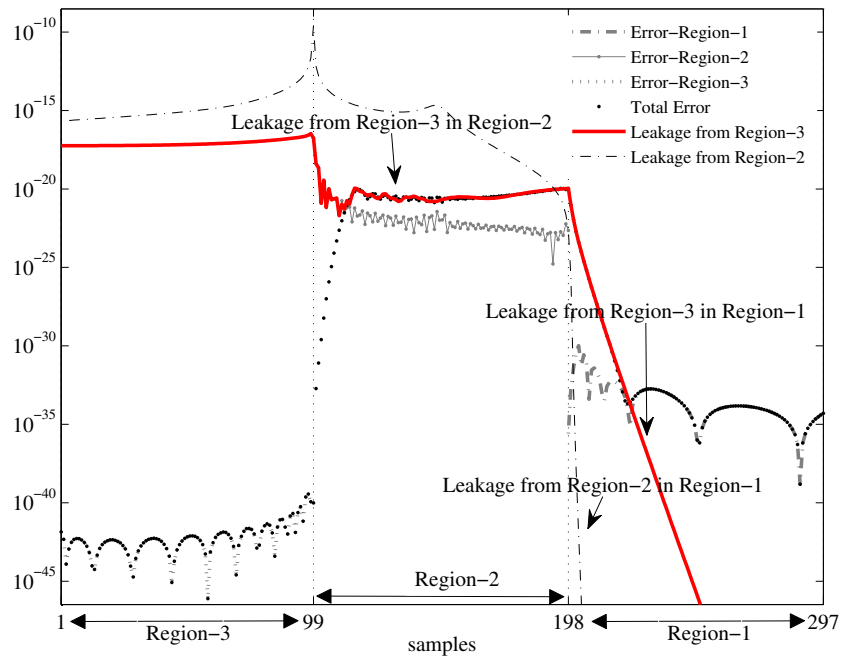


Figure 2.9: Demonstration of the Leakage: Leakage from Region-2 to Region-1, Leakage from Region-3 to Region-2 and to Region-1, the region specific errors and the overall error for the standard DCIM. Parameters of the geometry are given in Fig. 2.3 and the frequency of operation is 4 GHz.

- The curves designated as Error-Region- i ($i = 1, 2, 3$) demonstrate region-specific errors defined as the square of the magnitude of the difference between the actual function and its approximation over the samples of the region;
- the curve designated as Total Error is calculated as the square of the magnitude of the difference between the overall Green's function and its fitting;
- the curve designated as Leakage from Region-2 is the sum of the complex exponentials whose parameters are obtained from the fitting in Region-2, i.e., $f_2(k_\rho)$ and similarly
- the curve designated as Leakage from Region-3 is the sum of the complex exponentials whose parameters are obtained from the fitting in Region-3, i.e., $f_3(k_\rho)$

As it is observed, the leakages exist and leakage from Region-3 is highly dominant, especially in Region-2. In fact, it is so dominant that the overall error follows the leakage even if the actual fitting error in Region-2 is smaller. This matter continues in Region-1 as well, till the leakage from Region-3 becomes smaller than Error-region-1. That's why, taking the region specific error values as the error criterion may lead incorrect conclusions about that fitting.

2.5. Conclusion

After the 3-level DCIM that can take different wave natures into account has recently been introduced, the spatial-domain Green's functions are successfully approximated in closed forms for all ranges and materials [32]. However, even with this development, the DCIM approach may not be considered suitable for the development of commercial EM-based simulation tools for planar layered structures. The main reason for this is the lack of an error metric that could be incorporated into the algorithm

to ensure the accuracy of the end result within the prescribed limits. It is demonstrated that the metric introduced in this work can be easily implemented to any DCIM approach, very likely to boost the confidence of the method. A suitable and convenient metric is proposed by mapping the error criterion from the spatial-domain to the spectral-domain via introducing a proper weighted least squares (with a linear weighting function over a window) into the standard DCIM algorithm. In addition, the leakage problem that is inherent to the standard DCIM implementation has also been addressed and remedied. Modifying the standard DCIM, by implementing the minor improvements (elimination of leakage and direct fitting of the spectral-domain function) together with the major contribution of this work, i.e., incorporating the spatial-domain error criterion, has resulted in a robust, accurate and very reliable DCIM algorithm. The method was successfully applied to many different geometries and different components of the Green's functions.

Chapter 3

Discrete Complex Image Method with Automatic Order Selection

3.1. Introduction

With the advent of high speed computers, electromagnetic simulations of high-frequency systems and complex structures have been quite accessible by researchers and engineers, which undeniably furthers the boundaries of science and technology. In this regard, accurate and efficient computation of Green's functions plays an important role in computational electromagnetics and optics, as Green's functions are the key constituents of integral equations that govern the rules of electromagnetic wave propagation in different structures and media [10, 42, 43]. Since the solutions of integral equations are, in general, performed in the spatial domain using some numerical techniques, such as method of moments, finite element methods etc., computation of the spatial-domain Green's functions is crucial for the efficiency and accuracy of the numerical technique [11, 15, 44–48].

The spatial-domain Green's functions are usually obtained from their analytically expressible spectral-domain counterparts, and require the implementation of Hankel transform, which is also referred to as Sommerfeld integral in the literature. In case

of employing numerical quadrature in the implementation of the transformation, it is well-known and well-documented that the process becomes computationally expensive, mainly due to the oscillatory nature of the kernel of the transformation, rendering it almost impractical to use in conjunction with a numerical technique to solve the integral equations [15, 42]. As a viable and much more efficient alternative, analytical evaluation of the Hankel transforms of the exponential approximations of the spectral-domain Green's functions was proposed and referred to as the discrete-complex-image method (DCIM) [49, 50]. Upon its introduction with a rather restricted application domain, the method has been studied extensively, undergone a few major modifications and improvements [17–20, 25–28, 30, 32], and motivated a few other alternatives of similar nature [21–24, 29, 31]. However, two major issues have lingered for a long time: i) the lack of a proper error metric incorporated in the DCIM algorithm that would ensure the end result in the spatial domain, which was only very recently resolved [38]; and ii) an order selection algorithm, which will be the subject matter of this work.

Order selection, in the context of the DCIM when used to obtain the closed-form Green's functions in the spatial domain, implies the selection of the number of exponential terms used in the approximation, which has been generally decided by the user, no matter which version of the DCIM is employed. Since the decision is usually based on the number of dominant singular values obtained as the by-product of the DCIM, which has been implemented either by a direct user intervention or by setting up a threshold for a measure of dominance of the singular values in the code, there is no underlying theory or practical evidence that this approach provides an optimum number of terms in any measure. Although, with the latest improvement of the DCIM [38], the spatial-domain error is guaranteed to be smaller in the weighted least-squares sense as the number of terms increases, there is no guarantee that the choice of the number of the terms in the model is optimum. To remedy this shortcoming of the DCIM, a method known as the minimum description length (MDL) in the community of information theory has been adopted successfully [59–61]. The resulting DCIM,

referred to as DCIM with model order selection throughout this work, provides a choice of the model with the least code length, reflecting an optimal balance between the fitting error level versus model complexity. As an additional advantage of the method, this balance can be shifted by the user, if it is so desired, in favor of accuracy or computational cost, depending on the requirements of the problem at hand.

Since the proposed automatic order-selection in the DCIM is based on a model-selection algorithm, it would be instructive to provide its introduction in Section 3.2. Then, in Section 3.3, the MDL approach is combined with the latest version of the DCIM, i.e., the one with the spatial error criterion, to propose a fully automated, robust and accurate algorithm for obtaining the spatial-domain Green's functions in closed-forms. It is followed, in Section 3.4, by some numerical examples and discussions to assess the robustness and accuracy of the proposed combination for some typical geometries. Finally, some conclusions are provided in Section 3.5.

3.2. Model Selection

Model Selection refers to finding the most suitable choice of the model, from a set of candidates, that provides the “best” description of the limited observations. The MDL approach, among various alternatives in the literature (e.g. [62–64]), stands out as probably the most popular approach for the model selection. MDL was introduced by Jorma Rissanen [59] in 1978 as a concept in information theory, the idea of which originates from Kolmogorov's theory of algorithmic complexity and has received a significant interest within the statistics community. According to the MDL philosophy, the most suitable model is the one that would lead to the most compression in the representation of the data. The rationale behind this view is the following: the more regularities in the data, the more we can compress the data. Therefore, the model that best captures the regularities in data leads to the most compression. Formalizing this idea leads to a general theory for model selection with several properties such as; *i*) MDL finds a balance between goodness of the fit on the observed data

and complexity of the model, *ii*) MDL can be used to estimate both the parameters and the order of a model, *iii*) in MDL procedure data compression is equivalent to a form of maximum likelihood prediction and *iv*) in contrast to many other statistical methods, the MDL approach doesn't assume the existence of a "true" model but tries to find the most suitable candidate

If the candidate set for the model selection consists of the same family of functions with different orders, e.g. polynomials or mixture of exponentials as in DCIM, then, the corresponding problem is referred to as Model Order Selection. In this approach, the observed data is typically structured as

$$y^{(n)} = f^{(r)}(x^{(n)}; \Theta_r) + w^{(n)}, \quad n = 1, \dots, N \quad (3.1)$$

where

- $\{(x^{(n)}, y^{(n)}); n \in \{1, \dots, N\}\}$ is the pair of data points for which a model describing the mapping from $\{x_n; n \in \{1, \dots, N\}\}$ to $\{y_n; n \in \{1, \dots, N\}\}$ is sought,
- $f^{(r)}(x; \Theta_r)$ is the model function candidate of order r with parameters $\Theta_r \in \mathcal{C}^m$, and
- $w^{(n)}$ is the random noise sequence representing the fitting errors.

If the polynomial fitting problem is considered as an example, the model function corresponding to order r would have the form of

$$f^{(r)}(x; \Theta_r) = c^{(0)} + c^{(1)}x + c^{(2)}x^2 + \dots + c^{(r)}x^r, \quad (3.2)$$

where the model parameter vector can be written as

$$\Theta_r = \begin{bmatrix} c^{(0)} & c^{(1)} & \dots & c^{(r)} \end{bmatrix}^T, \quad (3.3)$$

with $m = r + 1$. More relevant to the DCIM, if the exponential fitting problem is considered, the model function corresponding to order r would be given by

$$f^{(r)}(x; \Theta_r) = \sum_{k=1}^r \beta^{(k)} e^{\alpha^{(k)}x}, \quad (3.4)$$

where the corresponding model parameter vector is written as follows:

$$\Theta_r = \left[\alpha^{(1)} \alpha^{(2)} \dots \alpha^{(r)} \beta^{(1)} \beta^{(2)} \dots \beta^{(r)} \right]^T, \quad (3.5)$$

with $m = 2r$.

The MDL principle is based on the fact that any set of data can be encoded by a string of symbols from a finite (say, binary) alphabet like prefix code. Given a probabilistic model, a certain number of bits is needed to encode the data according to Shannon's coding theorems. On the other hand however, one need to specify the model as well to complete the description and this will also require a certain number of bits. Therefore, the purpose becomes to minimize i) the length of the description of the data under a model of interest and ii) the description of that corresponding model. In this so-called two-step MDL approach [61], the complete description length becomes a kind of penalized maximum likelihood problem. More formally:

$\{\mathcal{H}^{(k)}; k \in \mathcal{Z}_+\}$ represents the list of the candidate models (hypotheses) for the given data, (in DCIM case, $\mathcal{H}^{(k)}$ represents the mixture of k exponentials), the best model H would minimize the following:

$$L(D) = L(D|H) + L(H), \quad (3.6)$$

where

- $L(H)$ is the numbers of bits required to describe the hypothesis which is the penalty term. (Increases with increasing order)
- $L(D|H)$ is the length (in bits) of the description of the data when encoded according to the hypothesis H . (Decreases with increasing order)
- $L(D)$ is the total number of bits to describe the data according to the chosen model.

To formalize L one needs to get familiar to the relation between the prefix code and Kraft's inequality which gives necessary and sufficient condition for the existence

of a uniquely decodable code and limits the length of the codewords in a prefix code [65]. Any binary tree can be viewed as defining a prefix code for the leaves of the tree. Kraft's inequality states that

$$\sum_{x \in A} 2^{-l_x} \leq 1 \quad (3.7)$$

where x is the leaves of the tree, i.e. the nodes without any children. l_x is the distance to the root node. The implication of the inequality is that each prefix code and the corresponding code lengths corresponds to a defective probability distribution. The word "defective" emphasizes the inequality. Indeed, the reverse implication of the Kraft's inequality is more important: Given a probability distribution (pmf) $p(x)$, we can define a prefix code, whose code lengths satisfy:

$$l_x = -\log(p(x)) \quad (3.8)$$

and for every pmf p , there exist a code with length $\log(p)$ and vice versa. In addition, if data is distributed according to p , then the codelength with lengths $\log(p)$ achieves the minimum expected codelength and if we use a prefix code corresponding to another pmf $q(x)$, we need to use extra bits according to $\log(q)$. This fact gives the idea that we can find a point hypothesis satisfying the minimum codelength for each hypothesis. According to this discussion, when we assume independent and identically distributed (i.i.d.) Gaussian vector $[w^{(1)} w^{(2)} \dots w^{(n)}]^T$, the conditional distribution for the data samples in (3.1) corresponding to Hypothesis $\mathcal{H}^{(r)}$ can be written compactly as

$$p_{\mathbf{y}}(\mathbf{y}|\mathbf{x}; \Theta_r, \sigma) = \frac{1}{(2\pi)^{N/2} \sigma^N} e^{-\frac{1}{2\sigma^2} \|\mathbf{y} - \mathbf{f}^{(r)}(\mathbf{x}; \Theta_r)\|_2^2}, \quad (3.9)$$

where \mathbf{x} and \mathbf{y} are the data sample vectors, $\mathbf{f}^{(r)}(\mathbf{x}; \Theta_r)$ is the model vector, and $\|\mathbf{a}\|_2 = \sqrt{\mathbf{a}^* \mathbf{a}}$ corresponds to the vector 2-norm for any $\mathbf{a} \in \mathcal{C}^N$. The length of the Shannon-Fano code [66] corresponding to this distribution is given by

$$L(D|\mathcal{H}^{(r)}; \Theta_r, \sigma) = -\log(p_{\mathbf{y}}(\mathbf{y}|\mathbf{x}; \Theta_r, \sigma)), \quad (3.10)$$

which is a function of the model vector $\Theta^{(r)}$ as well as the fitting error parameter σ . Note that the length expression in (3.10) corresponds to the negative log-likelihood

function [67], and it can be further simplified to

$$\begin{aligned} L(D|\mathcal{H}^{(r)}; \Theta_r, \sigma) &= \frac{N}{2} \log(2\pi) + N \log(\sigma) \\ &\quad + \frac{1}{2\sigma^2} \|\mathbf{y} - \mathbf{f}^{(r)}(\mathbf{x}; \Theta_r)\|_2^2, \end{aligned} \quad (3.11)$$

where the fitting error parameter σ can be treated either as an unknown, in which case it needs to be considered jointly with the model parameters Θ_r , or as a known parameter defined by a target accuracy level for the model fitting operation. The parameters of the model and σ (when assumed unknown) are selected to minimize the code length $L(D|\mathcal{H}^{(r)}; \Theta^{(r)}, \sigma)$, which corresponds to the maximization of the log-likelihood function, and therefore, to the Maximum-Likelihood (ML) solution for the corresponding model fitting problem [67]. Maximizing the log-likelihood function with respect to σ yields

$$\sigma = \left[\frac{1}{N} \|\mathbf{y} - \mathbf{f}^{(r)}(\mathbf{x}; \Theta_r)\|_2^2 \right]^{1/2} \quad (3.12)$$

As a result, the model-conditioned code length corresponding to the model $\mathcal{H}^{(r)}$ can be written as

$$\begin{aligned} L(D|\mathcal{H}^{(r)}; \Theta_{r,ML}, \sigma_{ML}) &= \frac{N}{2} (\log(2\pi) + 1) \\ &\quad + \frac{N}{2} \log\left(\frac{1}{N} \|\mathbf{y} - \mathbf{f}^{(r)}(\mathbf{x}; \Theta_{r,ML})\|_2^2\right) \end{aligned} \quad (3.13)$$

when σ is treated as an unknown parameter, and

$$\begin{aligned} L(D|\mathcal{H}^{(r)}; \Theta_{r,ML}) &= \frac{N}{2} \log(2\pi\sigma^2) \\ &\quad + \frac{1}{2\sigma^2} \|\mathbf{y} - \mathbf{f}^{(r)}(\mathbf{x}; \Theta_{r,ML})\|_2^2 \end{aligned} \quad (3.14)$$

when σ is specified based on a target fitting performance level. Since the goal is to get the total description length in (3.6), once the $L(D|H)$ component has been obtained in (3.13) and (3.14) for two different scenarios, the remaining term, i.e., the code length for the model parameters of $\mathcal{H}^{(r)}$, is given by

$$L(\mathcal{H}^{(r)}) = \frac{\kappa(\mathcal{H}^{(r)})}{2} \log(N) \quad (3.15)$$

where $\kappa(\mathcal{H}^{(r)})$ is the total number of effective real parameters used in the model. The expression in (3.15) is based on the assumption that the model parameters are estimated using N data samples. Therefore, the error variance in each parameter is proportional to $1/N$, corresponding to the assumed estimation accuracy whose logarithm determines the required bit precision for the parameter.

As a simple application seen in Fig. 3.1, a polynomial with order $r = 3$ is generated (solid line) and iid Gaussian noise is introduced to this polynomial (dotted line). Determining description length for different order of polynomials, it's seen in Fig. 3.2 that the minimum description length appears for the 3rd order polynomial. It is expected because MDL approach captures the regularity in the data for the third order polynomial fitting and as order increases the penalty dominates and description length increases.

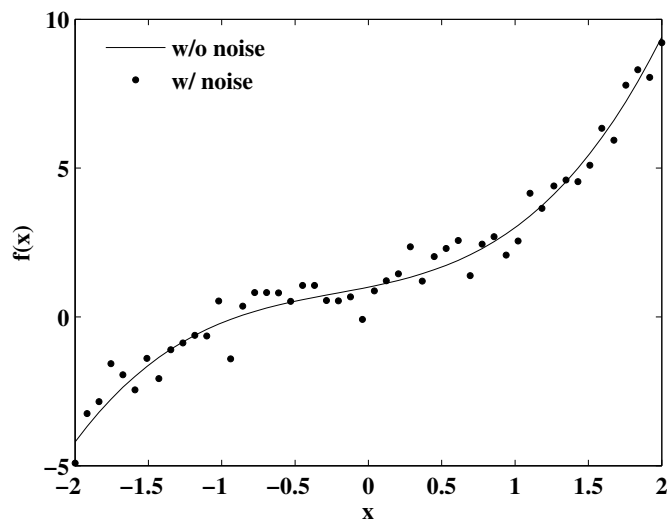


Figure 3.1: Third order polynomial with and without noise. Noise is iid gaussian with zero mean and $\sigma^2 = 0.01$

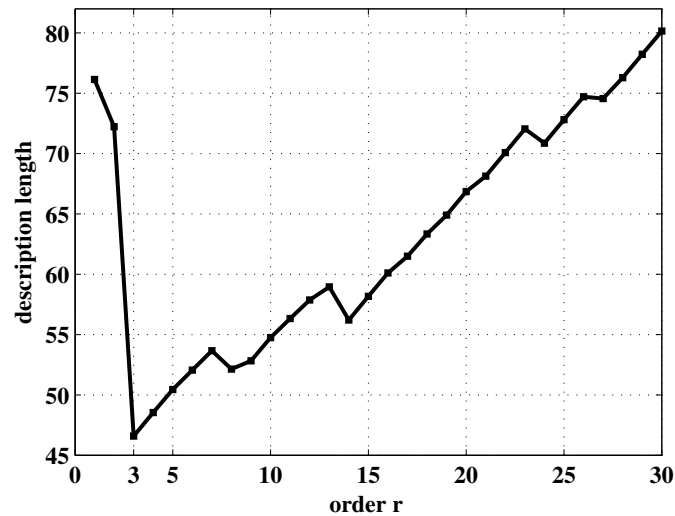


Figure 3.2: Description length vs. polynomial order. Minimum description length is achieved at $r = 3$.

MDL can also be applied to the exponential fitting problem via GPOF. In the previous example a polynomial fitting problem, which simply requires solution of an ordinary least square problem to find the coefficients of the polynomial is discussed. In this case however both the complex residues β_k 's and complex poles α_k 's are unknown and it requires nonlinear least square problem which makes the problem relatively more complicated. So in order to avoid nonlinear least square operation and since we had already had GPOF, the complex poles α_k 's are found from GPOF procedure and β_k 's are obtained by solving the ordinary least squares.

As an application, consider a pair of observations in Fig. 3.3 as shown with dots. The noise-free version of the signal is shown as a solid line in the figure and it is a sum of two cosine functions $f(x) = \cos(0.5x) + \cos(3x)$ which is a sum of 4 exponentials indeed. The noise added to the signal is iid Gaussian with zero mean and $\sigma^2 = 0.005$. In Fig. 3.4 description lengths for different hypotheses having different number of exponentials can be seen. Note that, MDL approach is able to capture the nature of the signal and reaches the minimum description length at the right number of residues, which is 4.

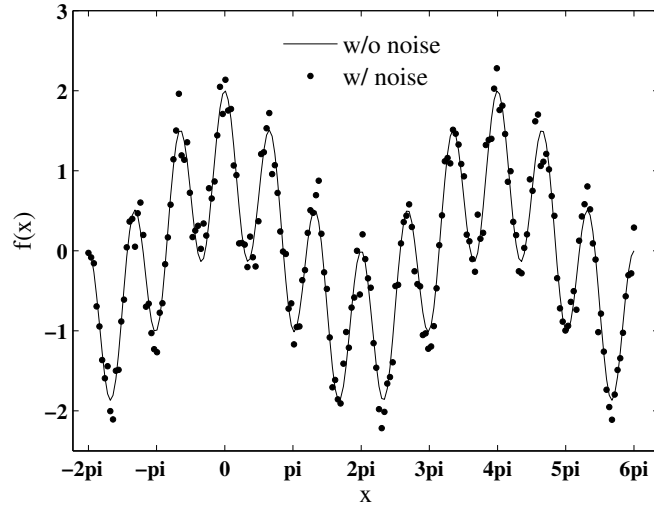


Figure 3.3: $f(x) = \cos(0.5x) + \cos(3x)$. Normally distributed iid noise with zero mean and $\sigma^2 = 0.005$

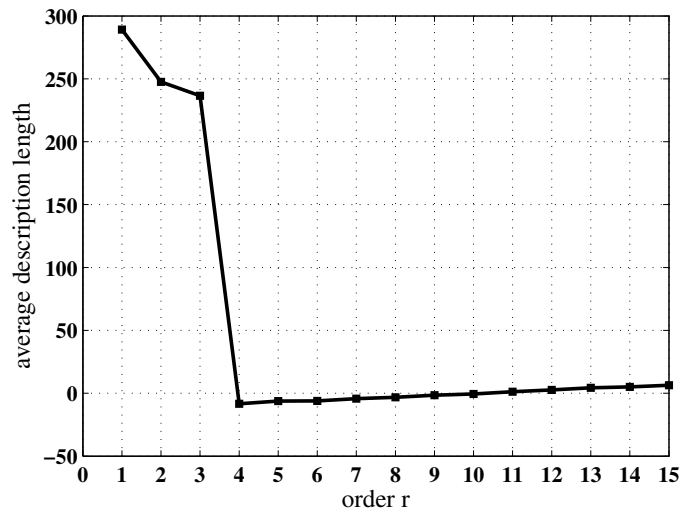


Figure 3.4: Average description length vs. number of exponentials. Minimum description length appears at $r = 4$ as expected.

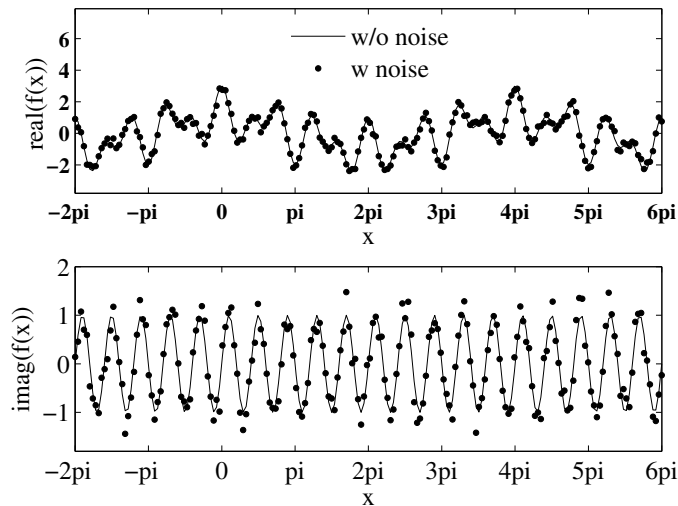


Figure 3.5: $f(x) = \cos(0.5x) + \cos(3x) + e^{5x}$. Normally distributed iid noise with zero mean and $\sigma^2 = 0.005$

As another application, consider a pair of observations in Fig. 3.5 which is a complex signal in this case. Similarly dotted ones are the observations with a complex noise (iid Gaussian with zero mean and $\sigma^2 = 0.005$) and the solid line is the original noise-free version of the signal. This time, the approximated function is $f(x) = \cos(0.5x) + \cos(3x) + e^{5x}$. As seen in Fig. 3.6, minimum description length is found when the order is 5, as expected.

3.3. DCIM with Model Order Selection

3.3.1. Brief Overview of DCIM

For the sake of illustration, consider a typical planar multi-layered structure as shown in Fig. 3.7, where the electromagnetic properties of the layers vary in z-direction only.

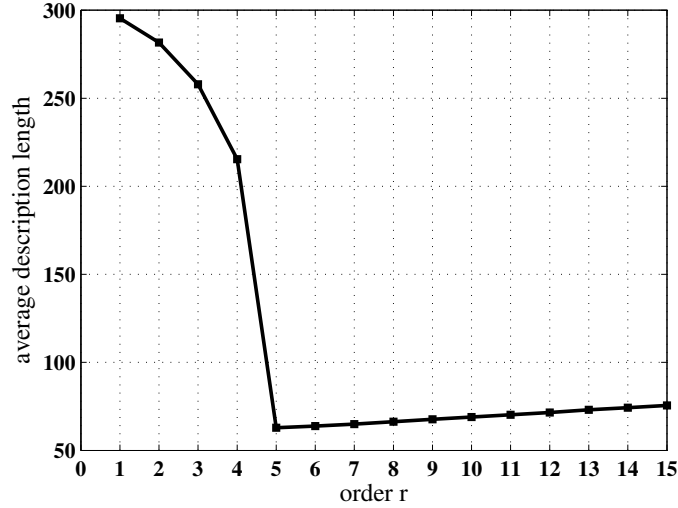


Figure 3.6: Average description length vs. number of exponentials. Minimum description length appears at $r = 5$.

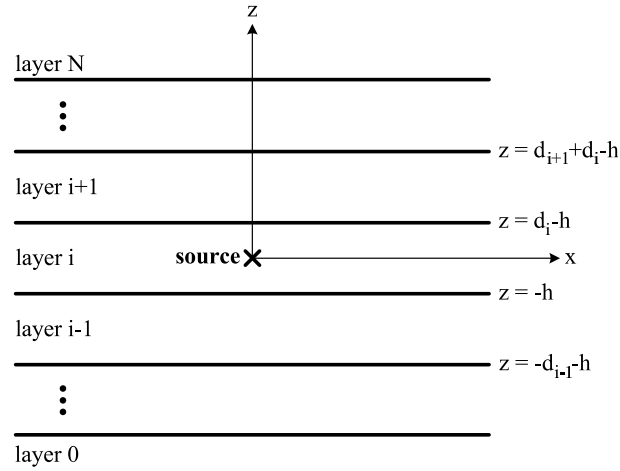


Figure 3.7: A general multilayer planar medium

Traditionally, Green's functions for planar layered media are obtained recursively as closed-form expressions in the spectral domain, and they are transformed to the spatial domain by the following Hankel transform integral (Sommerfeld integral):

$$g(\rho) = \frac{1}{2\pi} \int_S dk_\rho k_\rho J_0(k_\rho \rho) \tilde{G}(k_\rho) \quad (3.16)$$

where g and \tilde{G} are the spatial- and spectral-domain Green's functions, respectively, J_0

is a zeroth order Bessel function of the first kind and S denotes the integration path defined over the first quadrant in k_ρ -plane. Since it is generally computationally intensive to evaluate Sommerfeld integrals using numerical quadratures, the DCIM has been developed to avoid this expensive step by introducing two critical steps instead, which are, namely, i) the approximation of the spectral-domain Green's functions by the linear combinations of the complex exponentials, and ii) the evaluation of the resulting Sommerfeld integrals in closed forms using the Sommerfeld integral identity

$$\frac{e^{-jk_0 r}}{r} = \int_S dk_\rho k_\rho J_0(k_\rho \rho) \frac{e^{-jk_z z}}{jk_z} \quad (3.17)$$

where $r = \sqrt{\rho^2 + z^2}$ and $k_0 = \sqrt{k_\rho^2 + k_z^2}$. As a result, the spatial-domain Green's functions can be obtained analytically as a sum of complex images

$$\underbrace{\frac{1}{4\pi} \sum_{l=1}^M \alpha^{(l)} \frac{e^{-jk_0 r_i}}{r^{(l)}}}_{g(\rho)} = \frac{1}{2\pi} \int_S dk_\rho k_\rho J_0(k_\rho \rho) \underbrace{\frac{1}{2jk_z} \sum_{l=1}^M \alpha^{(l)} e^{-\beta^{(l)} k_z}}_{\tilde{G}(k_\rho)} \quad (3.18)$$

where $r^{(l)} = \sqrt{\rho^2 + (-j\beta^{(l)})^2}$ is a complex distance, due to which the method is referred to as discrete complex image method.

3.3.2. Automatic Order Selection for DCIM

According to the discussion in the previous section, central to the DCIM is the approximation of the spectral-domain Greens functions by rational exponential mixtures of the form

$$\tilde{G}_a(k_\rho; \Theta_r) = \sum_{l=1}^r \alpha^{(l)} \frac{e^{-\beta^{(l)} k_z}}{2jk_z} \quad (3.19)$$

where r is the order of the model corresponding to the number of exponentials used in the approximation, $\alpha^{(l)}$ and $\beta^{(l)}$ are the weights of the fractional terms and the

constants of the exponents, respectively, and $\Theta_r (= [\alpha^{(1)} \dots \alpha^{(r)} \beta^{(1)} \dots \beta^{(r)}]^T)$ is the model parameter vector.

By drawing an analogy from the generic data model in (3.1), the model fitting problem for the DCIM can be written as

$$\tilde{G}(k_\rho^{(n)}) = \tilde{G}_a^{(r)}(k_\rho^{(n)}; \Theta_r) + w^{(n)}, \quad n = 1, \dots, N. \quad (3.20)$$

where the fitting is performed for the spectral-domain points $\mathcal{K} = \{k_\rho^{(1)}, \dots, k_\rho^{(N)}\}$ defined over the integration path of the inverse Hankel transform operation in (3.16). Note that the minimization of the weighted 2-norm of the spatial-domain error of the Green's functions, for which the cost function was defined as

$$J(e) = \int_0^\infty \omega(\rho) |e(\rho)|^2 d\rho, \quad (3.21)$$

where $e(\rho)$ is the spatial error function, corresponding to the approximation procedure in DCIM, and $\omega(\rho)$ is the spatial weighting function, has recently been introduced as the optimization criterion for obtaining the model parameter vector Θ_r in [38]. In the same reference, it has also been demonstrated that this spatial-domain goal can be written as a spectral-domain optimization problem as

$$\begin{aligned} & \text{minimize} \quad \|\tilde{\mathbf{G}}(\mathbf{k}_\rho) - \tilde{\mathbf{G}}_a^{(r)}(\mathbf{k}_\rho; \Theta_r)\|_{\mathbf{\Gamma}_\mathcal{K}} \\ & \Theta_r \in \mathcal{C}^m \end{aligned} \quad (3.22)$$

where $\mathbf{\Gamma}_\mathcal{K} \in \mathcal{C}^{N \times N}$ is the positive definite weighting matrix, being a function of the spectral-domain samples \mathcal{K} , \mathbf{k}_ρ is the vector containing the elements in \mathcal{K} , $\tilde{\mathbf{G}}(\mathbf{k}_\rho)$ is the vector of the samples of the spectral-domain Greens functions, and $\tilde{\mathbf{G}}_a^{(r)}(\mathbf{k}_\rho; \Theta_r)$ is the vector containing the samples of the approximation model (of order r) corresponding to the model parameter vector Θ_r . The optimization problem in (3.22) targets the spectral shaping of the fitting errors such that the spatial-domain weighted error cost in (3.21) is minimized. Therefore, this procedure would be equivalent to the model fitting problem in (3.20) where the spectral model fitting noise vector

$$\mathbf{w} = \begin{bmatrix} w^{(1)} & w^{(2)} & \dots & w^{(N)} \end{bmatrix}^T \quad (3.23)$$

has the covariance $\sigma^2\mathbf{\Gamma}_{\mathcal{K}}^{-1}$, which corresponds to the independent fitting noise in the spatial domain following the discussion in [38]. Here σ target is a reflector of the fitting accuracy. The code length expressions for the data-conditioned model of order r in (3.13,3.14) should be accordingly modified as

$$\begin{aligned} L(D|\mathcal{H}^{(r)}; \mathbf{\Theta}_{r,ML}, \sigma_{ML}) &= \frac{N}{2}(\log(2\pi\det(\mathbf{\Gamma}_{\mathcal{K}}^{-1})) + 1) \\ &+ \frac{N}{2} \log\left(\frac{1}{N} \|\tilde{\mathbf{G}}(\mathbf{k}_{\rho}) - \tilde{\mathbf{G}}_a^{(r)}(\mathbf{k}_{\rho}; \mathbf{\Theta}_{r,ML})\|_{\mathbf{\Gamma}_{\mathcal{K}}}^2\right) \end{aligned} \quad (3.24)$$

when σ is treated as an unknown parameter, and

$$\begin{aligned} L(D|\mathcal{H}^{(r)}; \mathbf{\Theta}_{r,ML}) &= \frac{N}{2} \log(2\pi\sigma^2\det(\mathbf{\Gamma}_{\mathcal{K}}^{-1})) \\ &+ \frac{1}{2\sigma^2} \|\tilde{\mathbf{G}}(\mathbf{k}_{\rho}) - \tilde{\mathbf{G}}_a^{(r)}(\mathbf{k}_{\rho}; \mathbf{\Theta}_{r,ML})\|_{\mathbf{\Gamma}_{\mathcal{K}}}^2 \end{aligned} \quad (3.25)$$

when σ is specified. Note that the code length expressions given above assume that the $\mathbf{\Theta}_{r,ML}$ vector is obtained through the nonlinear least-squares procedure corresponding to the Maximum-Likelihood criterion, which is, in effect, equivalent to the optimization problem in (3.22). However, in the practical applications of the DCIM, a two-step approach is employed with the following brief descriptions of the steps: i) a subspace procedure such as GPOF [53] or ESPRIT [68] is used to obtain the constants of the exponents i.e., $\beta^{(l)}$'s; ii) the cost function in (3.22) is minimized with respect to the weighting parameters $\alpha^{(l)}$'s. This procedure typically achieves close approximation to the ML solution with more reasonable computational complexity, resulting in a parameter vector $\mathbf{\Theta}_{r,DCIM}$ to be used in evaluating the code lengths in (3.24) and (3.25).

For the code length computation of the model parameters for $\mathcal{H}^{(r)}$, one needs to consider mainly two different scenarios; single-level DCIM and multi-level DCIM. According to the single-level DCIM, since the same exponents and weighting parameters are used for the entire integration path, it results in $2r$ complex constants based on N sample points, leading to

$$L(\mathcal{H}^{(r)}) = 2r \log(N) \quad (3.26)$$

according to (3.15). However, in multi-level DCIM, the integration path is divided into L separate regions, for which there are separate numbers of samples N_k , separate orders r_k and separate parameter vectors Θ_{r_k} , for $k = 1, \dots, L$. Therefore, the model hypothesis in this case will be of the compound form, represented by $\mathcal{H}^{(r_1, r_2, \dots, r_L)}$. Although the exponents of a region are computed from the samples of that region alone, the weighting coefficients of all rational exponential mixtures are computed by a final weighted least squares performed over all the samples of the combined regions, as proposed in [38] to avoid the leakage caused by the independent weight optimizations. As a result, the code length for the hypothesis $\mathcal{H}^{(r_1, r_2, \dots, r_L)}$ can be written as

$$L(\mathcal{H}^{(r_1, r_2, \dots, r_L)}) = \underbrace{\sum_{k=1}^L r_k \log(N_k)}_{\text{for exponents}} + \underbrace{r \log(N)}_{\text{for weights}} \quad (3.27)$$

where $r = \sum_{k=1}^L r_k$ is the total order and $N = \sum_{k=1}^L N_k$ is the total number of samples on the integration path. Consequently, for a multi level DCIM with L levels, the total code length for the hypothesis $\mathcal{H}^{(r_1, r_2, \dots, r_L)}$ can be written as

$$\begin{aligned} L(D)^{(r)} &= \frac{N}{2} (\log(2\pi \det(\mathbf{\Gamma}_{\mathcal{K}}^{-1})) + 1) \\ &+ \frac{N}{2} \log\left(\frac{1}{N} \|\tilde{\mathbf{G}}(\mathbf{k}_\rho) - \tilde{\mathbf{G}}_a^{(r)}(\mathbf{k}_\rho; \Theta_{r, DCIM})\|_{\mathbf{\Gamma}_{\mathcal{K}}}^2\right) \\ &+ \sum_{k=1}^L r_k \log(N_k) + r \log(N) \end{aligned} \quad (3.28)$$

when σ is treated as an unknown parameter, and

$$\begin{aligned} L(D)^{(r)} &= \frac{N}{2} \log(2\pi \sigma^2 \det(\mathbf{\Gamma}_{\mathcal{K}}^{-1})) \\ &+ \frac{1}{2\sigma^2} \|\tilde{\mathbf{G}}(\mathbf{k}_\rho) - \tilde{\mathbf{G}}_a^{(r)}(\mathbf{k}_\rho; \Theta_{r, DCIM})\|_{\mathbf{\Gamma}_{\mathcal{K}}}^2 \\ &+ \sum_{k=1}^L r_k \log(N_k) + r \log(N) \end{aligned} \quad (3.29)$$

when σ is specified a priori. Therefore, the DCIM with model order selection involves choosing the model with the least code length, where the code length computation is based on the expressions in (3.28, 3.29).

The treatment of σ as a known or unknown parameter deserves a separate discussion. According to the proposed procedure, if σ is chosen as an unknown parameter, the DCIM with automatic order selection will return a prescribed σ value, in addition to the regional orders and parameters. This σ value would reflect the optimal balance point between the fitting error level versus model complexity according to the two-level MDL criterion. This choice may result in over-modeling with a fitting precision better than needed for the specific application. In order to reduce the implementation complexity of any EM simulation method that employs the closed-form Green's functions obtained by the proposed DCIM, one may specify a σ value, instead of treating it as an unknown. The user-specified σ value should depend on the accuracy and complexity requirements of the application. We can define a weighted signal to noise ratio (SNR)

$$SNR = \frac{\frac{1}{N} \|\tilde{\mathbf{G}}(k_\rho)\|_{\Gamma_\kappa}^2}{\frac{1}{N} \|\tilde{\mathbf{G}}(k_\rho) - \tilde{\mathbf{G}}_{\mathbf{a}}(k_\rho)\|_{\Gamma_\kappa}^2} \quad (3.30)$$

as an accuracy measure which is the ratio of average weighted energy of the spectral domain Green's function and fitting error. Therefore, for a chosen weighted SNR level, the target σ parameter can be computed as

$$\sigma_{target}^2 = \frac{\frac{1}{N} \|\tilde{\mathbf{G}}(k_\rho)\|_{\Gamma_\kappa}^2}{SNR_{target}}, \quad (3.31)$$

where the SNR_{target} is an application dependent parameter.

3.4. Results and Discussions

Once the theory and its possible scenarios have been thoroughly developed and studied in the previous section, its implementation and performance are provided in this section on some typical examples, chosen from rather difficult cases for the traditional DCIM. Before getting into the details of the results and discussions, it should be stated that the performance of the automatic order selection algorithm will be presented on the latest version of the DCIM only, namely the 3-level DCIM with

spatial error criterion [32, 38]. Although the algorithm has been tested on many different multilayered planar geometries with success, for the sake of brevity, only two geometries, which were considered as the most difficult ones for the traditional 2-level DCIM [31], are presented in this paper. It should also be noted that the proposed algorithm has been tested on the vector potentials (g^A) before and after extracting the surface wave poles (SWP), as the existence of SWPs makes the fitting difficult, while the Green's functions for scalar potentials (g^a) have been obtained only after extracting the SWPs, as SWPs often dominate the scalar potentials to a level that the DCIM can not capture the correct nature of the function, as discussed in [32].

To set the stage for the implementation of the proposed algorithm for the 3-level DCIM, note that the integration path is divided into three separate regions with three separate orders r_k for $k = 1, 2, 3$, and that the total code length of the hypothesis $\mathcal{H}^{(r_1, r_2, r_3)}$ is calculated by (3.28) and (3.29) with $L = 3$. Since the goal is to find the ternary order $\mathbf{r} = (r_1, r_2, r_3)$ that achieves the least code length, the code length computation is performed for all $r_k = 1, \dots, M_k$ and $k = 1, 2, 3$, and the minimum one among them is considered to be the minimum description length. Although the values of M_k for the three levels can be significantly narrowed down by educated guesses, they are chosen to be as large as possible in this study for the purpose of demonstration. Moreover, the proposed algorithm is implemented for both cases where σ is treated as an unknown and known parameter, using the equations in (3.28) and (3.29), respectively. In the case of unknown σ , the MDL algorithm returns the ternary order \mathbf{r}_{MDL} , together with a value for σ as

$$\sigma_{MDL} = \left[\frac{1}{N} \left\| \tilde{\mathbf{G}}(\mathbf{k}_\rho) - \tilde{\mathbf{G}}_a(\mathbf{k}_\rho; \Theta_{\mathbf{r}_{MDL}, DCIM}) \right\|_{\Gamma_K}^2 \right]^{\frac{1}{2}}, \quad (3.32)$$

while, in the case of predefined σ_{PRE} , the ternary order that gives the least code length is referred to as \mathbf{r}_{PRE} in this study. In addition, as briefly reviewed in Introduction, the performance of the traditional approach in determining the order of the model in DCIM, referred to as \mathbf{r}_{TRA} in this work, is also compared to the proposed algorithm.

Before proceeding with the details of the examples, it would be instructive to provide a brief summary of what has been done and how parameters have been named

in the tables and figures in this work:

1. the 3-level DCIM with automatic order selection is tested on g^A with and without SWP extraction, referred to as " g^A without SWP" and " g^A with SWP", respectively,
2. the 3-level DCIM with automatic order selection is tested on g^q with SWP extraction, referred to as " g^q without SWP",
3. \mathbf{r}_{MDL} and \mathbf{r}_{PRE} are the ternary orders achieving the minimum code length obtained from (3.28) and (3.29), respectively, and
4. \mathbf{r}_{TRA} is the ternary order found from the traditional approach.

As the first example, consider the geometry in Fig. 3.8 for which the Green's functions of the vector and scalar potentials, g_{xx}^A and g_x^q , respectively, are obtained at $f = 4.075 \text{ GHz}$ using the 3-level DCIM with spatial error criterion. For this setting, there is a TE-mode SWP with a rather small residue, resulting in a noticeable contribution only after very large distances, i.e., for large values of ρ . Therefore, the closed-form approximation of g_{xx}^A can be obtained from the proposed algorithm with and without extracting the SWP. However, since the TM-mode SWP contribution is quite dominant even in the intermediate distance from the source, a good fit for g_x^q can only be achieved after extracting the SWPs. Although it is suggested, as a general rule of thumb, that it is always a good practice to extract the SWPs from the spectral-domain Green's functions before the application of the DCIM [32], the vector-potential Green's function in this example has been treated both ways, just to demonstrate the performance of the order selection algorithm under rather difficult conditions. As a result, the performances of the order selections for the 3-level DCIM by the two MDL approaches, (3.28) and (3.29), and by the traditional approach for g_{xx}^A and g_x^q have been presented in Table 3.1. As observed from this example and many others, the MDL approach with unknown σ (σ_{MDL}) results in less or equal number of exponentials, in total, as compared to the number obtained from the traditional selection. It is fair to

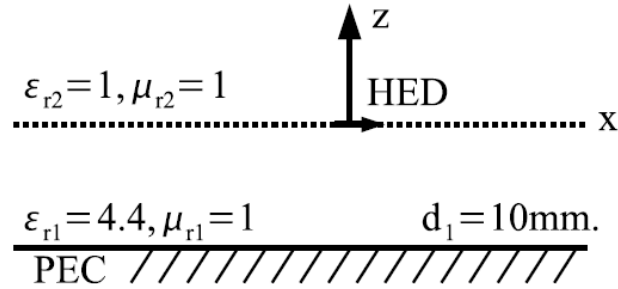
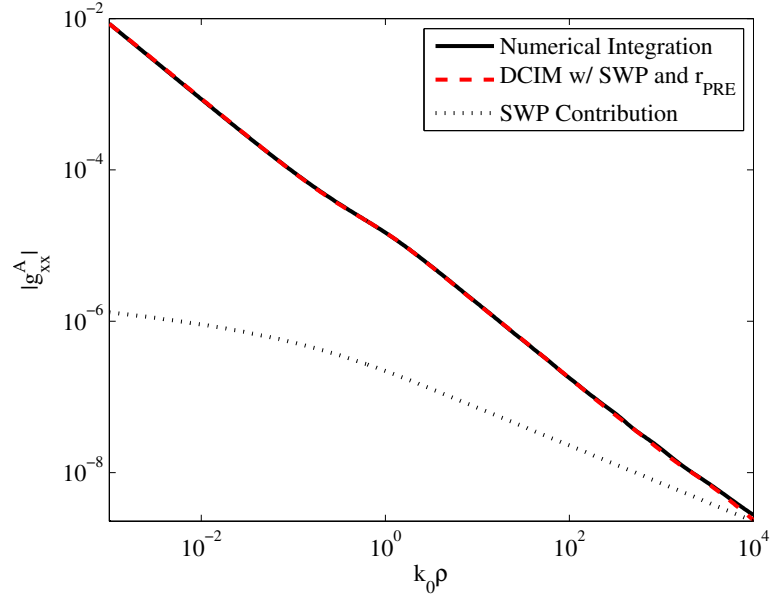


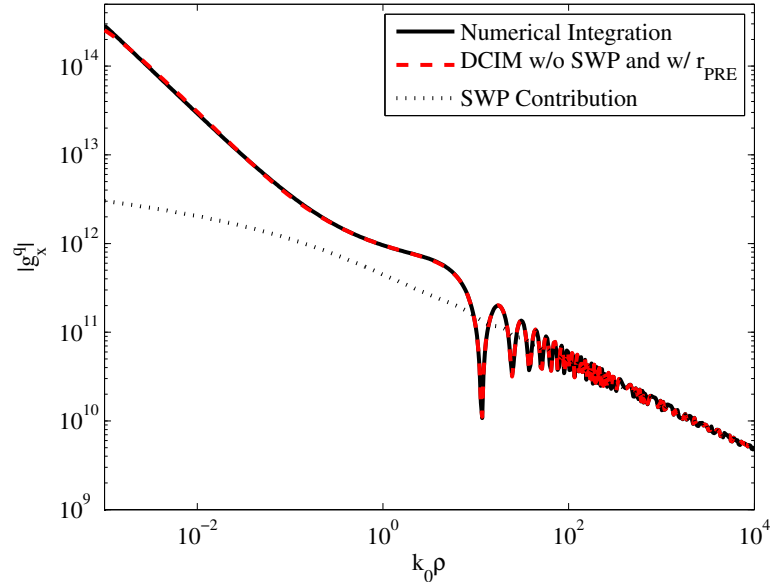
Figure 3.8: Geometry for Example-1 and Example-2. A PEC backed lossless dielectric material in free space.

state that, even before a priori target accuracy level of the approximation is defined by the user, the performance of the MDL approach is quite satisfactory and better than the traditional approach. Moreover, if one accepts, for a specific problem at hand, to work with some degree of inaccuracies in the end result by setting σ_{PRE} to $10^n \sigma_{MDL}$, the minimum code length is reduced drastically, resulting in significantly less number of exponentials, as expected. Of course, the choice of σ_{PRE} must be based on the trade-off between acceptable error for the problem and the computational cost of the algorithm. To demonstrate the robustness of the algorithm, the corresponding Green's functions obtained by the orders \mathbf{r}_{PRE} are presented in Fig.3.9, and compared to those obtained by the numerical integration of the transformation. It should be noted that even though the number of exponentials employed in the approximation has been significantly less than that of the ideal case, i.e., \mathbf{r}_{MDL} , the approximation has been quite successful as shown in Fig.3.9.

As a second example, the same geometry in Fig. 3.8 has been employed to study the algorithm at $f = 3.0 \text{ GHz}$, for which there is a dominant SWP for the TM modes while there is no SWP for TE modes, resulting in a dominant SWP contribution in the far field of g_x^q and a dominant branch point contribution in the far field of g_{xx}^A . As a result of this study, the order selections of the two MDL approaches and the traditional method have been provided in Table 3.2 for both g_{xx}^A and g_x^q with almost the same conclusion: the MDL algorithm with unknown σ ($= \sigma_{MDL}$) recommends a smaller number of exponentials in total as compared to the one from the traditional



(a)



(b)

Figure 3.9: Magnitudes of the Green's functions of a) the vectoral potential for $\mathbf{r}_{PRE} = (1, 2, 4)$; and b) the scalar potential for $\mathbf{r}_{PRE} = (1, 1, 2)$, for the geometry in Fig. 3.8. $f = 4.075GHz$, $\sigma_{PRE} = 10^3\sigma_{MDL}$.

Table 3.1: Order selection for the 3-level DCIM for the geometry in Fig. 3.8. $f = 4.075 \text{ GHz}$, $\sigma_{PRE} = 10^3 \sigma_{MDL}$.

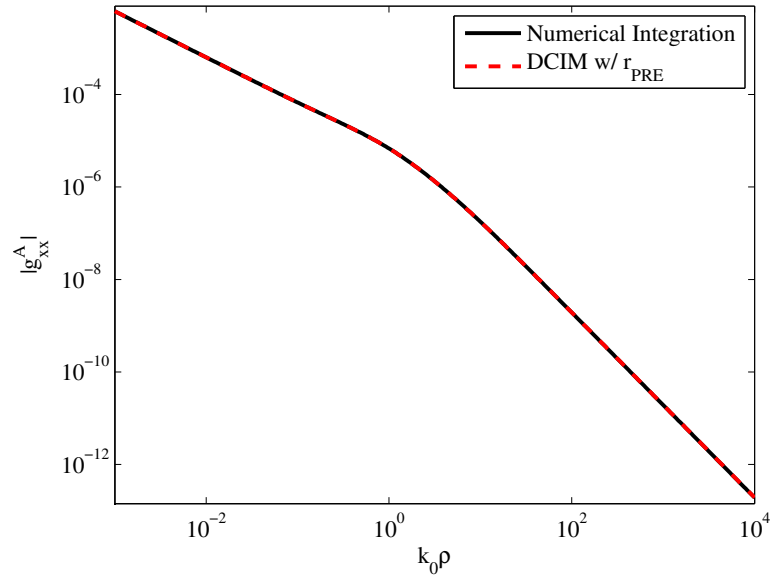
<i>Example-1</i>		g_{xx}^A		g_x^q
		w/ SWP	w/o SWP	w/o SWP
MDL	\mathbf{r}_{MDL}	3,22,15	10,20,16	9,13,17
	\mathbf{r}_{PRE}	1,2,4	3,9,11	1,1,2
\mathbf{r}_{TRA}		16,16,19	15,16,18	15,6,18

selection, and when the intended accuracy is sacrificed by choosing $\sigma_{PRE} = 10^3 \sigma_{MDL}$, the order \mathbf{r}_{PRE} is reduced significantly. To assess and to demonstrate the amount of error in the end result, that is, in the spatial-domain Green's functions, introduced by using the order \mathbf{r}_{PRE} (relaxing the fitting error parameter σ as compared to σ_{MDL}), the plots of the spatial-domain Green's functions obtained by the DCIM are provided for this choice with no noticeable difference, as shown in Fig. 3.10.

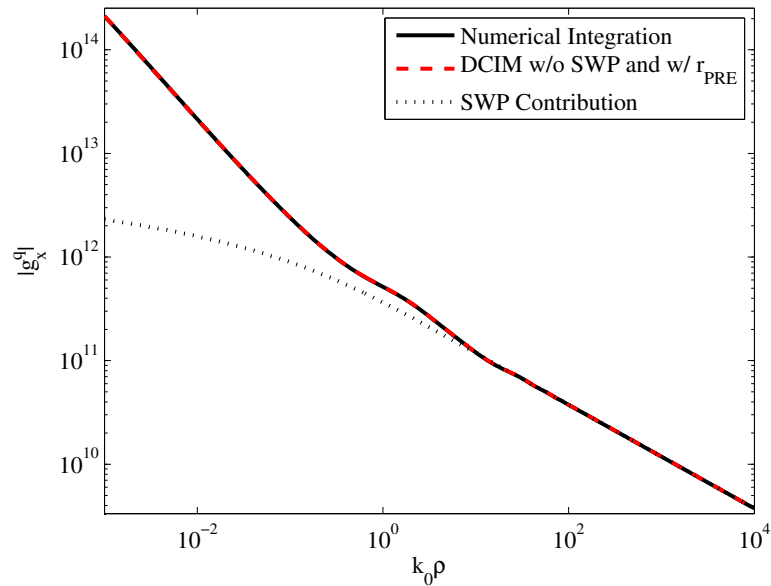
Table 3.2: Order selection for the 3-level DCIM for the geometry in Fig. 3.8. $f = 3 \text{ GHz}$, $\sigma_{PRE} = 10^3 \sigma_{MDL}$.

<i>Example-2</i>		g_{xx}^A	g_x^q
		no SWP	w/o SWP
MDL	\mathbf{r}_{MDL}	12,3,11	13,3,7
	\mathbf{r}_{PRE}	9,2,6	6,3,1
\mathbf{r}_{TRA}		16,10,8	13,3,12

As another example, consider a lossless PEC backed material in Fig. 3.11 for which the performance of the algorithm is tested at $f = 30 \text{ GHz}$. Although the geometry seem very similar to the one in the first example, there are TE- and TM-mode SWP's with quite large residues which makes their contributions highly dominant even in the intermediate distances from the source. Therefore a good fit for both g_{xx}^A and



(a)



(b)

Figure 3.10: Magnitude of the Green's functions of a) the vectoral potential for $\mathbf{r}_{PRE} = (9, 2, 6)$; and b) the scalar potential for $\mathbf{r}_{PRE} = (6, 3, 1)$, for the geometry in Fig. 3.8. $f = 3.0 \text{ GHz}$, $\sigma_{PRE} = 10^3 \sigma_{MDL}$.

g_x^q can be achieved only after extracting the SWP's. As a result, the performances of the order selections of the two MDL approaches and the traditional method have been provided in Table 3.3 for both g_{xx}^A and g_x^q . In this example, the MDL algorithm with unknown σ ($= \sigma_{MDL}$) recommends a slightly higher number of exponentials on total as compared to the one in the traditional method, however the order \mathbf{r}_{PRE} is reduced significantly, when the complexity requirement is adjusted by choosing $\sigma_{PRE} = 10^3 \sigma_{MDL}$. To demonstrate the possible maximum of error in the spatial domain Green's function, the plots of the Green's functions for vector and scalar potential are obtained by the choices of \mathbf{r}_{PRE} and demonstrated in Fig. 3.12(a) and 3.12(b) respectively. Note that, even with this choice the results agree with the ones obtained by the numerical integration.

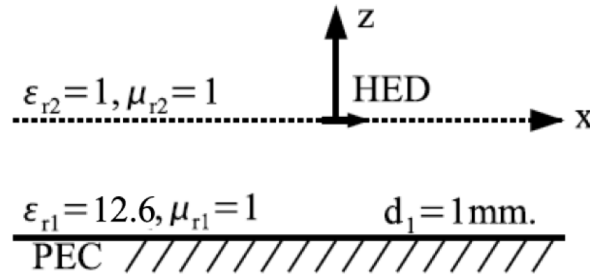
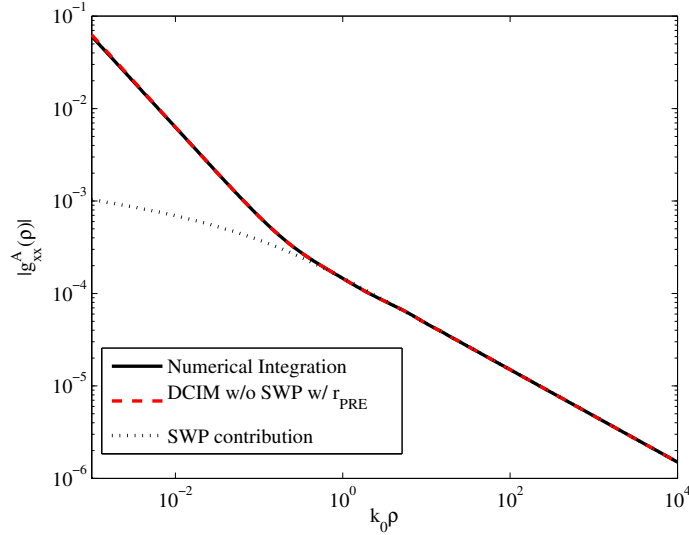


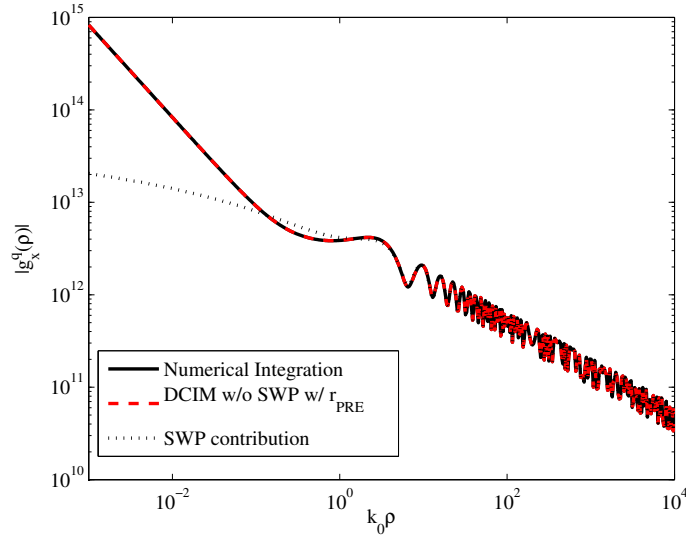
Figure 3.11: Geometry for Example-3. A lossless PEC backed material.

Table 3.3: Order selection for the 3-level DCIM for the geometry in Fig. 3.11. $f = 30 \text{ GHz}$, $\sigma_{PRE} = 10^3 \sigma_{MDL}$.

<i>Example-3</i>		g_{xx}^A	g_x^q
		w/o SWP	w/o SWP
MDL	\mathbf{r}_{MDL}	18,30,5	17,11,18
	\mathbf{r}_{PRE}	7,4,6	7,2,10
\mathbf{r}_{TRA}		16,4,3	15,5,11



(a)



(b)

Figure 3.12: Magnitude of the Green's functions of a) the vector potential for $\mathbf{r}_{PRE} = (7, 4, 6)$; and b) the scalar potential for $\mathbf{r}_{PRE} = (7, 2, 10)$, for the geometry in Fig. 3.11 . $f = 30 \text{ GHz}$, $\sigma_{PRE} = 10^3 \sigma_{MDL}$.

As another example, the geometry shown in Fig. 3.13 is studied at $f = 10 \text{ GHz}$, for which the SWP contribution is quite significant in the near field for both g_{xx}^A and g_x^q , even though the SWP contribution decays exponentially and the branch-point con-

tribution determines the behavior of the Green's functions for $\rho \rightarrow \infty$ in this example. Therefore, it is difficult to capture the behavior of the Green's functions unless the SWPs are extracted. To study the influence of the SWPs on the proposed algorithm, the order selection has been performed for g_{xx}^A without extracting the SWPs, which inevitably increases the order selected by all the variants of the algorithm, Table 3.4. Note that while σ_{PRE} is chosen as $\sigma_{PRE} = 10^3 \sigma_{MDL}$ when the SWPs are extracted, it would be reasonable to choose the fitting error parameter σ closer to the ideal case σ_{MDL} when the SWPs are not extracted, by setting $\sigma_{PRE} = \sqrt{10} \sigma_{MDL}$, because of the nature of the waves supported by the geometry in such cases. As observed in Table 3.4, the MDL algorithm with σ_{MDL} suggests slightly more number of exponentials in total compared to the traditional approach, while the MDL algorithm with σ_{PRE} results in significantly reduced order without causing any noticeable deterioration in the spatial-domain Green functions, as shown in Fig. 3.14.

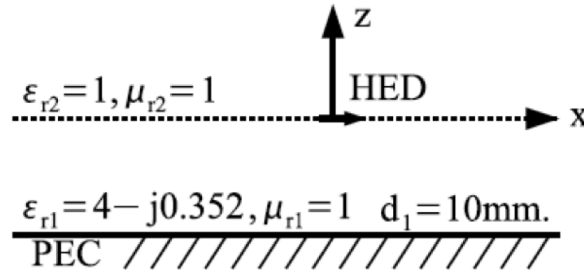
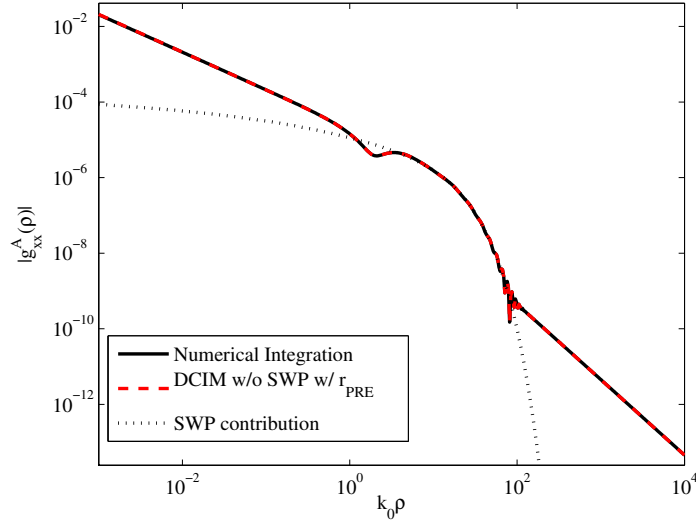


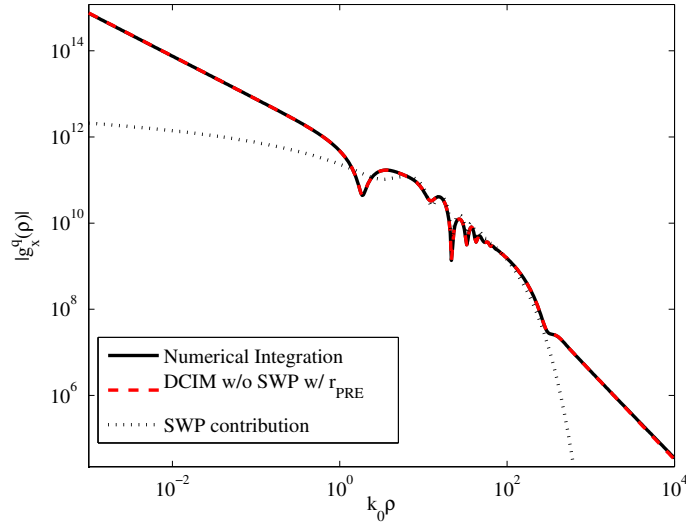
Figure 3.13: Geometry for Example-4. A lossy PEC backed material.

Table 3.4: Order selection for the 3-level DCIM for the geometry in Fig. 3.13. $f = 10 \text{ GHz}$, $\sigma_{PRE} = \sqrt{10}\sigma_{MDL}$ when SWPs are not extracted, $\sigma_{PRE} = 10^3\sigma_{MDL}$ when SWPs are extracted..

<i>Example-4</i>		g_{xx}^A		g_x^q
		w/ SWP	w/o SWP	w/o SWP
MDL	\mathbf{r}_{MDL}	9,37,19	15,25,18	19,24,13
	\mathbf{r}_{PRE}	6,34,17	7,4,5	11,3,11
\mathbf{r}_{TRA}		16,24,15	15,7,11	15,5,17



(a)



(b)

Figure 3.14: Magnitude of the Green's functions of a) the vector potential for $\mathbf{r}_{PRE} = (7, 4, 5)$; and b) the scalar potential for $\mathbf{r}_{PRE} = (11, 3, 11)$, for the geometry in Fig. 3.13. $f = 10 \text{ GHz}$, $\sigma_{PRE} = 10^3 \sigma_{MDL}$.

As the final example, the geometry shown in Fig. 3.15 is studied at $f = 4.0 \text{ GHz}$, for which the SWP contribution is quite significant in the near field for both g_{xx}^A and g_x^q similar to the previous example. Similarly, even though the SWP contribution is

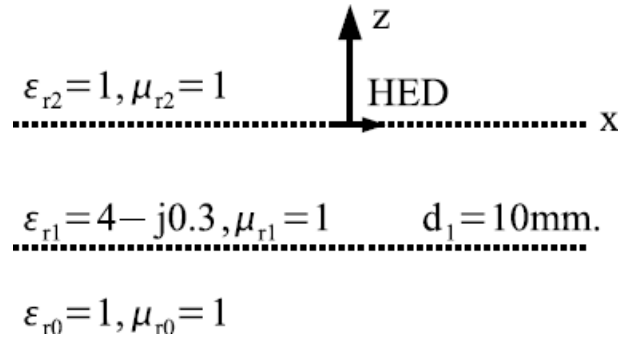
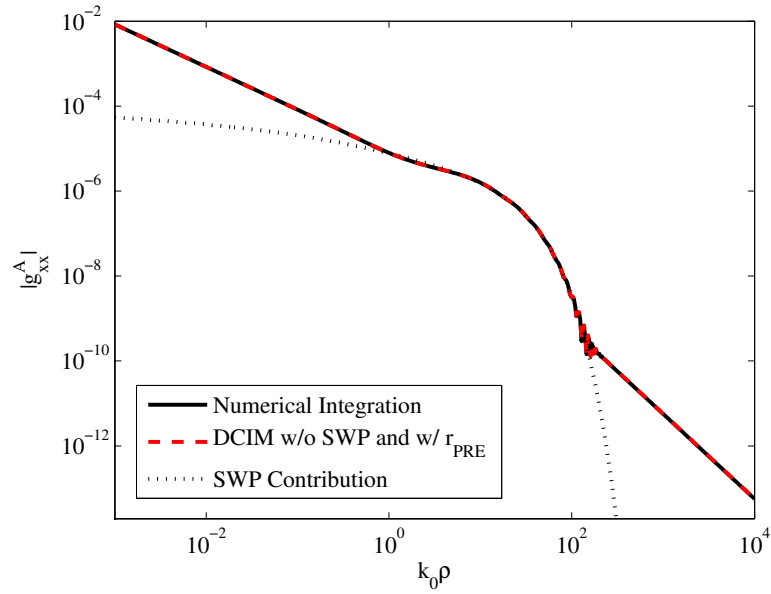


Figure 3.15: Geometry for Example-5. A lossy material in air.

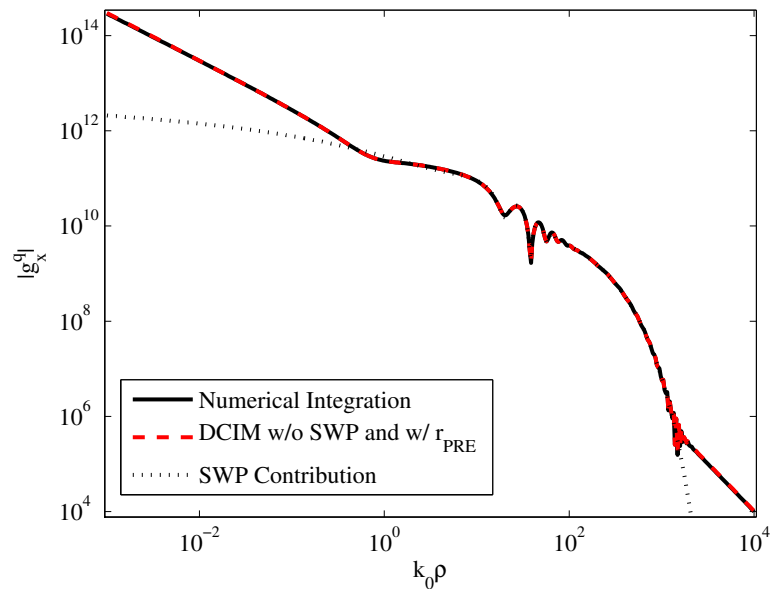
Table 3.5: Order selection for the 3-level DCIM for the geometry in Fig. 3.15. $f = 4\text{GHz}$, $\sigma_{PRE} = \sqrt{10}\sigma_{MDL}$ when SWPs are not extracted, $\sigma_{PRE} = 10^3\sigma_{MDL}$ when SWPs are extracted.

Example-5		g_{xx}^A		g_x^q
		w/ SWP	w/o SWP	w/o SWP
MDL	\mathbf{r}_{MDL}	7,38,16	18,3,14	18,10,16
	\mathbf{r}_{PRE}	5,34,12	7,5,10	8,2,7
\mathbf{r}_{TRA}		14,27,15	15,4,9	15,5,13

dominating in the intermediate distance from the source, eventually the SWP contribution decays and the branch-point contribution determines the behavior of the Green's functions in the far field region. Therefore, it is difficult to capture the behavior of the Green's functions unless the SWPs are extracted. Note that while σ_{PRE} is chosen as $\sigma_{PRE} = 10^3\sigma_{MDL}$ when the SWPs are extracted, it would be reasonable to choose the fitting error parameter σ closer to the ideal case σ_{MDL} when the SWPs are not extracted, by setting $\sigma_{PRE} = \sqrt{10}\sigma_{MDL}$. As observed in Table 3.5, the MDL algorithm with σ_{MDL} suggests slightly more number of exponentials in total compared to the traditional approach, while the MDL algorithm with σ_{PRE} results in significantly reduced order. As shown in Fig. 3.16, the choice obtained by σ_{PRE} does not cause any noticeable deterioration in the spatial-domain Green functions.



(a)



(b)

Figure 3.16: Magnitude of the Green's functions of a) the vector potential for $\mathbf{r}_{PRE} = (7, 5, 10)$; and b) the scalar potential for $\mathbf{r}_{PRE} = (8, 2, 7)$, for the geometry in Fig. 3.15. $f = 4.0 \text{ GHz}$, $\sigma_{PRE} = 10^3 \sigma_{MDL}$.

For the sake of completeness, the additional error introduced by relaxing the fitting error parameter σ is studied for all the Green's functions and the results for g_{xx}^A with the SWP extracted in example-3 have been provided for three different selections of σ_{PRE} in Fig. 3.17. In this study, the error is defined by the absolute value of the difference between the spatial-domain Green's function for the orders of \mathbf{r}_{PRE} and \mathbf{r}_{MDL} as normalized to that for \mathbf{r}_{MDL} , that is, $|g(\rho, \sigma_{PRE}) - g(\rho, \sigma_{MDL})|/|g(\rho, \sigma_{MDL})|$. Note that, for this specific example, the following orders corresponding to the different fitting error parameters σ have been provided by the MDL algorithm: $\mathbf{r}_{MDL} = (18, 3, 14)$, and $\mathbf{r}_{PRE} = (12, 5, 7)$ for $\sigma_{PRE} = 10\sigma_{MDL}$, $\mathbf{r}_{PRE} = (11, 3, 8)$ for $\sigma_{PRE} = 10^2\sigma_{MDL}$ and $\mathbf{r}_{PRE} = (7, 5, 10)$ for $\sigma_{PRE} = 10^3\sigma_{MDL}$. From this study, it is observed that, once the SWPs have been extracted, the choice of the fitting error parameter σ plays a significant role in order selection while introducing negligible error in the end result. For all the cases studied so far, provided SWPs are extracted a priori, the choice of $\sigma_{PRE} = 10^3\sigma_{MDL}$ works quite well in optimizing accuracy and the description length. It would be worth mentioning that although the total numbers of exponentials corresponding to $\sigma_{PRE} = 10^2\sigma_{MDL}$ and $\sigma_{PRE} = 10^3\sigma_{MDL}$ are the same, their distributions over the three regions of the 3-level DCIM differ, providing more emphasis to the regions where the amplitudes are relatively large, as σ gets large.

After providing the performance of the algorithm on some typical examples, it is worth to note that, in this study the error relaxation is performed by using the orders of magnitudes of σ_{MDL} , as σ_{MDL} has already been obtained in (3.32). Alternatively, the user can set an SNR level depending on the application as discussed in Section 3.3.

3.5. Conclusion

After having introduced the 3-level DCIM that can take different wave natures into account and that can provide an error metric to ensure the accuracy of the end result, the only remaining hurdle was the manual selection of the order of the approximation.

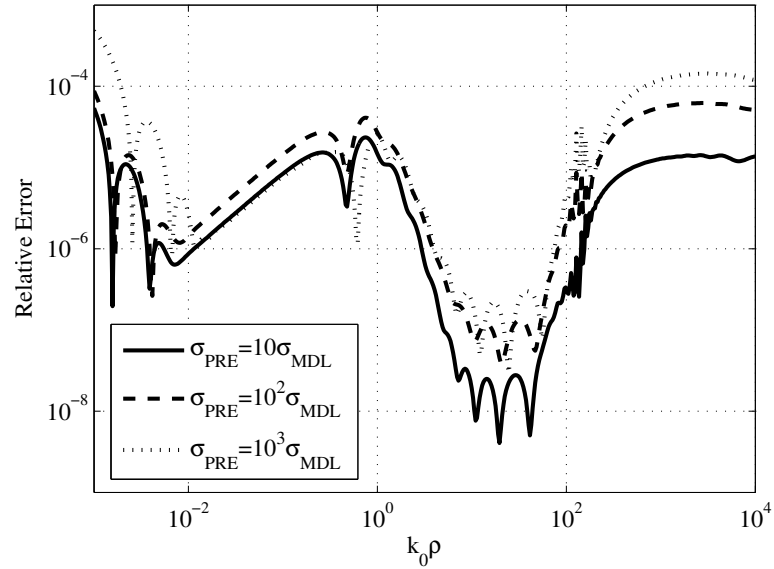


Figure 3.17: Relative error in g_{xx}^A (example-3) introduced by the choice of different error parameters σ as compared to the parameter provided by the algorithm itself. $\mathbf{r}_{MDL} = (18, 3, 14)$, and $\mathbf{r}_{PRE} = (12, 5, 7)$ for $\sigma_{PRE} = 10\sigma_{MDL}$, $\mathbf{r}_{PRE} = (11, 3, 8)$ for $\sigma_{PRE} = 10^2\sigma_{MDL}$ and $\mathbf{r}_{PRE} = (7, 5, 10)$ for $\sigma_{PRE} = 10^3\sigma_{MDL}$.

In this work, an order selection algorithm based on the minimum description length has been introduced, and demonstrated on some typical examples that it can easily be implemented with success. Based on the cases studied during this work, it would be safe to state that the DCIM with automatic order selection usually suggests less or equal number of exponentials than the ones decided manually in the traditional approach. More importantly, since the MDL approach, exploiting the regularities in the data, selects the order of the model based on a trade-off between the quality of fitting and complexity of the model, it guarantees the accuracy of the fitting as contrary to the traditional approach. Furthermore, this approach allows the user to modify the trade-off between the accuracy and the complexity in favor of one of the two, depending on the requirements of the actual problem at hand. It is inevitable that such a flexibility comes with a price tag; it requires some sort of input from the user, perhaps in the form of SNR according to which a target fitting error parameter σ can be computed. However, it was found out that while the choice of the parameter

had a significant influence on the order of the model, it is not critical for the accuracy of the end result, provided the SWPs have been extracted in advance. The method with all its variants was successfully applied to many different geometries and different components of the Green's functions.

Chapter 4

A Novel MoM-based Approach for Accurate and Efficient Analysis of 2D Structures

4.1. Introduction

With the advent of high-speed digital computers together with the sophisticated computer languages, many powerful numerical analysis and design methods have been promptly developed to solve EM problems which do not have analytical solutions. Among many other numerical methods, MoM, FEM and FDTD come into prominence for solving EM scattering problems. These methods basically transform differential, integral or integro-differential equations, which are originated from the Maxwell's equations, into a set of algebraic equations. Therefore the performance of these methods rely on the way of getting the algebraic equations and the size of the resulting matrix equation. Particularly, MoM used for the solution of the integral equations is the preferred choice for the EM analysis of open field problems for structures in 2D free space which are the main motivation of this study.

The accurate and fast analysis of dielectric and or metallic structures is crucial

to understand physical mechanisms involved in and design of many devices; such as antennas, microstrip lines, photonic band gap materials, left handed materials or other coupled geometries operating in different ranges of frequencies. For instance, for the characterization of photonic crystals, many analysis techniques such as the plane wave method [69–71] use the periodicity property of these structures and analyze only a single periodic unit which increases computational efficiency. Therefore they are applicable only to infinitely extent periodic structures and introducing defects reduces their efficiency significantly. However, periodic structures such as left handed materials and photonic band gap materials are finite in reality and most of their significance arise from defects which are imperfections generated intentionally to control and manipulate the propagation of electromagnetic waves. Producing defects into periodic structures provides development of many devices such as waveguides, waveguide crossings, channel drop filters, defect lasers, laser cavities, dynamic photonic crystals etc. To analyze these open structures, neither FEM nor FDTD based numerical simulation tools are suitable since the entire space of interest must be discretized that arises their computational time dramatically. On the other hand, MoM is a good candidate for an efficient method since the discretization is performed over the scatterer only.

In this study, a numerically efficient technique based on the spatial-domain MoM to the solution of EFIE in conjunction with exponential approximation method is developed for the analysis of 2D geometries in free space. The efficiency of the method is achieved by obtaining only two analytical expressions for all entries of the MoM matrix in which the indexes of the basis and testing functions are included explicitly. Therefore the matrix entries are obtained by evaluating one of the two expressions for the corresponding indices of the matrix. In addition extending and/or modifying the geometry do not require re-calculation of MoM matrix entries i.e., one needs to evaluate the corresponding expression only for the new indices of the added or modified portion of the geometry. The idea of the study is inspired by one of the proposed methods in [34] for which the EM characterization of the planar structures

in the multilayered media is obtained by a technique based on the spectral-domain MoM for the solution of MPIEs. In [34] the resulting spectral-domain MoM matrix entries are single integrals over an infinite domain which results from the testing procedure. To evaluate the integral, its integrand, except for the exponential term, is approximated in terms of complex exponentials and by getting the inverse Fourier transform with the help of the Sommerfeld integral identity, a closed form expression is obtained analytically. In addition, a single closed-form expression becomes valid for all entries which is the main advantage of the method. The geometry in [34] leads the unknown functions to be the functions of a single variable since the structures are planar and extending infinitely on the plane. Therefore the variation occurs in one dimension only and hence testing procedure requires a single integral. However for 2D structures the testing procedure in the spectral domain results in double integrals over the infinite domain to implement the boundary conditions in two-dimensional space. Therefore we employ the spatial-domain MoM instead of the spectral-domain one. The spatial-domain MoM for a 2D structure in free space yields a quinary integral; two for the convolution of the basis and Green's functions and two for the testing procedure. Since these integrals are definite over a finite domain, they can be evaluated analytically. The only integral left without to be evaluated comes from the expression of the spatial-domain Green's function which is written intentionally as the inverse Fourier transform of the known spectral-domain Green's function. As a result, the integral is evaluated in a similar manner discussed in [34].

Since the proposed method is a MoM based approach, it would be instructive to briefly review the key steps of the MoM in Section 4.2 and it is followed, in Section 4.3, by the general EFIE derivation in free space. Section 4.4 provides the MoM formulation and field calculation for the 2D structures by separating the discussions for TE and TM excitation modes together with the discussions of basis and testing function selections. In Section 4.5, the analyses of some 2D geometries performed by the proposed MoM approach are compared to the results of a reference simulation tool, called *Comsol Multiphysics* by Comsol Inc., for verification and finally some

conclusions are drawn in Section 4.6.

4.2. The Method of Moments

MoM is a general numerical approach to solve an operator equation, such as differential, integral and integro-differential equations. In general an operator equation can be defined as follows [10]:

$$\mathbf{L}f = g, \quad (4.1)$$

where \mathbf{L} is a linear operator, g is a known excitation or forcing function and f is the unknown function to be determined. Since there is usually no closed-form solution for the problem, f is approximated. If MoM is used to approximate the solution of the operator equation, some certain steps are followed:

1. Expand the unknown function using a set of known functions with unknown coefficients

$$f = \sum_{n=1}^N a_n B_n, \quad (4.2)$$

where B_n 's for $n = 1, \dots, N$ are the basis functions and a_n 's are unknown weighting coefficients. Since the operator \mathbf{L} is linear, (4.2) is substituted into (4.1) as

$$\sum_{n=1}^N a_n \mathbf{L}B_n = g. \quad (4.3)$$

2. Choose a set of testing functions T_m (or also called as the weighting functions) and define an inner product (or also called as moment) between the basis and the testing functions for each pair such as

$$\sum_{n=1}^N a_n \langle T_m, \mathbf{L}B_n \rangle = \langle T_m, g \rangle \quad (4.4)$$

for each T_m , $m = 1, \dots, N$. The inner product is defined as

$$\langle u, v \rangle = \int_{\Omega} uv^* d\Omega, \quad (4.5)$$

where $*$ and Ω denote the complex conjugate and the domain of integration, respectively. The domain of the integration can be line, surface or volume integrals depending on the basis and testing functions hence the structure of the problem itself. As a result, (4.4) yields $N \times N$ matrix equation

$$\mathbf{Z}\mathbf{a} = \mathbf{b}, \quad (4.6)$$

where $\mathbf{Z}_{mn} = \langle T_m, \mathbf{L}B_n \rangle$, $b_m = \langle T_m, g \rangle$ and unknown coefficient vector $\mathbf{a} = [a_1 a_2 \dots a_N]^T$.

3. Solve the matrix equation for the unknown coefficient vector \mathbf{a} and substitute the coefficients into (4.2) to find the unknown function f .

It is important to note that the second step of the MoM procedure is nothing but a residual minimization process which is the main reason for employing testing operation. In the mathematical point of view, MoM formalizes the orthogonal projections in Hilbert space to find the best solutions in subspaces [35]. When the residual (i.e. error) R is written as the difference between the exact and the approximate function such as

$$R = \mathbf{L}f - \sum_{n=1}^N a_n \mathbf{L}B_n = g - \sum_{n=1}^N a_n \mathbf{L}B_n, \quad (4.7)$$

the minimum residual can be obtained by setting its projection over the range space of the operator to zero. This is equivalent to setting the inner product of the residual with a set of testing functions, spanning the range space of the operator, to zero:

$$\langle T_m, R \rangle = \langle T_m, g \rangle - \left\langle T_m, \sum_{n=1}^N a_n \mathbf{L}B_n \right\rangle = 0 \quad (4.8)$$

for $m = 1, \dots, N$. Note that (4.8) yields exactly the same relation in (4.4), leading a set of linear equations for the unknown coefficients.

For the sake of the MoM performance, the selection of basis and testing functions are quite important. There exist various functional forms of the basis and testing functions such as, piecewise constant (pulse) functions, piecewise triangular (rooftop) functions, piecewise sinusoidal functions, Rao-Wilton-Glisson (RWG) basis functions

etc. These functions are called local or sub-sectional basis functions since they span a local region. If basis function spans the entire problem domain, they are called global or entire-domain basis functions. Some basis functions are sophisticated and therefore while they reduce the size of the matrix equation, they increase the complexity of the MoM formulation. The simple basis functions may need relatively more discretization however they yield simpler MoM formulations and ease of use. No matter how simple or complex the basis function is, the most crucial issue for the choice of the basis function is its capability to match the physical form of the actual unknown function. If the basis function cannot represent the actual behavior of the function the MoM may not converge even if the number of basis functions is increased dramatically. The testing functions are the weighting functions defined in the regions where the boundary conditions are set by the inner product operation. The method using the delta function as the testing function is referred as point matching which is the simplest testing procedure in MoM. For the MoM application, in which the basis functions themselves are used as the testing functions, is called Galerkin's method which is one of the most common choices for testing functions. For the cases in which a piecewise function is used for testing as in the Galerkin's method, the boundary conditions are applied throughout the solution domain rather than setting the boundary conditions at the discrete points as in the point matching. This usually increases the accuracy of the solution.

4.3. Theory and General Formulation in Free Space

It is well known that a dielectric structure which is exposed to electromagnetic waves becomes polarized and induces a scattered field. The scattered field can be considered as the radiation by the equivalent polarization currents \bar{J} in the dielectric structure. Hence, the sum of the scattered field and the incident field gives the total field at any point of interest

$$\bar{E}^t(\bar{r}) = \bar{E}^s(\bar{J}, \bar{r}, V) + \bar{E}^i(\bar{r}), \quad (4.9)$$

where the superscripts t , s and i denote total, scattered and incident fields, respectively. The scattered field can be expressed in terms of potentials

$$\bar{E}^s(\bar{J}, \bar{r}, V) = -j\omega\bar{A}(\bar{r}) - \nabla\phi(\bar{r}), \quad (4.10)$$

where \bar{A} and ϕ are vector and scalar potentials, respectively. The potentials can in turn be represented in terms of convolution of the induced polarization current and Green's function of the structure such as

$$\bar{A} = \mu_0 G * \bar{J}, \quad (4.11)$$

$$\phi = \frac{1}{\epsilon_0} G * \rho \quad (4.12)$$

where G is the spatial domain Green's function for the electric field and ρ is the charge density of the structure. By substituting (4.11) and (4.12) into (4.10) and applying continuity relation, the scattering field is rewritten as a quantity totally dependent on the induced polarization current

$$\bar{E}^s = -j\omega\mu_0 G * \bar{J} + \frac{\nabla}{j\omega\epsilon_0} (G * \nabla \cdot \bar{J}). \quad (4.13)$$

On the other hand, inside a dielectric in a background medium of free-space, the dielectric flux density \bar{D} is equal to

$$\bar{D} = \epsilon_0 \bar{E}^t + \bar{P}, \quad (4.14)$$

where the polarization \bar{P} is the electric dipole moment per unit volume. Since the polarization current \bar{J} is the time rate of change of \bar{P}

$$\bar{J} = \frac{\partial}{\partial t} \bar{P}, \quad (4.15)$$

and in turn the polarization current can be related to the electric flux density inside the dielectric in (4.14) through

$$\bar{J} = \frac{\partial}{\partial t} [\bar{D} - \epsilon_0 \bar{E}^t] \quad (4.16)$$

the following expression is obtained

$$\bar{J} = \frac{\partial}{\partial t} [\epsilon \bar{E}^t - \epsilon_0 \bar{E}^t]. \quad (4.17)$$

for linear media, where $\bar{D} = \epsilon \bar{E} = \epsilon_r \epsilon_0 \bar{E}$.

For the time harmonic fields with the time convention $e^{j\omega t}$, the equivalent polarization currents can be related to the total electric field by

$$\bar{J} = j\omega(\epsilon - \epsilon_0)\bar{E}^t = jk_0 Y_0(\epsilon_r - 1)\bar{E}^t \quad (4.18)$$

where $Y_0 = 1/Z_0$ is the intrinsic admittance of free-space. Therefore, the total electric field can be expressed by the induced polarization current [72]

$$\bar{E}^t = \frac{\bar{J}}{jk_0 Y_0(\epsilon_r - 1)}. \quad (4.19)$$

As a result, the total electric field and the scattering field are represented by the equivalent polarization current which becomes the only unknown of the problem. Leaving the incident field at righthand side as the known quantity and substituting (4.13) and (4.19) into (4.9) yields the general electric field integral equation (EFIE)

$$\frac{\bar{J}}{jk_0 Y_0(\epsilon_r - 1)} + j\omega\mu_0 G * \bar{J} - \frac{\nabla}{j\omega\epsilon_0} (G * \nabla \cdot \bar{J}) = \bar{E}^i, \quad (4.20)$$

which is the operator equation of MoM, describing the problem mathematically. The application of MoM for the solution of the polarization current begins at this point with expanding the unknown polarization current in terms of known basis functions with unknown coefficients, and it is followed by the testing procedure to convert the integral equation into a set of algebraic equations. In the following sections the application of MoM for 2D structures is elaborated and the problem is presented for TE and TM modes.

4.4. MoM Analysis of 2D structures

To provide a perspective about the method, consider a 2D dielectric rod (extending infinitely in one dimension; z direction in this study) excited by an incident time-harmonic plane wave as shown in Fig. 4.1. Note that since the geometry is invariant

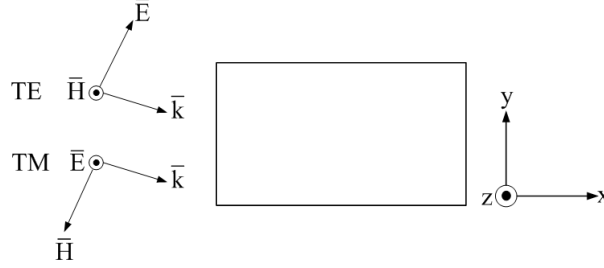


Figure 4.1: A single dielectric rod in a background medium of free-space extending in z direction. The direction of electric and magnetic fields are shown for TE and TM mode excitations.

to changes in z -direction, all quantities are a function of x and y . Under the excitation of a plane wave whose magnetic field is in-plane and electric field is parallel to z -axis (TM to z excitation), only the polarization current J_z is induced, so that the only unknown of MoM for TM to z mode becomes the coefficients representing J_z . On the other hand, the electric field is on xy plane and magnetic field is parallel to z axis for TE to z mode excitation, therefore MoM application requires solving two EFIE's to find J_x and J_y . In addition, the solution of the EFIE's of TE to z is more sophisticated and needs a deliberate selection of basis and testing function compared to TM to z mode. Therefore TM to z and TE to z mode analyses deserve separate discussions. For the sake of brevity, TM to z and TE to z modes will be called as shortly TM and TE modes, respectively, throughout this study.

4.4.1. TM Mode

TM mode excitation induces an electric current $\bar{J} = J_z(x, y)\hat{z}$ which becomes the only unknown to be found from MoM. Due to the fact that the induced electric current is z -directed and all quantities are invariant to z direction, the divergence of the induced current $\nabla \cdot \bar{J}$ in (4.20) is zero. As a result, the general EFIE is reduced down to

$$\bar{E}_z^t - \bar{E}_z^s = \frac{J_z(x, y)}{jk_0 Y_0(\epsilon_r(x, y) - 1)} + j\omega\mu_0 G(x, y) * J_z(x, y) = E_z^i. \quad (4.21)$$

For the solution of the equivalent polarization current J_z , the first step of MoM is to expand J_z in terms of known basis functions with unknown coefficients

$$J_z(x, y) = \sum_{m=1}^{N_x} \sum_{n=1}^{N_y} I_{zmn} B_m(x) B_n(y), \quad (4.22)$$

where N_x and N_y are the number of subsections of width h_x and h_y for x and y directions, respectively and B_m and B_n are piecewise constant functions defined for each subsection such as

$$B_m(x) = \begin{cases} 1, & (m - \frac{1}{2})h_x < x < (m + \frac{1}{2})h_x, \\ 0, & \text{otherwise} \end{cases} \quad (4.23)$$

and

$$B_n(y) = \begin{cases} 1, & (n - \frac{1}{2})h_y < y < (n + \frac{1}{2})h_y. \\ 0, & \text{otherwise} \end{cases} \quad (4.24)$$

After the representation of J_z in terms of basis functions, total and scattered fields will be in the following forms

$$E_z^t = \sum_{m=1}^{N_x} \sum_{n=1}^{N_y} I_{zmn} \frac{B_m(x) B_n(y)}{jk_0 Y_0 (\epsilon_r - 1)} \quad (4.25)$$

and

$$E_z^s = \sum_{m=1}^{N_x} \sum_{n=1}^{N_y} -I_{zmn} j\omega\mu_0 \int_{(m-\frac{1}{2})h_x}^{(m+\frac{1}{2})h_x} \int_{(n-\frac{1}{2})h_y}^{(n+\frac{1}{2})h_y} B_m(x') B_n(y') G(x, y; x', y') dx' dy'. \quad (4.26)$$

As the second step of MoM, the testing procedure leads to a set of linear equations, which are obtained by taking the inner product of both sides of (4.21):

$$\langle T_{m'n'}(x, y), E_z^t(x, y) \rangle - \langle T_{m'n'}(x, y), E_z^s(x, y) \rangle = \langle T_{m'n'}(x, y), E_z^i(x, y) \rangle \quad (4.27)$$

for all $m' = 1$ to N_x and $n' = 1$ to N_y . Here $T_{m'n'}$ is the testing function (i.e., weighting function) and is chosen to be the same as the basis functions which leads to the commonly known Galerkin MoM:

$$T_{m'n'}(x, y) = B_{m'}(x) B_{n'}(y) \quad (4.28)$$

For the sake of simplicity, the inner products of the testing functions with total, scattered and incident electric fields will be evaluated separately:

$$\begin{aligned} \langle T_{m'n'}, E_z^t \rangle &= \sum_{m=1}^{N_x} \sum_{n=1}^{N_y} I_{zmn} \int_{(m'-\frac{1}{2})h_x}^{(m'+\frac{1}{2})h_x} \int_{(n'-\frac{1}{2})h_y}^{(n'+\frac{1}{2})h_y} \frac{T_{m'n'}(x, y) B_m(x) B_n(y)}{jk_0 Y_0(\epsilon_r - 1)} dx dy \\ &= \sum_{m=1}^{N_x} \sum_{n=1}^{N_y} I_{zmn} \frac{h_x h_y}{jk_0 Y_0(\epsilon_r - 1)} \delta_{m'm, n'n} \end{aligned} \quad (4.29)$$

$$\begin{aligned} \langle T_{m'n'}, E_z^s \rangle &= \sum_{m=1}^{N_x} \sum_{n=1}^{N_y} -I_{zmn} j\omega\mu_0 \int_{(m'-\frac{1}{2})h_x}^{(m'+\frac{1}{2})h_x} \int_{(n'-\frac{1}{2})h_y}^{(n'+\frac{1}{2})h_y} \\ &\times \int_{(m-\frac{1}{2})h_x}^{(m+\frac{1}{2})h_x} \int_{(n-\frac{1}{2})h_y}^{(n+\frac{1}{2})h_y} T_{m'n'}(x, y) B_m(x') B_n(y') G(x, y; x', y') dx dy dx' dy' \end{aligned} \quad (4.30)$$

$$\begin{aligned} \langle T_{m'n'}, E_z^i \rangle &= E_{oz} \int_{(m'-\frac{1}{2})h_x}^{(m'+\frac{1}{2})h_x} B_{m'}(x) e^{-jk_{x0}x} dx \int_{(n'-\frac{1}{2})h_y}^{(n'+\frac{1}{2})h_y} B_{n'}(y) e^{-jk_{y0}y} dy \\ &= E_{oz} h_x h_y e^{-j(k_{x0}m'h_x + k_{y0}n'h_y)} \text{sinc}(k_{x0}h_x/2) \text{sinc}(k_{y0}h_y/2) \end{aligned} \quad (4.31)$$

where the incident electric field for TM case is $E_z^i = E_{oz} e^{-j(k_{x0}x + k_{y0}y)}$ and E_{oz} is the amplitude of the incident field. Here $k_0 = \sqrt{k_{x0}^2 + k_{y0}^2}$ is the free space wave number.

Note that, while (4.29) and (4.31) are obtained by evaluating the definite integrals, the integration in (4.30) has not been carried out yet. It requires employing the Green's function of the system together which the complexity of the integration will be investigated in detail in the following sections.

Green's Function for a Line Source

In general, integral equations are the equations with the unknown functions under the integral operator. Specifically, integral equations in electromagnetics are basically integral representations of the field quantities in terms of superposition of the current

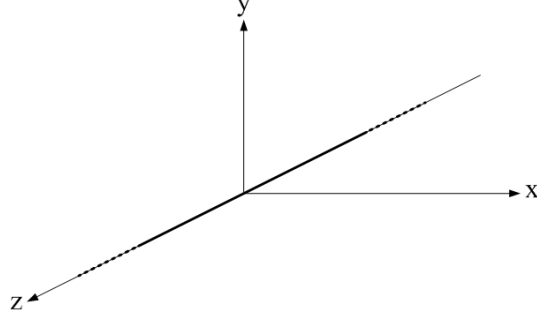


Figure 4.2: A line source at the origin

densities and Green's functions as in (4.13). Therefore, the structure of Green's function is very crucial to obtain integral equations and to apply MoM. For 2D structures, Green's function is considered as the resulting electric field due to a line source, extending to infinity in an unbounded medium as in Fig. 4.2. As the uniformity of the source along z -direction in free space, Green's function due to the line source vary only in xy plane. The expression of the Green's function used in this study originates from the assumption that a one-dimensional Fourier transform of the Green's function exists with the following definition of the Fourier transform pairs

$$G(x, y) = \frac{1}{2\pi} \int_{-\infty}^{+\infty} dk_x \tilde{G}(k_x, y) e^{-jk_x x} \quad (4.32)$$

$$\tilde{G}(k_x, y) = \int_{-\infty}^{+\infty} dx G(x, y) e^{jk_x x} \quad (4.33)$$

where one of the space variables, here y , is fixed and Fourier transform is performed over the other variable. As it is found in [43], the spectral domain Green's function is found as

$$\tilde{G}(k_x, y) = \frac{1}{j2k_y} e^{jk_y |y|} \quad (4.34)$$

which yields

$$G(x, y) = \frac{1}{2\pi} \int_{-\infty}^{+\infty} dk_x \frac{e^{-j(k_x x + k_y |y|)}}{j2k_y} \quad (4.35)$$

if the line source is located at the origin as in Fig. 4.2. The general case yields

$$G(x, y; x', y') = \frac{1}{2\pi} \int_{-\infty}^{+\infty} dk_x \frac{e^{-jk_x(x-x') - jk_y(|y-y'|)}}{j2k_y}. \quad (4.36)$$

Note that due to the uniqueness of the solution of the Green's function, an equivalent expression could be derived by fixing x variable and performing Fourier transform over y as well.

Evaluation of the inner product term $\langle T_{m'n'}, E_z^s \rangle$

Once the Green's function of the problem is specified, (4.30) becomes more clear, yet some set of integration operations must be carried out. For simplicity, we separate integration part of the inner product $-\langle T_{m'n'}, E_z^s \rangle$ and substitute Green's function in (4.36) into that term and reordering it as follows

$$\frac{1}{\pi} \int_{-\infty}^{+\infty} \frac{dk_x}{k_y} \frac{\omega \mu_0}{4} \underbrace{\int_{(m-\frac{1}{2})h_x}^{(m+\frac{1}{2})h_x} \int_{(m-\frac{1}{2})h_x}^{(m+\frac{1}{2})h_x} B_{m'}(x) B_m(x') e^{-jk_x(x-x')} dx dx'}_{T_1} \times \underbrace{\int_{(n-\frac{1}{2})h_y}^{(n+\frac{1}{2})h_y} \int_{(n-\frac{1}{2})h_y}^{(n+\frac{1}{2})h_y} B_{n'}(y) B_n(y') e^{-jk_y|y-y'|} dy dy'}_{T_2} \quad (4.37)$$

where the terms T_1 and T_2 are definite integrals the solutions of which are the functions of k_x and k_z

$$T_1(k_x) = h_x^2 e^{-jk_x(m'-m)h_x} \text{sinc}^2(k_x h_x / 2) \quad (4.38)$$

and

$$T_2(k_x) = \begin{cases} h_y^2 e^{-jk_y|n'-n|h_y} \text{sinc}^2(k_y h_y / 2), & \text{if } |n' - n| \geq 1; \\ \frac{2h_y}{jk_y} \left\{ 1 - e^{-jk_y h_y / 2} \text{sinc}(k_y h_y / 2) \right\}, & \text{if } n' = n. \end{cases} \quad (4.39)$$

Note that, T_2 can be considered a k_x dependent function due to the relation of $k = \sqrt{k_x^2 + k_y^2}$.

The remaining integral in (4.37) is over infinite k_x domain which can not be evaluated analytically. Therefore it requires numerical integration which is computationally expensive due to the slowly convergent and oscillatory behavior of the integrand. Therefore instead of taking the numerical integration, if the integrand (apart from

$1/k_y$ and exponential terms) can be approximated in terms of complex exponentials, the analytical evaluation of (4.37) can be achieved via the following integral identity [42]

$$H_0^{(2)}(k_\rho \rho) = \frac{1}{\pi} \int_{-\infty}^{+\infty} \frac{dk_x}{k_y} e^{-jk_x(x-x')-jk_y|y-y'|} \quad (4.40)$$

where $H_0^{(2)}$ is second kind of Hankel function of zero order with $\rho = \sqrt{(x-x')^2 + |y-y'|^2}$.

To clarify the idea a general case can be discussed. Suppose the term $F(k_x)$ in the expression below

$$\frac{1}{\pi} \int_{-\infty}^{+\infty} \frac{dk_x}{k_y} e^{-jk_x x} e^{-jk_y y} F(k_x) \quad (4.41)$$

is approximated as sum of complex exponentials such as

$$F(k_x) = \sum_t a_t e^{-\alpha_t k_y}, \quad (4.42)$$

then the integral of interest in (4.41) can be evaluated by using the integral identity in (4.40) as follows

$$\frac{1}{\pi} \int_{-\infty}^{+\infty} \frac{dk_x}{k_y} e^{-jk_x x} e^{-jk_y y} \sum_t a_t e^{-\alpha_t k_y} = \sum_t a_t \frac{1}{\pi} \int_{-\infty}^{+\infty} \frac{dk_x}{k_y} e^{-jk_x x} e^{-jk_y(y-j\alpha_t)} = \sum_t a_t H_0^{(2)}(k_\rho \rho_t) \quad (4.43)$$

where $\rho_t = \sqrt{(x^2 + (y - j\alpha_t)^2)}$.

By the light of this example, the integral in (4.37) can also be obtained in the same manner. Here, the exponential approximation is very crucial to evaluate the inner product terms containing the Green's function and it is performed by a Prony like exponential approximation technique (GPOF) [73] together with two level approach [19].

Finally, the terms in (4.27) are derived by analytical evaluation for E_z^t and E_z^i and by the exponential approximation for E_z^s . Note that to find the polarization current we obtain an algebraic equation which can be written in matrix form

$$\begin{bmatrix} \mathbf{Z} \end{bmatrix} \begin{bmatrix} \mathbf{I}_z \end{bmatrix} = \begin{bmatrix} \mathbf{R} \end{bmatrix} \quad (4.44)$$

where $\mathbf{I}_z = [I_{z11} \dots I_{zN_x N_y}]^T$ is the vector for the unknown polarization currents and $\mathbf{R} = [\langle T_{11}, E_z^i \rangle \dots \langle T_{N_x N_y}, E_z^i \rangle]^T$ is the excitation vector.

Due to the region dependency of T_2 , the terms to be approximated in MoM matrix \mathbf{Z} differ and the matrix entries are derived accordingly as follows:

1. For $|n' - n| \geq 1$:

$$\begin{aligned}
 Z_{m'n',mn} &= \frac{\omega\mu_0}{4} h_x^2 h_y^2 \frac{1}{\pi} \int_{-\infty}^{+\infty} \frac{dk_x}{k_y} e^{-jk_x(m'-m)h_x} e^{-jk_y|n'-n|h_y} \\
 &\quad \times \text{sinc}^2(k_x h_x/2) \text{sinc}^2(k_y h_y/2) \\
 &= \frac{\omega\mu_0}{4} h_x^2 h_y^2 \frac{1}{\pi} \int_{-\infty}^{+\infty} \frac{dk_x}{k_y} e^{-jk_x(m'-m)h_x} e^{-jk_y|n'-n|h_y} \sum_t a_t e^{-\alpha_t k_y} \\
 &= \frac{\omega\mu_0}{4} h_x^2 h_y^2 \sum_t a_t H_0^{(2)}(k\rho_t)
 \end{aligned} \tag{4.45}$$

where $\rho_t = \sqrt{((m' - m)h_x)^2 + (|n' - n|h_y - j\alpha_t)^2}$;

2. For $n' = n$:

$$\begin{aligned}
 Z_{m'n',mn} &= \frac{h_x h_y}{jk_0 Y_0(\epsilon_r - 1)} \delta_{m'm} + \frac{\omega\mu_0}{4} h_x^2 h_y^2 \frac{1}{\pi} \int_{-\infty}^{+\infty} \frac{dk_x}{k_y} e^{-jk_x(m'-m)h_x} \\
 &\quad \times \text{sinc}^2(k_x h_x/2) \frac{2}{jk_y h_y} \left[1 - e^{-jk_y h_y/2} \text{sinc}(k_y h_y/2) \right] \\
 &= \frac{h_x h_y}{jk_0 Y_0(\epsilon_r - 1)} \delta_{m'm} + \frac{\omega\mu_0}{4} h_x^2 h_y^2 \frac{1}{\pi} \int_{-\infty}^{+\infty} \frac{dk_x}{k_y} e^{-jk_x(m'-m)h_x} \sum_t a_t e^{-\alpha_t k_y} \\
 &= \frac{h_x h_y}{jk_0 Y_0(\epsilon_r - 1)} \delta_{m'm} + \frac{\omega\mu_0}{4} h_x^2 h_y^2 \sum_t a_t H_0^{(2)}(k\rho_t)
 \end{aligned} \tag{4.46}$$

where $\rho_t = \sqrt{((m' - m)h_x)^2 + (-j\alpha_t)^2}$.

It should be noted that, with this approach the MoM matrix entries can be represented in closed forms with the help of the exponential approximation. Most importantly, the matrix elements do not have different closed form expressions, on the contrary only two closed form expressions are valid for all entries. Therefore it is sufficient to perform GPOF approximation twice in order to fill the entire MoM matrix.

This makes the approach very efficient in getting the entries of the MoM matrix and it is the main advantage of the method.

4.4.2. TE Mode

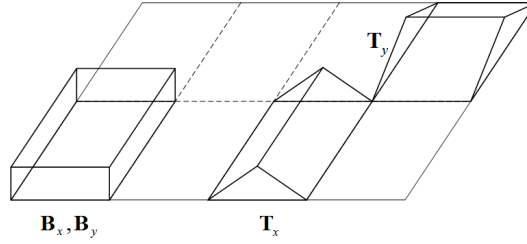


Figure 4.3: Basis and testing functions selected for the MoM application.

Contrary to *TM* mode incident field, *TE* excitation induces an electric current perpendicular to z -direction such as $\bar{J} = J_x(x, y)\hat{x} + J_y(x, y)\hat{y}$. Therefore in this case two polarization currents must be solved by MoM employing two EFIE's:

$$E_x^t(x, y) - E_x^s(x, y) = E_x^i(x, y), \quad (4.47)$$

where

$$E_x^s = -j\omega\mu_0 G * J_x + \frac{1}{j\omega\epsilon_0} \frac{\partial}{\partial x} \left(G * \frac{\partial}{\partial x} J_x \right) + \frac{1}{j\omega\epsilon_0} \frac{\partial}{\partial x} \left(G * \frac{\partial}{\partial y} J_y \right). \quad (4.48)$$

and

$$E_y^t(x, y) - E_y^s(x, y) = E_y^i(x, y), \quad (4.49)$$

where

$$E_y^s = -j\omega\mu_0 G * J_y + \frac{1}{j\omega\epsilon_0} \frac{\partial}{\partial y} \left(G * \frac{\partial}{\partial x} J_x \right) + \frac{1}{j\omega\epsilon_0} \frac{\partial}{\partial y} \left(G * \frac{\partial}{\partial y} J_y \right). \quad (4.50)$$

Note that, since the convolution of the induced polarization current $\nabla \cdot \bar{J}$ in (4.20) is not zero in this case, inner product operations contain differentiations that may result in singularities due to the choice of the basis and testing functions. Therefore there is an admissible set of functions for basis (testing) functions depending on the

testing (basis) function. Regarding TE mode, the strongest condition for the choice of the basis and testing functions for the convergence of the integrals comes from the term containing double derivative with respect to the same variable. For the assurance of the convergence, it was showed that [74], if the basis function is a piecewise continuous function, the testing function should be selected at least from a class of piecewise differentiable functions, or vice versa. Therefore unlike *TM* mode case Galerkin's MoM with pulse functions is not applicable.

Together with the convergence issue, the other important constraint of this study is finding a MoM approach that is capable of solving arbitrary shaped and electrically different structures and handling the changes in the geometry efficiently. Therefore a model is desired in which each discretization cell has different electrical properties. To achieve this, basis and testing functions should occupy the single discretization cell only. To satisfy this constraint together with the convergence issue, the pulse functions should be used for basis functions and in turn testing functions become rooftop as seen in Fig. 4.3. The reverse case is not applicable because if the triangular function occupying a single cell is chosen for the basis function, the polarization current will be forced to be zero at the edges of the cells, which does not match the physical form of the actual current density and in turn causes inaccurate results. For the same reason, Galerkin's MoM with rooftop functions is not applicable either.

According to these discussions, J_x and J_y are expressed in terms of basis functions as

$$J_x(x, y) = \sum_{m=1}^{N_x} \sum_{n=1}^{N_y} I_{xmn} B_m(x) B_n(y). \quad (4.51)$$

and

$$J_y(x, y) = \sum_{m=1}^{N_x} \sum_{n=1}^{N_y} I_{ymn} B_m(x) B_n(y). \quad (4.52)$$

where B_m and B_n are defined in (4.23) and (4.24), respectively and testing functions for J_x and J_y are chosen as rooftop functions

$$T_{xm'n'}(x, y) = \Lambda_{m'}(x) B_{n'}(y) \quad (4.53)$$

where

$$\Lambda_{xm'}(x) = \begin{cases} 1 - \frac{2|x-m'h_x|}{h_x}, & \text{if } (m' - \frac{1}{2})h_x \leq x \leq (m' + \frac{1}{2})h_x, \\ 0, & \text{otherwise.} \end{cases} \quad (4.54)$$

and

$$T_{ym'n'}(x, y) = B_{m'}(x)\Lambda_{n'}(y) \quad (4.55)$$

where

$$\Lambda_{yn'}(y) = \begin{cases} 1 - \frac{2|y-n'h_y|}{h_y}, & \text{if } (n' - \frac{1}{2})h_y \leq y \leq (n' + \frac{1}{2})h_y, \\ 0, & \text{otherwise.} \end{cases} \quad (4.56)$$

Note that, since the analyses of two EFIE's are same, we focus on the solution of the first EFIE in (4.47), for the sake of brevity. In addition E_x^s term in (4.48) is rewritten for further analysis as follows

$$E_x^s = \underbrace{-j\omega\mu_0 G * J_x}_{A_x} + \underbrace{\frac{1}{j\omega\epsilon_0} \frac{\partial}{\partial x} \left(G * \frac{\partial}{\partial x} J_x \right)}_{B_x} + \underbrace{\frac{1}{j\omega\epsilon_0} \frac{\partial}{\partial x} \left(G * \frac{\partial}{\partial y} J_y \right)}_{C_x} \quad (4.57)$$

where the derivations of A_x , B_x and C_x and the application of the testing procedure to these terms will be discussed separately. Before that, the algebraic equation need to be stated as

$$\langle T_{m'n'}, E_x^t \rangle - \langle T_{m'n'}, A_x \rangle - \langle T_{m'n'}, B_x \rangle - \langle T_{m'n'}, C_x \rangle = \langle T_{m'n'}, E_x^i \rangle. \quad (4.58)$$

Since $\langle T_{m'n'}, E_x^t \rangle$ and $\langle T_{m'n'}, E_x^i \rangle$ do not contain Green's function, they can be solved analytically as

$$\begin{aligned} \langle T_{m'n'}, E_x^t \rangle &= \sum_{m=1}^{N_x} \sum_{n=1}^{N_y} I_{xmn} \int_{(m'-\frac{1}{2})h_x}^{(m'+\frac{1}{2})h_x} \int_{(n'-\frac{1}{2})h_y}^{(n'+\frac{1}{2})h_y} \frac{T_{xm'n'}(x, y) B_m(x) B_n(y)}{jk_0 Y_0(\epsilon_r - 1)} dx dy \\ &= \sum_{m=1}^{N_x} \sum_{n=1}^{N_y} I_{xmn} \frac{h_x h_y}{2jk_0 Y_0(\epsilon_r - 1)} \delta_{m'm, n'n} \end{aligned} \quad (4.59)$$

and

$$\begin{aligned} \langle T_{m'n'}, E_x^i \rangle &= E_{ox} \int_{(m'-\frac{1}{2})h_x}^{(m'+\frac{1}{2})h_x} \Lambda_{m'}(x) e^{-jk_{x0}x} dx \int_{(n'-\frac{1}{2})h_y}^{(n'+\frac{1}{2})h_y} B_{n'}(y) e^{-jk_{y0}y} dy \\ &= E_{ox} h_x h_y e^{-j(k_{x0}m'h_x + k_{y0}n'h_y)} \text{sinc}^2(k_{x0}h_x/4) \text{sinc}(k_{y0}h_y/2), \end{aligned} \quad (4.60)$$

respectively.

Now we can derive A_x , B_x and C_x to construct E_x^s and convolve with the testing function. The procedure to derive A_x and $\langle T_{m'n'}, A_x \rangle$ is very similar to the term discussed in the previous section, since this term does not contain derivatives and J_x is directly convolved with the Green's function similar to J_z in TM mode:

$$A_x = \sum_{m=1}^{N_x} \sum_{n=1}^{N_y} -I_{xmn} j \omega \mu_0 \int_{(m-\frac{1}{2})h_x}^{(m+\frac{1}{2})h_x} \int_{(n-\frac{1}{2})h_y}^{(n+\frac{1}{2})h_y} B_m(x') B_n(y') G(x, y; x', y') dx' dy'. \quad (4.61)$$

where G is defined in (4.36). Substituting (4.36) into (4.61) and convolving with the testing function in (4.53) result in

$$\begin{aligned} \langle T_{xm'n'}, A_x \rangle = & -\frac{\omega \mu_0}{4} \sum_{m=1}^{N_x} \sum_{n=1}^{N_y} I_{xmn} \frac{1}{\pi} \int_{-\infty}^{+\infty} \frac{dk_x}{k_y} \int_{(m'-\frac{1}{2})h_x}^{(m'+\frac{1}{2})h_x} \int_{(m-\frac{1}{2})h_x}^{(m+\frac{1}{2})h_x} \Lambda_{m'}(x) B_m(x') e^{-jk_x(x-x')} dx dx' \\ & \times \int_{(n'-\frac{1}{2})h_y}^{(n'+\frac{1}{2})h_y} \int_{(n-\frac{1}{2})h_y}^{(n+\frac{1}{2})h_y} B_{n'}(y) B_n(y') e^{-jk_y|y-y'|} dy dy' \end{aligned} \quad (4.62)$$

which yields two expressions:

1. For $|n' - n| \geq 1$:

$$\begin{aligned} \langle T_{xm'n'}, A_x \rangle = & -\frac{\omega \mu_0}{8} h_x^2 h_y^2 \sum_{m=1}^{N_x} \sum_{n=1}^{N_y} I_{xmn} \frac{1}{\pi} \int_{-\infty}^{+\infty} \frac{dk_x}{k_y} e^{-jk_x(m'-m)h_x} e^{-jk_y|n'-n|h_y} \\ & \times \text{sinc}^2(k_x h_x / 4) \text{sinc}(k_x h_x / 2) \text{sinc}^2(k_y h_y / 2) \end{aligned} \quad (4.63)$$

2. For $n' = n$:

$$\begin{aligned} \langle T_{xm'n'}, A_x \rangle = & \frac{\omega \mu_0}{8} h_x^2 h_y^2 \sum_{m=1}^{N_x} \sum_{n=1}^{N_y} I_{xmn} \frac{1}{\pi} \int_{-\infty}^{+\infty} \frac{dk_x}{k_y} e^{-jk_x(m'-m)h_x} \text{sinc}^2(k_x h_x / 4) \\ & \times \text{sinc}(k_x h_x / 2) \frac{2}{jk_y h_y} \left[1 - e^{-jk_y h_y / 2} \text{sinc}(k_y h_y / 2) \right] \end{aligned} \quad (4.64)$$

The second term B_x of E_x^s contains differentiations with respect to x , therefore the derivative of the basis function come into prominence for this term. We start with

expressing J_x with basis functions and write B_x as follows

$$B_x = \sum_{m=1}^{N_x} \sum_{n=1}^{N_y} I_{xmn} \frac{1}{j\omega\epsilon_0} \frac{\partial}{\partial x} \left(G * \frac{\partial}{\partial x} B_m(x) B_n(y) \right) \quad (4.65)$$

Since B_m is a pulse function, its derivative results in two impulse functions defined at the edges of the corresponding subsection:

$$\frac{\partial}{\partial x} B_m(x) = \delta \left(x - \left(m - \frac{1}{2}\right)h_x \right) - \delta \left(x + \left(m - \frac{1}{2}\right)h_x \right). \quad (4.66)$$

Note that the convolution of the Green's function with an impulse function is equal to the evaluation of the Green's function at the point where impulse function is defined. Therefore when we substitute the Green's function and convolve with the impulse functions, B_x becomes

$$\begin{aligned} B_x &= -\frac{1}{4\omega\epsilon_0} \sum_{m=1}^{N_x} \sum_{n=1}^{N_y} I_{xmn} \frac{1}{\pi} \int_{-\infty}^{+\infty} \frac{dk_x}{k_y} \frac{\partial}{\partial x} e^{-jk_x x} \left[e^{jk_x(m-\frac{1}{2})h_x} - e^{jk_x(m+\frac{1}{2})h_x} \right] \\ &\quad \times \int_{(n-\frac{1}{2})h_y}^{(n+\frac{1}{2})h_y} e^{-jk_y|y-y'|} dy' \\ &= -\frac{h_x}{4\omega\epsilon_0} \sum_{m=1}^{N_x} \sum_{n=1}^{N_y} I_{xmn} \frac{1}{\pi} \int_{-\infty}^{+\infty} \frac{dk_x}{k_y} k_x^2 e^{-jk_x(x-mh_x)} \text{sinc}(k_x h_x/2) \\ &\quad \times \int_{(n-\frac{1}{2})h_y}^{(n+\frac{1}{2})h_y} e^{-jk_y|y-y'|} dy' \quad (4.67) \end{aligned}$$

After the application of the testing procedure and evaluation of the analytically solvable integrals, $\langle T_{xm'n'}, B_x \rangle$ can be calculated as

1. For $|n' - n| \geq 1$:

$$\begin{aligned} \langle T_{xm'n'}, B_x \rangle &= \frac{\omega\mu_0}{8} h_x^2 h_y^2 \sum_{m=1}^{N_x} \sum_{n=1}^{N_y} I_{xmn} \frac{1}{\pi} \int_{-\infty}^{+\infty} \frac{dk_x}{k_y} k_x^2 e^{-jk_x(m'-m)h_x} e^{-jk_y|n'-n|h_y} \\ &\quad \times \text{sinc}^2(k_x h_x/4) \text{sinc}(k_x h_x/2) \text{sinc}^2(k_y h_y/2) \quad (4.68) \end{aligned}$$

2. For $n' = n$:

$$\begin{aligned} \langle T_{xm'n'}, B_x \rangle &= \frac{\omega\mu_0}{8} h_x^2 h_y^2 \sum_{m=1}^{N_x} \sum_{n=1}^{N_y} I_{xmn} \frac{1}{\pi} \int_{-\infty}^{+\infty} \frac{dk_x}{k_y} k_x^2 e^{-jk_x(m'-m)h_x} \text{sinc}^2(k_x h_x/4) \\ &\quad \times \text{sinc}(k_x h_x/2) \frac{2}{jk_y h_y} \left[1 - e^{-jk_y h_y/2} \text{sinc}(k_y h_y/2) \right] \end{aligned} \quad (4.69)$$

Finally, third term C_x of E_x^s is analyzed with the similar manner. Similar to B_x , C_x contains differentiations to be evaluate but depending on both x and y variables in this case:

$$C_x = \sum_{m=1}^{N_x} \sum_{n=1}^{N_y} I_{ymn} \frac{1}{j\omega\epsilon_0} \frac{\partial}{\partial x} \left(G * B_m(x) \frac{\partial}{\partial y} B_n(y) \right) \quad (4.70)$$

Since B_n is a pulse function, its derivative becomes:

$$\frac{\partial}{\partial y} B_n(y) = \delta \left(y - (n - \frac{1}{2})h_y \right) - \delta \left(y + (n - \frac{1}{2})h_y \right). \quad (4.71)$$

Substituting the Green's function and convolving with the impulse function yields

$$\begin{aligned} C_x &= -\frac{1}{4\omega\epsilon_0} \sum_{m=1}^{N_x} \sum_{n=1}^{N_y} I_{ymn} \frac{1}{\pi} \int_{-\infty}^{+\infty} \frac{dk_x}{k_y} \frac{\partial}{\partial x} e^{-jk_x x} \int_{(m-\frac{1}{2})h_x}^{(m+\frac{1}{2})h_x} e^{-jk_x x'} dx' \\ &\quad \times \left[e^{-jk_y |y - (n-\frac{1}{2})h_y|} - e^{-jk_y |y - (n+\frac{1}{2})h_y|} \right] \\ &= -\frac{h_x}{4\omega\epsilon_0} \sum_{m=1}^{N_x} \sum_{n=1}^{N_y} I_{ymn} \frac{1}{\pi} \int_{-\infty}^{+\infty} \frac{dk_x}{k_y} (-jk_x) e^{-jk_x(x-mh_x)} \text{sinc}(k_x h_x/2) \\ &\quad \times \left[e^{-jk_y |y - (n-\frac{1}{2})h_y|} - e^{-jk_y |y - (n+\frac{1}{2})h_y|} \right] \end{aligned} \quad (4.72)$$

Finally, the testing procedure yields three different expressions for C_x :

1. For $(n' - n) \geq 1$:

$$\begin{aligned} \langle T_{xm'n'}, C_x \rangle &= \frac{\omega\mu_0}{8} h_x^2 h_y^2 \sum_{m=1}^{N_x} \sum_{n=1}^{N_y} I_{ymn} \frac{1}{\pi} \int_{-\infty}^{+\infty} \frac{dk_x}{k_y} e^{-jk_x(m'-m)h_x} e^{-jk_y(n'-n)h_y} \\ &\quad \times (-k_x k_y) \text{sinc}^2(k_x h_x/4) \text{sinc}(k_x h_x/2) \text{sinc}^2(k_y h_y/2) \end{aligned} \quad (4.73)$$

2. For $(n - n') \geq 1$:

$$\begin{aligned} \langle T_{xm'n'}, C_x \rangle &= \frac{\omega\mu_0}{8} h_x^2 h_y^2 \sum_{m=1}^{N_x} \sum_{n=1}^{N_y} I_{ymn} \frac{1}{\pi} \int_{-\infty}^{+\infty} \frac{dk_x}{k_y} e^{-jk_x(m'-m)h_x} e^{-jk_y(n-n')h_y} \\ &\quad \times k_x k_y \text{sinc}^2(k_x h_x/4) \text{sinc}(k_x h_x/2) \text{sinc}^2(k_y h_y/2) \end{aligned} \quad (4.74)$$

3. For $n' = n$:

$$\langle T_{xm'n'}, C_x \rangle = 0 \quad (4.75)$$

Finally first EFIE for TE excitation is obtained by evaluating each term in (4.58). Note that the derivation of the second EFIE can be performed in the same manner. Together with the second EFIE, the algebraic equation to solve J_x and J_y can be written in matrix form:

$$\begin{bmatrix} \mathbf{Z}_{11} & \mathbf{Z}_{12} \\ \mathbf{Z}_{21} & \mathbf{Z}_{22} \end{bmatrix} \begin{bmatrix} \mathbf{I}_x \\ \mathbf{I}_y \end{bmatrix} = \begin{bmatrix} \mathbf{R}_1 \\ \mathbf{R}_2 \end{bmatrix} \quad (4.76)$$

where $\mathbf{R}_1 = [\langle T_{x11}, E_x^i \rangle \dots \langle T_{xN_x N_y}, E_x^i \rangle]^T$ is the excitation vector for the first EFIE and \mathbf{Z}_{11} can be expressed according to the derivations performed so far:

- \mathbf{Z}_{11}

1. For $|n' - n| \geq 1$:

$$\begin{aligned} Z_{11m'n',mn} &= \frac{\omega\mu_0}{8} h_x^2 h_y^2 \frac{1}{\pi} \int_{-\infty}^{+\infty} \frac{dk_x}{k_y} e^{-jk_x(m'-m)h_x} e^{-jk_y|n'-n|h_y} \left(1 - \frac{k_x^2}{k_0^2} \right) \\ &\quad \times \text{sinc}^2(k_x h_x/4) \text{sinc}(k_x h_x/2) \text{sinc}^2(k_y h_y/2) \\ &= \frac{\omega\mu_0}{8} h_x^2 h_y^2 \frac{1}{\pi} \int_{-\infty}^{+\infty} \frac{dk_x}{k_y} e^{-jk_x(m'-m)h_x} e^{-jk_y|n'-n|h_y} \sum_t a_t e^{-\alpha_t k_y} \\ &= \frac{\omega\mu_0}{8} h_x^2 h_y^2 \sum_t a_t H_0^{(2)}(k\rho_t) \end{aligned} \quad (4.77)$$

where $\rho_t = \sqrt{((m' - m)h_x)^2 + (|n' - n|h_y - j\alpha_t)^2}$;

2. For $n' = n$:

$$\begin{aligned}
 Z_{11m'n',mn} &= \frac{h_x h_y}{jk_0 Y_0(\epsilon_r - 1)} \delta_{m'm} + \frac{\omega \mu_0}{8} h_x^2 h_y^2 \frac{1}{\pi} \int_{-\infty}^{+\infty} \frac{dk_x}{k_y} e^{-jk_x(m'-m)h_x} \left(1 - \frac{k_x^2}{k_0^2}\right) \\
 &\quad \times \text{sinc}^2(k_x h_x/4) \text{sinc}(k_x h_x/2) \frac{2}{jk_y h_y} (1 - e^{-jk_y h_y/2} \text{sinc}(k_y h_y/2)) \\
 &= \frac{h_x h_y}{jk_0 Y_0(\epsilon_r - 1)} \delta_{m'm} + \frac{\omega \mu_0}{8} h_x^2 h_y^2 \frac{1}{\pi} \int_{-\infty}^{+\infty} \frac{dk_x}{k_y} e^{-jk_x(m'-m)h_x} \sum_t a_t e^{-\alpha_t k_y} \\
 &= \frac{h_x h_y}{jk_0 Y_0(\epsilon_r - 1)} \delta_{m'm} + \frac{\omega \mu_0}{8} h_x^2 h_y^2 \sum_t a_t H_0^{(2)}(k \rho_t) \tag{4.78}
 \end{aligned}$$

where $\rho_t = \sqrt{((m' - m)h_x)^2 + (-j\alpha_t)^2}$.

It's important to note that, similar to the case of TM excitation, for the evaluation of the integrals which are over infinite k_x domain, exponential approximation allows expressing the integrand (apart from $1/k_y$ and exponential terms) as a sum of complex exponentials. Therefore the integral can be evaluated as a sum of Hankel functions with the appropriate arguments. This is also valid for MoM matrix \mathbf{Z}_{12} :

• \mathbf{Z}_{12}

1. For $(n' - n) \geq 1$:

$$\begin{aligned}
 Z_{12m'n',mn} &= \frac{h_x^2 h_y^2}{8\omega\epsilon_0} \frac{1}{\pi} \int_{-\infty}^{+\infty} \frac{dk_x}{k_y} e^{-jk_x(m'-m)h_x} e^{-jk_y(n'-n)h_y} \\
 &\quad \times (-k_x k_y) \text{sinc}^2(k_x h_x/4) \text{sinc}(k_x h_x/2) \text{sinc}^2(k_y h_y/2) \\
 &= \frac{h_x^2 h_y^2}{8\omega\epsilon_0} \frac{\partial}{\partial x} \frac{1}{\pi} \int_{-\infty}^{+\infty} \frac{dk_x}{k_y} e^{-jk_x(m'-m)h_x} e^{-jk_y(n'-n)h_y} \\
 &\quad \times (-jk_y) \text{sinc}^2(k_x h_x/4) \text{sinc}(k_x h_x/2) \text{sinc}^2(k_y h_y/2) \\
 &= \frac{h_x^2 h_y^2}{8\omega\epsilon_0} \frac{\partial}{\partial x} \frac{1}{\pi} \int_{-\infty}^{+\infty} \frac{dk_x}{k_y} e^{-jk_x(m'-m)h_x} e^{-jk_y(n'-n)h_y} \sum_t a_t e^{-\alpha_t k_y} \\
 &= \frac{h_x^2 h_y^2}{8\omega\epsilon_0} \frac{\partial}{\partial x} \sum_t a_t H_0^{(2)}(k\rho_t) \\
 &= \frac{h_x^2 h_y^2}{8\omega\epsilon_0} \sum_t \frac{-a_t k_0}{\rho_t} [(n' - n)h_y - j\alpha_t] H_1^{(2)}(k\rho_t) \tag{4.79}
 \end{aligned}$$

where $\rho_t = \sqrt{((m' - m)h_x)^2 + ((n' - n)h_y - j\alpha_t)^2}$;

2. For $(n - n') \geq 1$:

$$\begin{aligned}
 Z_{12m'n',mn} &= \frac{h_x^2 h_y^2}{8\omega\epsilon_0} \frac{1}{\pi} \int_{-\infty}^{+\infty} \frac{dk_x}{k_y} e^{-jk_x(m'-m)h_x} e^{-jk_y(n-n')h_y} \\
 &\quad \times (k_x k_y) \text{sinc}^2(k_x h_x/4) \text{sinc}(k_x h_x/2) \text{sinc}^2(k_y h_y/2) \\
 &= \frac{h_x^2 h_y^2}{8\omega\epsilon_0} \frac{\partial}{\partial x} \frac{1}{\pi} \int_{-\infty}^{+\infty} \frac{dk_x}{k_y} e^{-jk_x(m'-m)h_x} e^{-jk_y(n-n')h_y} \\
 &\quad \times (jk_y) \text{sinc}^2(k_x h_x/4) \text{sinc}(k_x h_x/2) \text{sinc}^2(k_y h_y/2) \\
 &= \frac{h_x^2 h_y^2}{8\omega\epsilon_0} \frac{\partial}{\partial x} \frac{1}{\pi} \int_{-\infty}^{+\infty} \frac{dk_x}{k_y} e^{-jk_x(m'-m)h_x} e^{-jk_y(n-n')h_y} \sum_t a_t e^{-\alpha_t k_y} \\
 &= \frac{h_x^2 h_y^2}{8\omega\epsilon_0} \frac{\partial}{\partial x} \sum_t a_t H_0^{(2)}(k\rho_t) \\
 &= \frac{h_x^2 h_y^2}{8\omega\epsilon_0} \sum_t \frac{-a_t k_0}{\rho_t} [(n - n')h_y - j\alpha_t] H_1^{(2)}(k\rho_t) \tag{4.80}
 \end{aligned}$$

$$\text{where } \rho_t = \sqrt{((m' - m)h_x)^2 + ((n - n')h_y - j\alpha_t)^2}.$$

3. For $n' = n$: $Z_{12m'n',mn} = 0$

It is important to point out that the entries of \mathbf{Z}_{11} and \mathbf{Z}_{12} are in closed forms where there are only two different closed form expressions for all matrix entries similar to the case in TM excitation.

Similar expressions for \mathbf{Z}_{21} and \mathbf{Z}_{22} and the details of the second EFIE are also included in the Appendix.

4.4.3. Field Calculation

In the previous sections, the MoM application for the solution of the polarization current induced inside the material in free space due to the excitation of a plane wave has been provided in detail. Using the induced polarization current, the electric field needs to be found at any point of interest. The most straightforward approach is to

employ (4.13) that requires the convolution of the Green's function and the polarization current. For TM mode excitation, it is applicable because of the fact that there is no operation that may result in singularities, yet the new integration containing the Green's function need to be evaluated. On the other hand in TE mode excitation, (4.13) requires the gradient of the convolution of the Green's function and the divergence of the polarization current. This operation contains second order differentials and this results in singularities due to the basis functions that were selected as pulse functions. Note that in MoM application, the testing function were selected particularly to eliminate the singularities but there is no testing operation in this case. Therefore finding fields by evaluating (4.13) is not possible for TE mode problem.

As an alternative and more efficient approach, the fields inside and outside of the material can be treated separately. As derived in (4.19), the total field inside the material is proportional to the induced polarization current therefore it can be obtained directly from (4.19). Note that since the incident field is known, the scattered field can also be obtained directly by subtracting the incident field from the total electric field.

On the other hand, the electric field outside of the material needs to be a different approach. In the MoM application, the basis functions can be viewed as sources acting independently and the electric field on a region specified by the testing function is the sum of the contributions of the basis functions where the testing operation averages their total contribution according to the form of the testing function. By using this point of view, the scattered field can be obtained at a cell located outside of the material by averaging the overall contribution of the basis functions inside the material with the testing function used before. This is achieved by employing simply some part of the formulations in MoM. Considering the case for the TM excitation the testing procedure for the scattering field can be rewritten as

$$\langle T_{m'n'}, E_z^s \rangle = - \sum_{m=1}^{N_x} \sum_{n=1}^{N_y} I_{zmn} j \omega \mu_0 \left\langle T_{m'n'}, (G(x, y) * B_m(x) B_n(y)) \right\rangle, \quad (4.81)$$

where the indices $m'n'$ representing the testing region correspond to an area in free

space in this case. Considering the discussion above; the electric field, the location of which is specified by the indices $m'n'$, is the sum of the contributions of the basis functions with coefficients of I_{zmn} which have been found in the previous section. Since the region indicated by $m'n'$ is sufficiently small (typically smaller than wavelength/10), (4.81) is approximately equal to the scattering field itself and can be written in matrix form as

$$\mathbf{E}_z^s \cong \mathbf{Z}_f \mathbf{I}_z, \quad (4.82)$$

where \mathbf{I}_z is the coefficient vector in (4.44) which has already been found by MoM and \mathbf{E}_z^s is the field vector consisting of the field values for desired regions defined by the pairs of $m'n'$. \mathbf{Z}_f is the field matrix whose entries have already been evaluated in (4.45) and (4.46) together with other terms related to EFIE. In order to be more clear, \mathbf{Z}_f is presented below:

- \mathbf{Z}_f

1. For $|n' - n| \geq 1$:

$$\begin{aligned} Z_{fm'n',mn} &= \frac{-\omega\mu_0}{4} h_x^2 h_y^2 \frac{1}{\pi} \int_{-\infty}^{+\infty} \frac{dk_x}{k_y} e^{-jk_x(m'-m)h_x} e^{-jk_y|n'-n|h_y} \\ &\quad \times \text{sinc}^2(k_x h_x/2) \text{sinc}^2(k_y h_y/2) \\ &= \frac{-\omega\mu_0}{4} h_x^2 h_y^2 \frac{1}{\pi} \int_{-\infty}^{+\infty} \frac{dk_x}{k_y} e^{-jk_x(m'-m)h_x} e^{-jk_y|n'-n|h_y} \sum_t a_t e^{-\alpha_t k_y} \\ &= \frac{-\omega\mu_0}{4} h_x^2 h_y^2 \sum_t a_t H_0^{(2)}(k\rho_t) \end{aligned} \quad (4.83)$$

where $\rho_t = \sqrt{((m' - m)h_x)^2 + (|n' - n|h_y - j\alpha_t)^2}$;

2. For $n' = n$:

$$\begin{aligned}
 Z_{fm'n',mn} &= \frac{-\omega\mu_0}{4} h_x^2 h_y^2 \frac{1}{\pi} \int_{-\infty}^{+\infty} \frac{dk_x}{k_y} e^{-jk_x(m'-m)h_x} \\
 &\quad \times \text{sinc}^2(k_x h_x/2) \frac{2}{jk_y h_y} \left[1 - e^{-jk_y h_y/2} \text{sinc}(k_y h_y/2) \right] \\
 &= \frac{-\omega\mu_0}{4} h_x^2 h_y^2 \frac{1}{\pi} \int_{-\infty}^{+\infty} \frac{dk_x}{k_y} e^{-jk_x(m'-m)h_x} \sum_t a_t e^{-\alpha_t k_y} \\
 &= \frac{-\omega\mu_0}{4} h_x^2 h_y^2 \sum_t a_t H_0^{(2)}(k\rho_t)
 \end{aligned} \tag{4.84}$$

$$\text{where } \rho_t = \sqrt{((m' - m)h_x)^2 + (-j\alpha_t)^2}.$$

Note that (4.83) is identical to the negative of (4.45) and (4.84) is written from (4.46) without its first term.

The same approach is also applicable to TE mode, where the scattered field can be represented in the matrix form:

$$\begin{bmatrix} \mathbf{E}_x^s \\ \mathbf{E}_y^s \end{bmatrix} \cong \begin{bmatrix} \mathbf{Z}_{f11} & \mathbf{Z}_{f12} \\ \mathbf{Z}_{f21} & \mathbf{Z}_{f22} \end{bmatrix} \begin{bmatrix} \mathbf{I}_x \\ \mathbf{I}_y \end{bmatrix} \tag{4.85}$$

where

- \mathbf{Z}_{f11}

1. For $|n' - n| \geq 1$:

$$Z_{f11m'n',mn} = -Z_{11m'n',mn} \tag{4.86}$$

2. For $n' = n$:

$$\begin{aligned}
 Z_{11m'n',mn} &= \frac{-\omega\mu_0}{8} h_x^2 h_y^2 \frac{1}{\pi} \int_{-\infty}^{+\infty} \frac{dk_x}{k_y} e^{-jk_x(m'-m)h_x} \left(1 - \frac{k_x^2}{k_0^2} \right) \\
 &\quad \times \text{sinc}^2(k_x h_x / 4) \text{sinc}(k_x h_x / 2) \frac{2}{jk_y h_y} \left[1 - e^{-jk_y h_y / 2} \text{sinc}(k_y h_y / 2) \right] \\
 &= \frac{-\omega\mu_0}{8} h_x^2 h_y^2 \frac{1}{\pi} \int_{-\infty}^{+\infty} \frac{dk_x}{k_y} e^{-jk_x(m'-m)h_x} \sum_t a_t e^{-\alpha_t k_y} \\
 &= \frac{-\omega\mu_0}{8} h_x^2 h_y^2 \sum_t a_t H_0^{(2)}(k\rho_t) \tag{4.87}
 \end{aligned}$$

where $\rho_t = \sqrt{((m' - m)h_x)^2 + (-j\alpha_t)^2}$.

- $\mathbf{Z}_{f12} = -\mathbf{Z}_{12}$

\mathbf{Z}_{f21} and \mathbf{Z}_{f22} are presented in Appendix.

To sum up, the electric field inside the material is found directly from the polarization currents and the electric field outside is found by using the idea of the MoM application. Unlike direct evaluation of the scattering field, this approach works for both excitation modes and in this manner, no additional integral evaluation is needed, i.e. the fields are evaluated by employing the same formulation and exponential approximation proposed for MoM application.

4.5. Numerical Examples and Discussions

In this section some numerical examples are provided to assess and validate the performance of the proposed MoM algorithm. For validation, the fields found by the proposed method developed for TM and TE propagation modes are compared to the ones obtained by the FEM-based commercial simulation tool, called *Comsol Multiphysics* by Comsol Inc. It is important to note that for TM mode the system is excited by a plane wave the input of which is the electric field with amplitude equal to 1 and for TE mode excitation the input of the plane wave is the magnetic field with

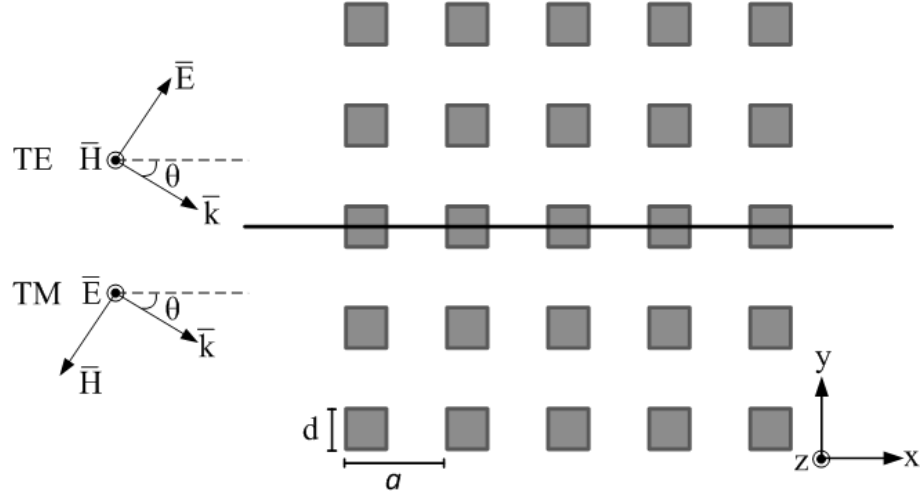


Figure 4.4: The finite PhC consisting of 25 square lattice of dielectric columns with relative permittivity $\epsilon_r = 8$, the lattice constant $a = 400nm$ and the width of a dielectric column $d = 120nm$. The PhC is excited by the plane waves in TM and TE mode and the resulting fields are calculated for the cross-section shown as a line.

unity amplitude this time. This difference has been made in order to be consistent with the inputs used in *Comsol Multiphysics* and valid for all examples presented in this work.

As the first example, consider a finite PhC consisting of 25 square lattice of dielectric columns with relative permittivity $\epsilon_r = 8$ where the width of each dielectric column and the lattice constant of the PhC are $d = 120nm$ and $a = 400nm$, respectively, as shown in Fig. 4.4. The proposed MoM approach for TM mode is employed to obtain the field E_z and the fields E_x and E_y are found for TE mode at the operating frequency 500 THz. The fields are calculated for the cross-section demonstrated with a line crossing the PhC in Fig. 4.4. For the case in which the angle of incidence is normal, i. e. $\theta = 0$, the electric field E_z resulting from TM mode excitation is demonstrated in Fig. 4.5 together with the result obtained by the Comsol simulation. Fig. 4.5 shows that the PhC prevent most of the field to propagate through it. In the TE excitation case, the fields E_y and E_x are shown in 4.6(a) and 4.6(b), respectively. Note that the amplitude of E_y is quite higher than E_x 's amplitude. It is expected because the PhC is excited with a plane wave in normal incidence meaning that only

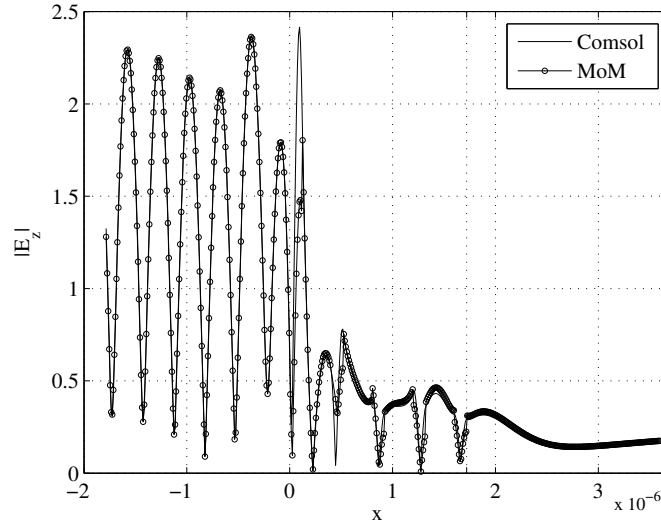
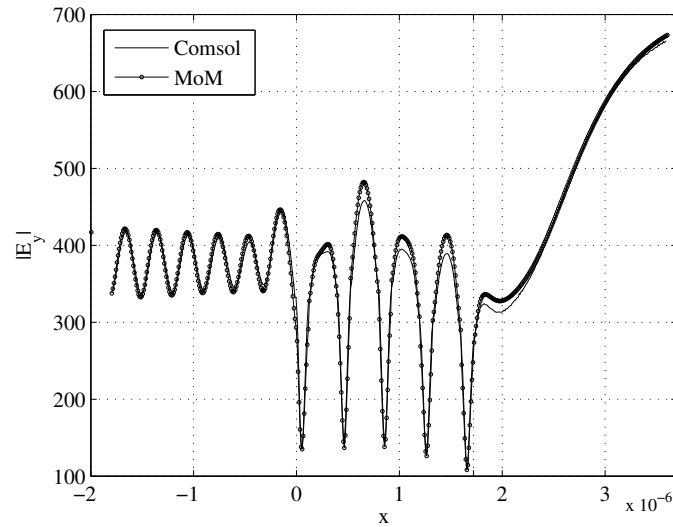


Figure 4.5: Magnitude of the field in z -direction due to the normal incident TM mode plane wave at 500 THz. The field is calculated over the finite photonic crystal shown in Fig. 4.4. The PhC covers the region from 0 to $1.72 \times 10^{-6}m$, which is demonstrated as an additional grid on x .

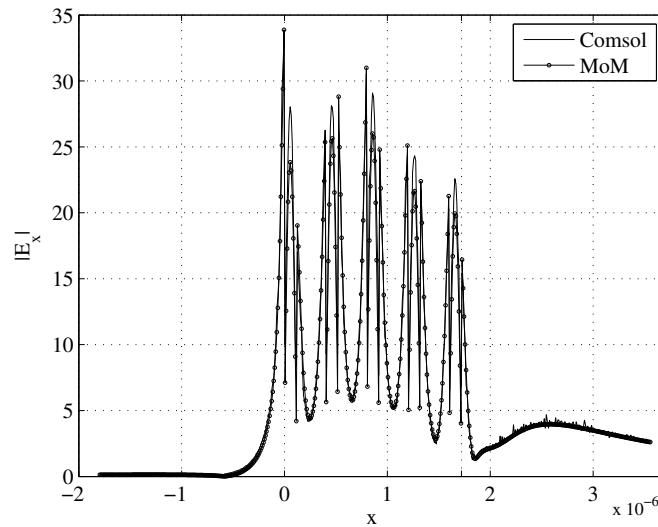
y component of the incident field exists. Therefore the field E_x is formed due to the interaction of the incident field in y -direction with the edges of the square columns of the PhC only, resulting in a noisy behavior. On the other hand, the results obtained by the MoM and Comsol agree quite well as seen from the field plots.

As the second example, the characterization of the same geometry is performed under the excitation of an oblique incidence where $\theta = 15^\circ$ at 500 THz. The field E_z resulting from TM mode excitation is demonstrated in Fig. 4.7 and the TE mode fields E_y and E_x are shown in 4.8(a) and 4.8(b), respectively, with the result of Comsol simulation. Where the behavior of the fields E_z and E_y are similar to the one in the normal incidence case, the field E_x behaves quite differently due to the fact that an incident field in x -direction exists in the oblique excitation and increases the contribution of the scattering in this direction.

As another example, the proposed MoM approach is applied to a finite defected PhC. The structure is obtained by removing the dielectric column at the center of the



(a)



(b)

Figure 4.6: Magnitude of the fields in *a*) *y*-direction and *b*) *x*-direction due to the normal incident TE mode plane wave at 500 THz. The field is calculated over the finite photonic crystal shown in Fig. 4.4. The PhC covers the region from 0 to $1.72 \times 10^{-6}m$, which is demonstrated as an additional grid on *x*.

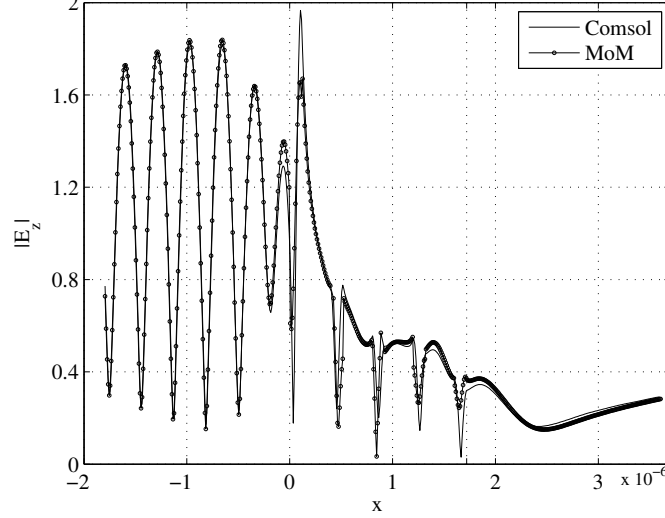
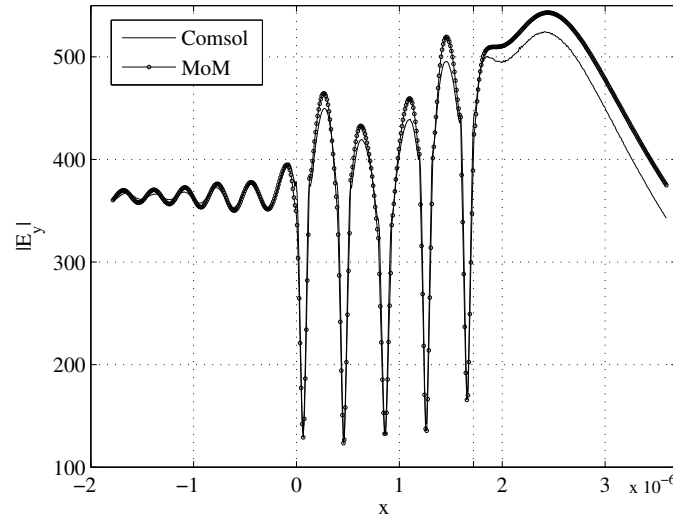


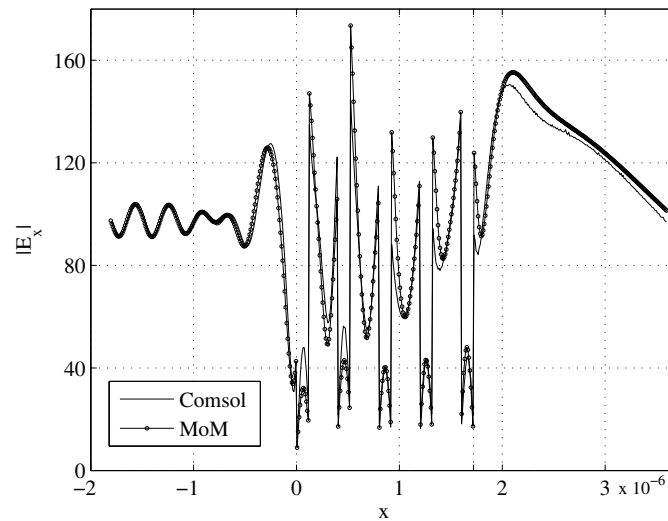
Figure 4.7: Magnitude of the field in z -direction due to the oblique incident TM mode plane wave at 500 THz with $\theta = 15$. The field is calculated over the finite photonic crystal shown in Fig. 4.4. The PhC covers the region from 0 to $1.72 \times 10^{-6}m$, which is demonstrated as an additional grid on x .

finite PhC discussed in the previous examples as shown in 4.9. The characterization of the geometry is performed under the excitation of normal incidence at 500 THz. The field E_z resulting from TM mode excitation is demonstrated in Fig. 4.10 with the result of Comsol simulation. Similarly, the TE mode fields E_y and E_x are shown in 4.11(a) and 4.11(b), respectively. When the fields of PhC's with and without defect (the first example of this section) are compared, it is observed that while E_z and E_y have four peaks corresponding to free-space regions inside the PhC without defect (Fig. 4.5 and 4.6(a)), the second and third peaks merge inside the PhC with defect (Fig. 4.10 and 4.11(a)). Similarly, while E_x has five peaks which correspond to the dielectric columns inside the PhC without defect (Fig. 4.6(b)), the central peak corresponding to the removed column disappears inside the defected PhC (Fig. 4.11(b)), as expected.

In order to validate that the proposed method is also suitable to analyze the metallic structures, the geometry shown in Fig. 4.12 is studied as another example.



(a)



(b)

Figure 4.8: Magnitude of the fields in *a*) *y*-direction and *b*) *x*-direction due to the oblique incident TE mode plane wave at 500 THz with $\theta = 15$. The field is calculated over the finite photonic crystal shown in Fig. 4.4. The PhC covers the region from 0 to $1.72 \times 10^{-6}m$, which is demonstrated as an additional grid on *x*.

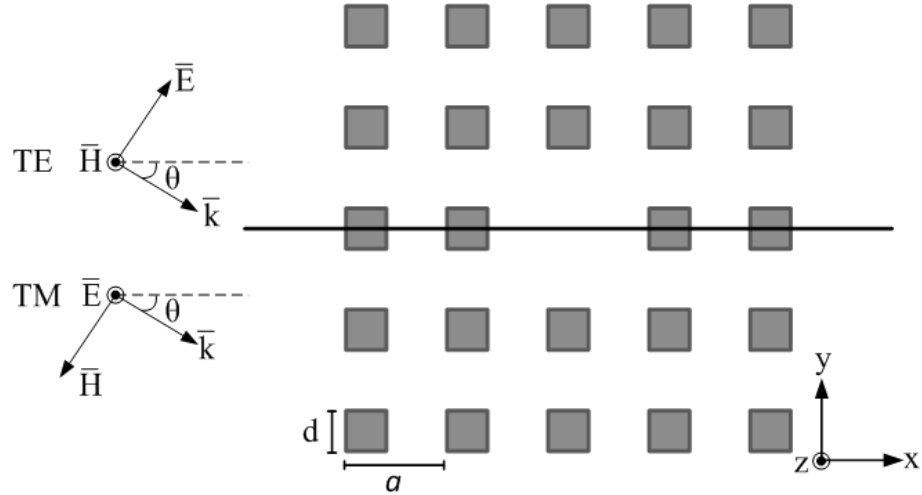


Figure 4.9: The finite PhC with defect consisting of 24 square lattice of dielectric columns with relative permittivity $\epsilon_r = 8$, the lattice constant $a = 400nm$ and the width of a dielectric column $d = 120nm$. The defect is introduced by removing the central dielectric column. The PhC is excited by the plane waves in TM and TE mode and the resulting fields are calculated for the cross-section shown as a line.

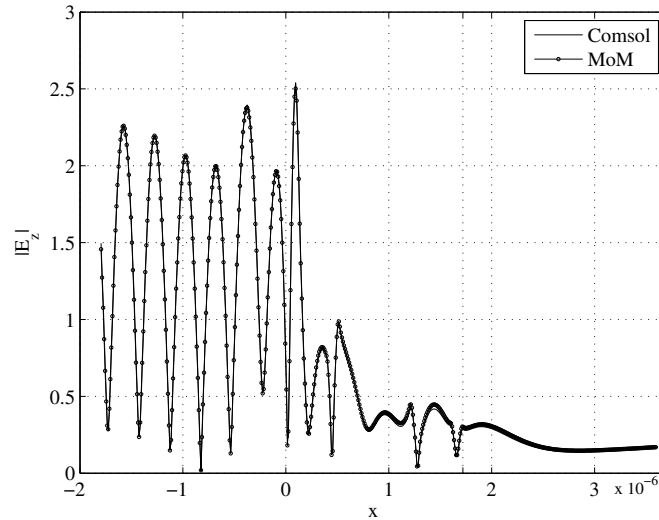
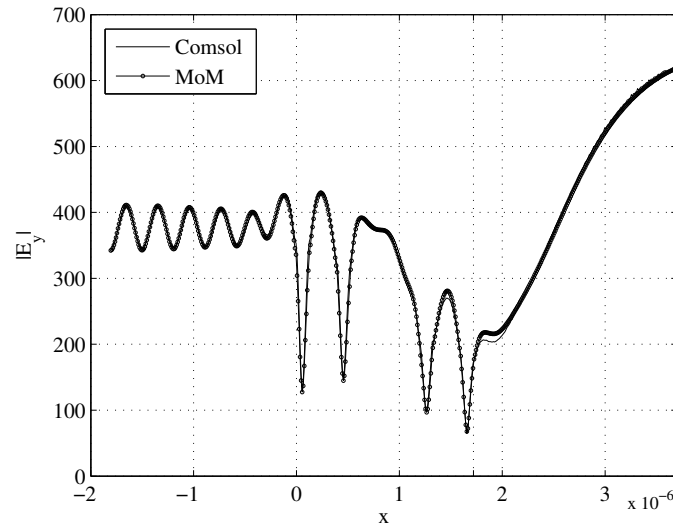
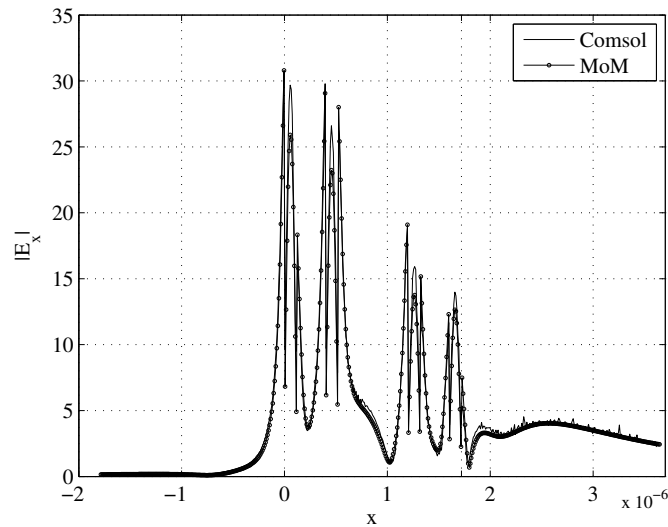


Figure 4.10: Magnitude of the field in z-direction due to the normal incident TM mode plane wave at 500 THz. The field is calculated over the finite photonic crystal with defect shown in Fig. 4.9. The PhC covers the region from 0 to $1.72 \times 10^{-6}m$, which is demonstrated as an additional grid on x .



(a)



(b)

Figure 4.11: Magnitude of the fields in *a*) *y*-direction and *b*) *x*-direction due to the normal incident TE mode plane wave at 500 THz. The field is calculated over the finite photonic crystal with defect shown in Fig. 4.9. The PhC covers the region from 0 to $1.72 \times 10^{-6}m$, which is demonstrated as an additional grid on *x*.

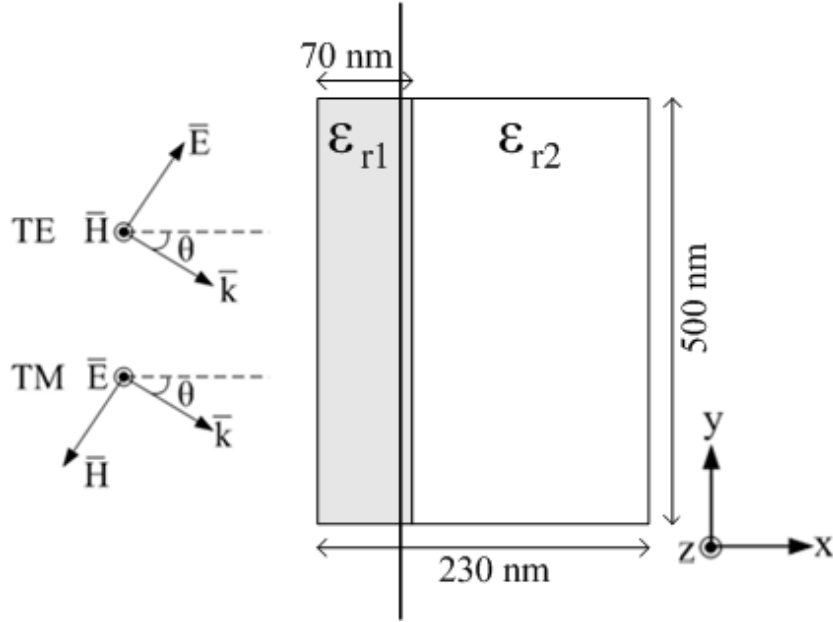


Figure 4.12: Dielectric and metallic structure in free space with the relative permittivities $\epsilon_{r1} = 4$ and $\epsilon_{r2}(Ag) = -15.91j - j0.43$ at 500 THz, respectively. The system is excited by the plane waves in TM and TE mode and the resulting fields are calculated for the cross-section shown as a line.

The structure in free space is composed of dielectric and metallic materials with the relative permittivities $\epsilon_{r1} = 4$ and $\epsilon_{r2}(Ag) = -15.91j - j0.43$ at 500 THz, respectively. The incident field is a plane wave impinging normally on the system from left and the fields are obtained along the interval demonstrated as a line of cross-section in Fig. 4.12. The field E_z resulting from TM mode excitation is demonstrated in Fig. 4.13 compared to the field obtained via Comsol. Similarly, the TE mode fields E_x and E_y are shown in 4.14(a) and 4.14(b), respectively. For TE polarization, a surface plasmon polariton (SPP) resonance is observed concentrated on the metallic scatterer where no such behavior is observed for TM polarization. It is expected because of the fact an electric field normal to the boundary of the metal and dielectric interface can not excite the surface plasmon in the structure due to the boundary conditions.

For the analysis of another metallic structure, consider a finite metallic structure with a single nano-slit in free space shown in Fig. 4.15. The relative permittivity of the metal is $\epsilon_r = -16.19j - j1.05$ and the width of the slit is 80 nm. The incident

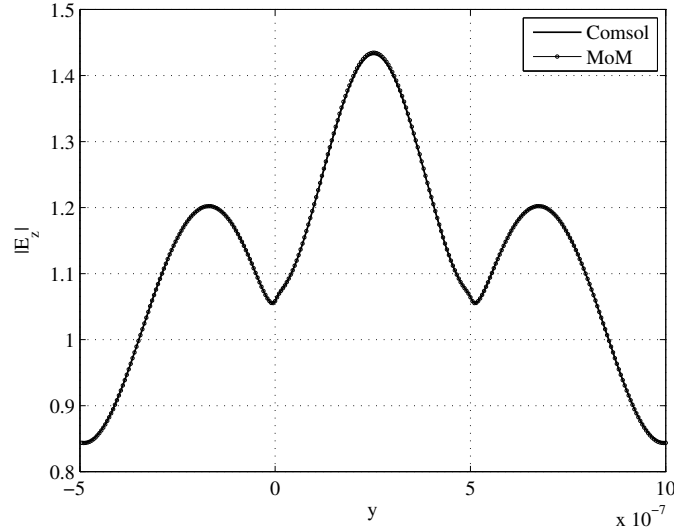
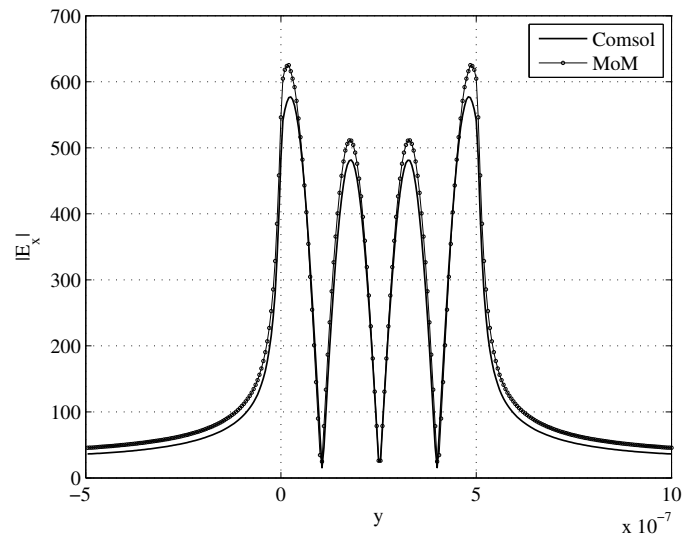


Figure 4.13: Magnitude of the field in z -direction due to the normal incident TM mode plane wave at 500 THz. The field is calculated over the cross-section shown as a line in Fig. 4.12. The dielectric material is between $y = 0$ and $y = 500$ nm.

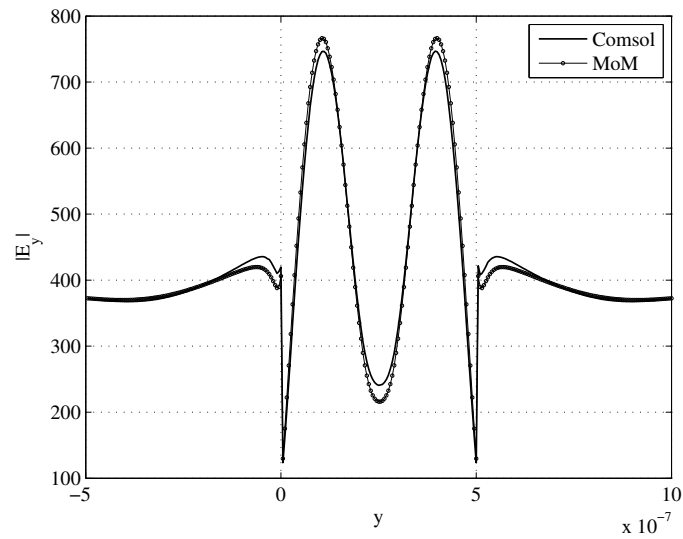
field is a plane wave impinging normally on the system from left where free-space wavelength is $\lambda_0 = 650$ nm and the fields are obtained along the interval close to the surface of the metal demonstrated as a line of cross-section in Fig. 4.15. The field E_z resulting from TM mode excitation is demonstrated in Fig. 4.16 compared to the field obtained via Comsol. Similarly, the TE mode fields E_x and E_y are shown in 4.17(a) and 4.17(b), respectively. For TE polarization, an SPP is observed along the surface of the metallic scatterer as expected. It is well known that nano-slits are one of the sources of the surface plasmon. The surface plasmon is excited by the incident wave at the slit entrance and propagates along the slit region.

4.6. Conclusion

MoM is one of the widely used full-wave methods for the analysis of open structures and the performance of MoM is highly dependent on the Matrix filling time at least for the moderate-size geometries. In this work, a novel method based on the spatial-



(a)



(b)

Figure 4.14: Magnitude of the field in x and y-direction due to the normal incident TE mode plane wave at 500 THz. The field is calculated over the cross-section shown as a line in Fig. 4.12. The dielectric material is between $y = 0$ and $y = 500$ nm.

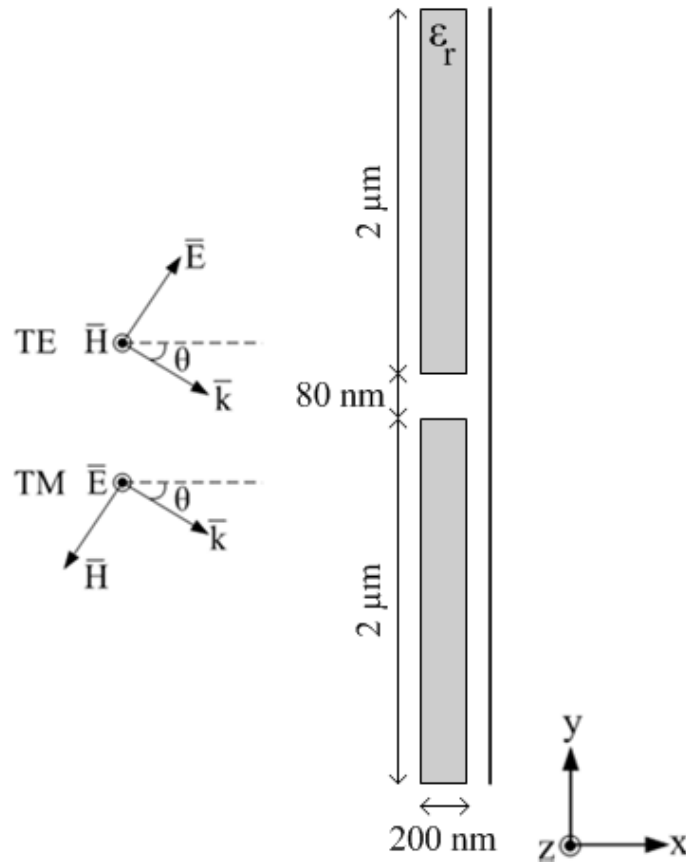


Figure 4.15: A metallic structure with a single slit in free space with the relative permittivity $\epsilon_r = -16.19j - j1.05$ where free-space wavelength is $\lambda_0 = 650$ nm. The width and height of the metallic bars are 200nm and $2\mu\text{m}$, respectively. The width of the slit is 80nm. The system is excited by the plane waves in TM and TE mode and the resulting fields are calculated for the cross-section shown as a line.

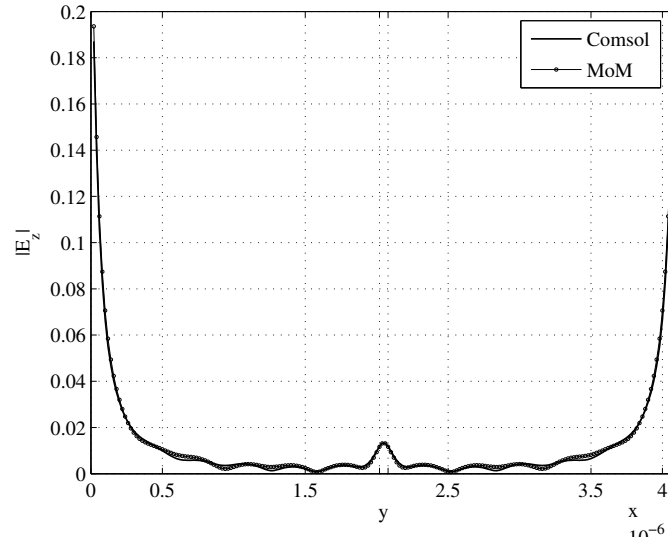
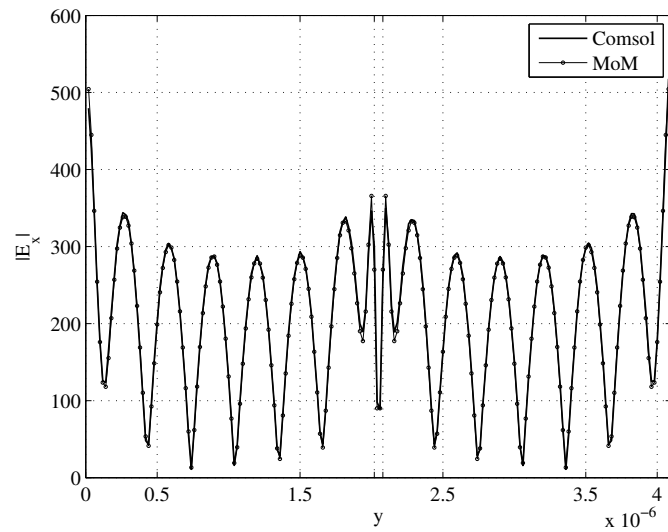
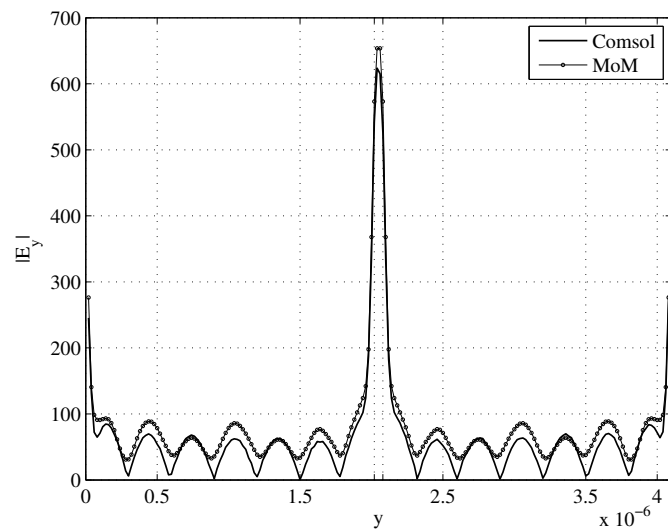


Figure 4.16: Magnitude of the field in z-direction due to the normal incident TM mode plane wave at 500 THz. The field is calculated over the cross-section shown as a line in Fig. 4.15. The slit region is demonstrated with two additional grids at the center of the figure.

domain MoM to the solution of EFIE is proposed for the analysis of 2D systems in free space. The spatial-domain analysis of MoM in conjunction with inverse Fourier representation of the spatial-domain free-space Green's function yields an infinite integral which should be evaluated numerically for each matrix entry. In order to avoid this time consuming operation, the integrand except for the exponential terms is approximated in terms of complex exponentials so that a closed-form expression is obtained for the integral with the help of a particular integral identity. The efficiency arises from the fact that the approximated expressions are independent of the matrix indices therefore they are approximated only once and all the elements of the MoM matrix are obtained from the same closed form expression. In addition, the fields are obtained directly from the current densities inside the material and by using exactly same expressions in MoM calculations outside of the material which improves the efficiency of the method. Several dielectric and metallic structures are analyzed by the proposed method and the fields found by the method are compared to the results



(a)



(b)

Figure 4.17: Magnitude of the field in x and y-direction due to the normal incident TE mode plane wave at 500 THz. The field is calculated over the cross-section shown as a line in Fig. 4.15. The slit region is demonstrated with two additional grids at the center of the figure.

obtained by the simulation tool *Comsol Multiphysics* by Comsol Inc., for verification.

Chapter 5

Conclusion and Recommendations for Future Work

The work presented in this thesis has proposed the following developments which overcame the computational difficulties to develop an efficient and accurate numerical technique that could analyze two-dimensional nano-structures in multilayered environment in the optical regime:

- The development of a spatial-domain error criterion to the DCIM algorithm used for the approximation of the spatial-domain Green's functions.
- The elimination of the leakage problem which is inherent to the semi-independent processing of subregions in multilevel implementations of the DCIM.
- The elimination of the manual selection of the complex images in the DCIM algorithm and development of an automatic order selection routine by adopting a model selection approach, known as minimum description length, to DCIM algorithm.
- The development of an efficient MoM based approach for the analysis of 2D (dielectric and/or metallic) structures in free-space by introducing an explicit

expression to evaluate all MoM matrix entries.

As an additional study, a versatile tool which is used to verify the correctness of expressions found for MoM matrix entries (discussed in Chapter 4) has been presented:

- The development of a novel computational method to evaluate 1D and 2D integrals and summations which do not have analytical solutions and relatively difficult to be computed numerically.

Since the majority of the issues studied in this thesis are the subjects of the DCIM algorithm and the improvements were applied to the latest version of the DCIM called three-level DCIM, an overview of the method has been presented in Chapter 2 and the spatial error criterion together with the leakage elimination has been proposed. It has been showed that instead of using OLS, WLS optimization needs to be employed to map the error criterion from the spatial to the spectral domain.

In Chapter 3, an automatic order selection among the complex images has been proposed by using the MDL approach with the help of the spatial-domain error criterion proposed previously. Due to the fact that the spatial error is guaranteed to be smaller as the number of terms increased, the MDL adoption has become applicable. Since MDL approach is not quite familiar to the EM community, an overview of the idea is presented first. Then the method has been successfully applied to many different geometries and different components of the Green's functions.

After developing a complete and correct DCIM algorithm to obtain the spatial-domain Green's function in layered media, we have focused on the analysis of the 2D structures in free space via a MoM-based approach and proposed a novel method in Chapter 4. The proposed approach has employed the spatial-domain MoM in conjunction with the exponential approximation method. The efficiency of the method has been achieved by obtaining analytical expressions for the entries of the MoM matrices. The derivations of the proposed approach has been given by discussing the two propagation modes (TM and TE) in detail and the analyses of several dielectric and metallic 2D systems have been performed by the method.

As the final study, an efficient and versatile computational method has been proposed for the evaluation of 1D and 2D integrals and summations. The proposed method approximate a set of partial sums as a sum of complex exponential and the DC term of this summation becomes the end result. The proposed approach has been applied to various 1D and 2D examples for verification of the method. Since this study is a side problem and does not directly make a contribution to the MoM concept, it has been presented in the Appendix part of the thesis.

There exist many possibilities for the future work to improve and widen the contributions of the work presented in this thesis. Some of them are outlined below.

As stated several times, this thesis overcomes the computational difficulties to develop an efficient and accurate numerical technique that could analyze two-dimensional nano-structures in multilayered environment. Although these problems are remedied and the proposed MoM-based approach for the analysis of 2D structures in free space can be extended to multilayered environment in a straightforward manner, this part has been left for the future study because of its numerical inefficiency. Basically, the extension can be achieved by considering each term in the closed-form approximation of the Green's function as the Green's function in free space with complex source location but it needs further improvements.

For the DCIM approach with the spatial error criterion, instead of employing a linear weighting function for the error metric, different weighting functions can be investigated and if the resulting integrals can be evaluated accurately and efficiently, the windowing (emphasizing a particular interval in the spatial domain) can also be possible.

Finally, the MoM based approach which is used for the 2D systems in free space can be extended to analyze the 3D structures. In this case, the spatial domain MoM in free space yields eight integrations: three for the convolution of the basis and Green's functions and three for the testing procedure. Since these integrals are definite over a discretization cell, they can be evaluated analytically. The double integral left without evaluation will come from the inverse Fourier transform of the spatial

domain Green's function for a point source. As a result, this double integral must be evaluated for each MoM matrix entry. To employ the similar idea of 2D systems, the integrand except for the exponential terms must be approximated in terms of complex exponentials but this time the approximation must be performed in two-dimensional spectral domain. Therefore GPOF can not be used but many efficient two-dimensional frequency estimation methods (such as ACMP [75], MEMP [76], 2D Prony method [77] and 2D ESPRIT-type method [78]) are available in the literature. Once the term is approximated, the Weyl's identity [43] can be used for the analytic evaluation.

Appendices

Appendix A

Derivations of the second EFIE for the TE mode excitation

With the use of the Green's Function expression

$$G(x, y; x', y') = \frac{1}{2\pi} \int_{-\infty}^{+\infty} dk_y \frac{e^{-jk_x|x-x'| - jk_y(y-y')}}{j2k_x}, \quad (\text{A.1})$$

which is equivalent to (4.36) and the corresponding Hankel identity

$$H_0^{(2)}(k_\rho \rho) = \frac{1}{\pi} \int_{-\infty}^{+\infty} \frac{dk_y}{k_x} e^{-jk_x|x-x'| - jk_y(y-y')} \quad (\text{A.2})$$

with $\rho = \sqrt{|x-x'|^2 + (y-y')^2}$, the derivation of the second EFIE becomes very similar to the first EFIE except for the fact that the expressions for x-dependent values are valid for y-dependent ones, and vice versa.

For the evaluation of the integrals which are over infinite k_y domain, exponential approximation allows expressing the integrand apart from $1/k_x$ and exponential terms as a sum of complex exponentials. Therefore the integral can be evaluated as a sum of Hankel functions with the appropriate arguments similar to the case in the first EFIE. In addition, if the discretization in MoM yields $h_x = h_y$ then exactly the same terms as in the first EFIE appear for the second EFIE to be approximated. Hence one does not need to perform exponential approximation for the second EFIE. Here

the terms related to the second EFIE in (4.76) and corresponding field calculations in (4.85) are listed as follows:

• \mathbf{Z}_{21} :

1. For $(m' - m) \geq 1$:

$$\begin{aligned}
Z_{21m'n',mn} &= \frac{h_x^2 h_y^2}{8\omega\epsilon_0} \frac{1}{\pi} \int_{-\infty}^{+\infty} \frac{dk_y}{k_x} e^{-jk_x(m'-m)h_x} e^{-jk_y(n'-n)h_y} \\
&\times (-k_x k_y) \text{sinc}^2(k_x h_x/2) \text{sinc}^2(k_y h_y/4) \text{sinc}(k_y h_y/2) \\
&= \frac{h_x^2 h_y^2}{8\omega\epsilon_0} \frac{\partial}{\partial x} \frac{1}{\pi} \int_{-\infty}^{+\infty} \frac{dk_y}{k_x} e^{-jk_x(m'-m)h_x} e^{-jk_y(n'-n)h_y} \\
&\times (-jk_x) \text{sinc}^2(k_x h_x/2) \text{sinc}^2(k_y h_y/4) \text{sinc}(k_y h_y/2) \\
&= \frac{h_x^2 h_y^2}{8\omega\epsilon_0} \frac{\partial}{\partial y} \frac{1}{\pi} \int_{-\infty}^{+\infty} \frac{dk_y}{k_x} e^{-jk_x(m'-m)h_x} e^{-jk_y(n'-n)h_y} \sum_t a_t e^{-\alpha_t k_x} \\
&= \frac{h_x^2 h_y^2}{8\omega\epsilon_0} \frac{\partial}{\partial y} \sum_t a_t H_0^{(2)}(k\rho_t) \\
&= \frac{h_x^2 h_y^2}{8\omega\epsilon_0} \sum_t \frac{-a_t k_0}{\rho_t} [(m' - m)h_x - j\alpha_t] H_1^{(2)}(k\rho_t) \tag{A.3}
\end{aligned}$$

where $\rho_t = \sqrt{((m' - m)h_x - j\alpha_t)^2 + ((n' - n)h_y)^2}$;

2. For $(m - m') \geq 1$:

$$\begin{aligned}
Z_{21m'n',mn} &= \frac{h_x^2 h_y^2}{8\omega\epsilon_0} \frac{1}{\pi} \int_{-\infty}^{+\infty} \frac{dk_y}{k_x} e^{-jk_x(m-m')h_x} e^{-jk_y(n'-n)h_y} \\
&\quad \times (k_x k_y) \text{sinc}^2(k_x h_x/2) \text{sinc}^2(k_y h_y/4) \text{sinc}(k_y h_y/2) \\
&= \frac{h_x^2 h_y^2}{8\omega\epsilon_0} \frac{\partial}{\partial y} \frac{1}{\pi} \int_{-\infty}^{+\infty} \frac{dk_y}{k_x} e^{-jk_x(m-m')h_x} e^{-jk_y(n'-n)h_y} \\
&\quad \times (jk_x) \text{sinc}^2(k_x h_x/2) \text{sinc}^2(k_y h_y/4) \text{sinc}(k_y h_y/2) \\
&= \frac{h_x^2 h_y^2}{8\omega\epsilon_0} \frac{\partial}{\partial y} \frac{1}{\pi} \int_{-\infty}^{+\infty} \frac{dk_y}{k_x} e^{-jk_x(m-m')h_x} e^{-jk_y(n'-n)h_y} \sum_t a_t e^{-\alpha_t k_x} \\
&= \frac{h_x^2 h_y^2}{8\omega\epsilon_0} \frac{\partial}{\partial} \sum_t a_t H_0^{(2)}(k\rho_t) \\
&= \frac{h_x^2 h_y^2}{8\omega\epsilon_0} \sum_t \frac{-a_t k_0}{\rho_t} [(m - m')h_x - j\alpha_t] H_1^{(2)}(k\rho_t) \tag{A.4}
\end{aligned}$$

where $\rho_t = \sqrt{((m - m')h_x - j\alpha_t)^2 + ((n' - n)h_y)^2}$.

3. For $m' = m$: $Z_{21m'n',mn} = 0$

• \mathbf{Z}_{22} :

1. For $|m' - m| \geq 1$:

$$\begin{aligned}
Z_{22m'n',mn} &= \frac{\omega\mu_0}{8} h_x^2 h_y^2 \frac{1}{\pi} \int_{-\infty}^{+\infty} \frac{dk_y}{k_x} e^{-jk_x|m'-m|h_x} e^{-jk_y(n'-n)h_y} \left(1 - \frac{k_y^2}{k_0^2}\right) \\
&\quad \times \text{sinc}^2(k_x h_x/2) \text{sinc}^2(k_y h_y/4) \text{sinc}(k_y h_y/2) \\
&= \frac{\omega\mu_0}{8} h_x^2 h_y^2 \frac{1}{\pi} \int_{-\infty}^{+\infty} \frac{dk_y}{k_x} e^{-jk_x|m'-m|h_x} e^{-jk_y(n'-n)h_y} \sum_t a_t e^{-\alpha_t k_x} \\
&= \frac{\omega\mu_0}{8} h_x^2 h_y^2 \sum_t a_t H_0^{(2)}(k\rho_t) \tag{A.5}
\end{aligned}$$

where $\rho_t = \sqrt{(|m' - m|h_x - j\alpha_t)^2 + ((n' - n)h_y)^2}$;

2. For $m' = m$:

$$\begin{aligned}
Z_{22m'n',mn} &= \frac{h_x h_y}{jk_0 Y_0(\epsilon_r - 1)} \delta_{n'n} + \frac{\omega \mu_0}{8} h_x^2 h_y^2 \frac{1}{\pi} \int_{-\infty}^{+\infty} \frac{dk_y}{k_x} e^{-jk_y(n'-n)h_y} \left(1 - \frac{k_y^2}{k_0^2}\right) \\
&\quad \times \text{sinc}^2(k_y h_y/4) \text{sinc}(k_y h_y/2) \frac{2}{jk_x h_x} (1 - e^{-jk_x h_x/2} \text{sinc}(k_x h_x/2)) \\
&= \frac{h_x h_y}{jk_0 Y_0(\epsilon_r - 1)} \delta_{n'n} + \frac{\omega \mu_0}{8} h_x^2 h_y^2 \frac{1}{\pi} \int_{-\infty}^{+\infty} \frac{dk_y}{k_x} e^{-jk_y(n'-n)h_y} \sum_t a_t e^{-\alpha_t k_x} \\
&= \frac{h_x h_y}{jk_0 Y_0(\epsilon_r - 1)} \delta_{n'n} + \frac{\omega \mu_0}{8} h_x^2 h_y^2 \sum_t a_t H_0^{(2)}(k \rho_t) \tag{A.6}
\end{aligned}$$

$$\text{where } \rho_t = \sqrt{(-j\alpha_t)^2 + ((n' - n)h_y)^2}.$$

• The excitation vector \mathbf{R}_2 :

$$\mathbf{R}_2 = [\langle T_{y11}, E_y^i \rangle \dots \langle T_{yN_x N_y}, E_y^i \rangle]^T, \tag{A.7}$$

where

$$E_y^i = E_{oy} e^{-j(k_{x0}x + k_{y0}y)} \tag{A.8}$$

and

$$\langle T_{ym'n'}, E_y^i \rangle = E_{oy} h_x h_y e^{-j(k_{x0}m'h_x + k_{y0}n'h_y)} \text{sinc}(k_{x0}h_x/2) \text{sinc}^2(k_{y0}h_y/4). \tag{A.9}$$

• $\mathbf{Z}_{f21} = -\mathbf{Z}_{21}$

• \mathbf{Z}_{f22}

1. For $|m' - m| \geq 1$:

$$Z_{f22m'n',mn} = -Z_{22m'n',mn} \tag{A.10}$$

2. For $m' = m$:

$$\begin{aligned}
Z_{f22m'n',mn} &= \frac{-\omega\mu_0}{8} h_x^2 h_y^2 \frac{1}{\pi} \int_{-\infty}^{+\infty} \frac{dk_y}{k_x} e^{-jk_y(n'-n)h_y} \left(1 - \frac{k_y^2}{k_0^2}\right) \\
&\quad \times \operatorname{sinc}^2(k_y h_y/4) \operatorname{sinc}(k_y h_y/2) \frac{2}{jk_x h_x} (1 - e^{-jk_x h_x/2} \operatorname{sinc}(k_x h_x/2)) \\
&= \frac{-\omega\mu_0}{8} h_x^2 h_y^2 \frac{1}{\pi} \int_{-\infty}^{+\infty} \frac{dk_y}{k_x} e^{-jk_y(n'-n)h_y} \sum_t a_t e^{-\alpha_t k_x} \\
&= \frac{-\omega\mu_0}{8} h_x^2 h_y^2 \sum_t a_t H_0^{(2)}(k\rho_t) \tag{A.11}
\end{aligned}$$

where $\rho_t = \sqrt{(-j\alpha_t)^2 + ((n' - n)h_y)^2}$.

Appendix B

A Novel Approach for Fast Evaluation of 1D and 2D Infinite Summations

B.1. Abstract

A novel computational method is proposed to evaluate 1-D and 2-D infinite summations that are relatively difficult to compute numerically. The method is based on a subspace algorithm, which uses a set of partial sums to approximate the trend of these sums in terms of complex exponentials. For a convergent summation, it is expected that one of the exponential terms will turn out to be with vanishingly small exponent (ideally zero), corresponding to the result of the summation. Since the procedure requires the evaluation of relatively small number of terms, in addition to the subspace algorithm, the computational cost of the evaluation of the summation is significantly reduced.

B.2. Introduction

In many engineering applications, relatively difficult infinite summations with quite complex terms need to be computed numerically. These applications may include the

calculation of free-space or planar-media periodic Green's functions in electromagnetics (EM), the determination of the electrostatic energy of ionic crystals in chemistry and the nucleic acid simulations in molecular dynamics. The difficulty of such computations usually arises from the fast oscillatory and slowly convergent nature of the summations. For instance, the EM analysis of cylindrical geometries may require the computation of slow convergent infinite summations of cylindrical Hankel and Bessel type functions; in numerical simulations of periodic structures, e.g. in the analysis of antenna arrays and photonic band gap materials, the periodic Green's functions need to be calculated for each impedance matrix elements in the method of moments, requiring the evaluation of many infinite summations of complex functions to fill in the entire matrix.

In this study, a novel method is proposed to compute slowly convergent summations. In principle, the idea of the method is as follows: if one i) takes a sufficient series of partial sums, and ii) considers them as a set of data, and iii) approximates the data as a sum of complex exponentials, the DC term (the residue of the exponential with zero complex pole) of this approximation would be the result of the summation of interest. The method is quite efficient and robust because of the fact that the partial sums of an infinite summation always exhibit an oscillating or monotonic behavior, and if the summation is convergent, the corresponding behavior dies out eventually and leads towards a DC term, which is the result of the summation. Therefore, the partial sums are approximated in terms of exponentials to find this zero frequency term. In order to approximate the data as a series of complex exponentials, a subspace approach called the generalized pencil of function (GPOF [53]) is employed. For the sake of demonstration, the method is first applied to a 1-D problem with a known analytical result, and its performance is compared to the direct summation in terms of the computation time. Then, the free-space periodic Green's function (FSPGF) taken from [79] is computed by the proposed method, for its verification in 2-D summations, and the results are compared with those obtained by the Ewald method [80]. It should be noted that, the proposed method can also be applied to

1-D and 2-D slowly convergent infinite *integrals* by converting them into infinite summations. Since the main idea is the same, once a sufficient set of partial integrals is obtained, the rest of the algorithm becomes exactly the same. However, for the sake of coherence and brevity, no examples on integrations are provided in this paper.

The theory of the method and the details of its implementation on 1-D and 2-D summations are discussed in Section 2. Section 3 provides some numerical results, and conclusions are drawn in Section 4.

B.3. Theory of the Method

In this section, the principle idea of the method for 1-D summations is demonstrated and its extension to 2-D summations is discussed. Consider the infinite 1-D summation S for the series f which is in general slowly convergent. Unless an analytic solution for S exists, the summation is supposed to be truncated at a certain relatively large n value for its numerical evaluation. Thus, if the summation converges, it can be calculated as

$$S = \sum_{n=0}^{\infty} f(n) \simeq S_{N_t} = \sum_{n=0}^{N_t} f(n), \quad (\text{B.1})$$

where N_t is the upper bound summation for truncation. However for (B.1) to be correct, N_t is in general very large in particular for slowly convergent summations. In addition, if the summation is fast oscillating, the numerical accuracy becomes questionable for large n values. Therefore even with very large N_t value, S may not be found. The method in this study is developed to find S without necessity of large N_t values. The idea is based on the use of GPOF over a set of partial sums of a given summation

$$\mathbf{S} = \left[S_1 \quad S_2 \quad \dots \quad S_{N_s} \right]^T, \quad (\text{B.2})$$

where

$$S_m = \sum_{n=0}^{mN_a-1} f(n) \equiv S_{m-1} + \sum_{n=(m-1)N_a}^{mN_a-1} f(n), \quad m = 1, \dots, N_s, \quad (\text{B.3})$$

where N_s is the number of partial sums, N_a is the number of terms added to each partial sum in \mathbf{S} , assuming $S_0 = 0$. Note that, since the partial sums can be obtained iteratively as shown in (B.3), \mathbf{S} is computed by adding only $N_a \times N_s$ terms and \mathbf{S} can be considered as a function of m for constant N_a . In general, $N_a \times N_s$ is far less than N_t , which is the essential advantage of the method. If the partial sums are used as the samples to be input for GPOF, \mathbf{S} vs. m can be approximated in terms of M complex exponentials as

$$\mathbf{S} \cong \hat{\mathbf{S}} = \sum_{i=1}^M b_i e^{s_i m N_a}, \quad (\text{B.4})$$

where $\hat{\mathbf{S}}$ is the approximation of \mathbf{S} , b_i are the complex residues and s_i are the complex poles. Thus, when the limiting value of $\hat{\mathbf{S}}$ is considered as $m \rightarrow \infty$

$$\lim_{m \rightarrow \infty} \hat{\mathbf{S}} = \lim_{m \rightarrow \infty} \sum_{i=1}^M b_i e^{s_i m N_a} \quad (\text{B.5})$$

yields two possibilities:

- If S is divergent, then at least one of the complex poles has a positive real part, i.e. $\Re\{s_i\} > 0$ for at least one i value where $i = 1, \dots, M$ and
- If S is convergent, then all except one complex poles have negative real part and one complex pole is zero, i.e. $\Re\{s_i\} \Big|_{i \neq k} < 0$ for $i = 1, 2, \dots, k-1, k+1, \dots, M$ and $s_k = 0$. Then the corresponding complex residue, b_k , becomes the result of the summation S .

It is important to note that the efficiency of the algorithm is strongly dependent on the behavior of \mathbf{S} vs. m and thus N_a , however the relation between the behavior of $f(n)$ and \mathbf{S} vs. m is not clear. Intuition and the numerical examples used for the verification of the method suggest that if $f(n)$ is fast or slowly oscillating so is \mathbf{S} vs. m and the relation of these parameters are currently under investigation.

For 2-D summations, the idea can be directly extended since once the partial sums are computed to be used in GPOF, the rest of the procedure is the same. Consider

the infinite 2-D summation

$$S = \sum_{i=0}^{\infty} \sum_{j=0}^{\infty} f(i, j) \quad (\text{B.6})$$

where f is a function of two variables in this case and the partial sums can be computed as

$$S_m = \sum_{i=0}^{(mN_{a1}-1)} \sum_{j=0}^{(mN_{a2}-1)} f(i, j), \quad m = 1, \dots, N_s, \quad (\text{B.7})$$

where N_{a1} and N_{a2} correspond to sampling interval for two dimensions and they can be different depending the behavior of $f(i, j)$, i.e. the convergence in two dimensions can be different, therefore one can adjust N_{a1} and N_{a2} values accordingly. Once S_m values are computed, they can be approximated in terms of complex exponentials and similarly the residue of the exponential term with zero complex pole corresponds to the result of the summation.

B.4. Numerical Results

In this section, some numerical examples are provided to assess and validate the proposed method for 1-D and 2-D summations. The method is first applied to a typical 1-D slowly converging summation

$$S = \sum_{n=1}^{\infty} \frac{\cos(n\Delta\phi)}{n} = -\log \left(2\sin \left(\frac{\Delta\phi}{2} \right) \right) \quad (\text{B.8})$$

with an analytical result, which is $S = 7.41858$ when $\Delta\phi = 0.0006$. The proposed method reaches six significant figures with parameters $N_s = 43$ and $N_a = 1000$ and its performance is compared with the direct summation as demonstrated in Table-1. As seen, although the direct summation reaches the correct result at a very large N_t value, the proposed approach uses only $N_a \times N_s = 43,000$ terms, decreasing the cpu-time dramatically. Fig. B.1 demonstrates \mathbf{S} vs. m curve which has an oscillatory behavior, as expected. According to the method, the zero frequency term of its approximation, which is also represented in figure, corresponds to the final result of the summation.

Method	No. of Terms	CPU-Time
Direct Summation	200,000,000	10.49 sec.
Proposed Method	43,000	0.007571 sec.

Table B.1: The performance comparison of the proposed method and direct summation for 1-D infinite summation with regard to CPU-time.

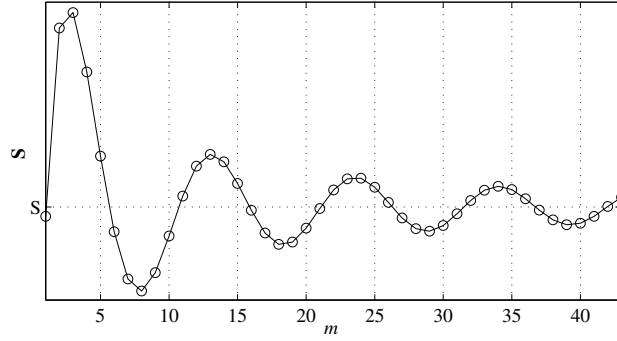


Figure B.1: \mathbf{S} vs. m of the summation in (B.8), where $m = 1, \dots, N_s = 43$. $S = 7.41858$ is equivalent to the zero frequency term of its complex-exponential approximation and hence the result of the summation.

For the 2-D summation example, FSPGF of an infinite periodic array is found by the proposed method. The calculation of FSPGF is an important problem in physics and engineering and the EWALD method is a popular method to efficiently evaluate the FSPGF. For this reason, we validate the performance of the proposed method by comparing it with the EWALD method. The spatial domain FSPGF for a 2-D periodic array on a general skewed lattice extending on the $x - y$ plane is given as (according to $e^{j\omega t}$ time dependence):

$$G(\mathbf{r}, \mathbf{r}') = \sum_{m=-\infty}^{\infty} \sum_{n=-\infty}^{\infty} e^{j\mathbf{k}_{t00} \cdot \rho_{mn}} \left(\frac{e^{-jkR_{mn}}}{4\pi R_{mn}} \right) = \frac{1}{A} \sum_{p=-\infty}^{\infty} \sum_{q=-\infty}^{\infty} \frac{1}{2jk_{zpq}} e^{-j\mathbf{k}_{tpq} \cdot (\rho - \rho')} e^{-jk_{zpq}|z - z'|}, \quad (\text{B.9})$$

where A is the cross sectional area of each lattice cell, R_{mn} is the distance between

the observation point at $\mathbf{r} = (x, y, z)$ and the (m, n) 'th periodic source point, k_{t00} is the transverse phasing wave-vector and ρ_{mn} is the position vector of the (m, n) 'th source point relative to the reference source at $\mathbf{r}' = (x', y', z')$, \mathbf{k}_{tpq} is the transverse wavenumber, $k_{zpq} = \sqrt{k^2 - \mathbf{k}_{tpq}^2}$ and $k = 2\pi/\lambda$. The performances of two methods are compared for an example of a square lattice of dimension $0.5m$ with $x = y = x' = y' = 0$ and $|z - z'| = 0.05m$ and at the frequency for $a/\lambda = 0.5$ and presented in Table-2. For this example, the result of the summation is given as $G(\mathbf{r}, \mathbf{r}') = 1.10173 - j0.30273$. Table-2 shows that the proposed method reaches the result of the summation faster than the Ewald method does. Note that, although the Ewald Method uses less number of terms, its computation time is longer, since the Ewald method needs to evaluate the complementary error function for each term.

Method	No. of Terms	CPU-Time
Ewald	$3 \times 3 \times 2$	0.021511 sec.
Proposed Method	11×11	0.002672 sec.

Table B.2: The performance comparison of the proposed method and the Ewald method for the evaluation of FSPGF with regard to CPU-time.

B.5. Conclusion

In this study, we presented a novel method to evaluate 1-D and 2-D infinite slowly converging summations efficiently. The method is based on the idea that the partial sums of a convergent summation always has a nature culminating in a zero frequency value eventually, which becomes the result of the summation. In order to acquire this value, a series of partial sums are obtained and approximated in terms of complex exponentials where the zero frequency term among them corresponds to the end result. The method is applied to typical examples for 1-D and 2-D summations and compared with the direct summation and the Ewald method, respectively.

Bibliography

- [1] Schinzinger R. and Laura P. A. A, *Conformal Mapping: Methods and Applications*, , New York: Elsevier, 1991.
- [2] P. Silvester and P. Benedek, “Equivalent Capacitances of Microstrip Open Circuits,” *Microwave Theory and Techniques, IEEE Transactions on*, vol. 20, no. 8, pp. 511–516, Aug. 1972.
- [3] P. Benedek and P. Silvester, “Equivalent Capacitances for Microstrip Gaps and Steps,” *Microwave Theory and Techniques, IEEE Transactions on*, vol. 20, no. 11, pp. 729–733, Nov. 1972.
- [4] P. Silvester and P. Benedek, “Microstrip Discontinuity Capacitances for Right-Angle Bends, T Junctions, and Crossings,” *Microwave Theory and Techniques, IEEE Transactions on*, vol. 21, no. 5, pp. 341–346, May 1973.
- [5] J. Jin, *The Finite Element Method in Electromagnetics*, New York: Wiley, 1993.
- [6] John L. Volakis, Arindam Chatterjee, and Leo C. Kempel, *Finite Element Method Electromagnetics: Antennas, Microwave Circuits, and Scattering Applications (IEEE Press Series on Electromagnetic Wave Theory)*, Wiley-IEEE Press, 1 edition, June 1998.
- [7] K. Kunz and R. Luebber, *The Finite Difference Time Domain Method for Electromagnetics*, Boca Raton, FL: CRC Press, 1993.

-
- [8] A. Taflove and S. C. Hagness, *Computational Electrodynamics: The Finite-Difference Time-Domain Method*, Norwood, MA: Artech House, 2000.
- [9] R.F Harrington, "Matrix methods for field problems," *Proc. IEEE*, vol. 55, no. 2, pp. 136–149, Feb 1967.
- [10] R. F. Harrington, *Field Computation by Moment Methods*, Florida: Robert E. Krieger Publishing Company, 1982.
- [11] J. R. Mosig, "Arbitrarily shaped microstrip structures and their analysis with a mixed potential integral equation," *Microwave Theory and Techniques, IEEE Transactions on*, vol. 36, no. 2, pp. 314–323, Feb. 1988.
- [12] K. Naishadham and T. W. Nuteson, "Efficient analysis of passive microstrip elements in MMICs," *Int. J. Microw. Mill.-Wave Comput.-Aided Eng.*, vol. 4, no. 3, pp. 219–229.
- [13] I. Park, R. Mittra, and M. I. Aksun, "Numerically efficient analysis of planar microstrip configurations using closed-form Green's functions," *Microwave Theory and Techniques, IEEE Transactions on*, vol. 43, no. 2, pp. 394–400, 1995.
- [14] Noyan Kinayman and M. I. Aksun, "Efficient and accurate EM simulation technique for analysis and design of MMICs," *Int. J. Microw. Mill.-Wave Comput.-Aided Eng.*, vol. 7, no. 5, pp. 344–358, 1997.
- [15] J. R. Mosig and F. E. Gardiol, "A dynamical radiation model for microstrip structures," in *Advances in Electronics and Electron Physics*, P. W. Hawkes, Ed. 1982, vol. 59, pp. 139–237, New York: Academic.
- [16] N. Kinayman and M. I. Aksun, "Comparative study of acceleration techniques for integrals and series in electromagnetic problems," *Radio Science*, vol. 30, pp. 1713–1722, Nov.-Dec. 1995.

-
- [17] M. I. Aksun and R. Mittra, "Derivation of closed-form green's functions for a general microstrip geometry," *Microwave Theory and Techniques, IEEE Transactions on*, vol. 40, no. 11, pp. 2055–2062, Nov. 1992.
- [18] G. Dural and M. I. Aksun, "Closed-form green's functions for general sources and stratified media," *Microwave Theory and Techniques, IEEE Transactions on*, vol. 43, no. 7, pp. 1545–1552, Jul. 1995.
- [19] M. I. Aksun, "A robust approach for the derivation of closed-form green's functions," *Microwave Theory and Techniques, IEEE Transactions on*, vol. 44, no. 5, pp. 651–658, May. 1996.
- [20] C. Tokgoz and G. Dural, "Closed-form green's functions for cylindrically stratified media," *Microwave Theory and Techniques, IEEE Transactions on*, vol. 48, no. 1, pp. 40–49, Jan. 2000.
- [21] Y. Ge and K. P. Esselle, "New closed-form green's functions for microstrip structures theory and results," *Microwave Theory and Techniques, IEEE Transactions on*, vol. 50, no. 6, pp. 1556–1560, Jun. 2002.
- [22] N. V. Shuley, R. R. Boix, F. Medina, and M. Horno, "On the fast approximation of green's functions in mpie formulations for planar layered media," *Microwave Theory and Techniques, IEEE Transactions on*, vol. 50, no. 9, pp. 2185–2192, Sep. 2002.
- [23] V. I. Okhmatovski and A. C. Cangellaris, "A new technique for the derivation of closed-form electromagnetic green's functions for unbounded planar layered media," *Antennas and Propagation, IEEE Transactions on*, vol. 50, no. 7, pp. 1005–1016, Jul. 2002.
- [24] V. I. Okhmatovski and A. C. Cangellaris, "Evaluation of layered media green's

- functions via rational function fitting,” *Microwave and Wireless Components Letters, IEEE*, vol. 14, no. 1, pp. 22–24, Jan. 2004.
- [25] M. I. Aksun and G. Dural, “Clarification of issues on the closed-form green’s functions in stratified media,” *Antennas and Propagation, IEEE Transactions on*, vol. 53, no. 11, pp. 3644–3653, Nov. 2005.
- [26] M. Yuan, T. K. Sarkar, and M. Salazar-Palma, “A direct discrete complex image method from the closed-form green’s functions in multilayered media,” *Microwave Theory and Techniques, IEEE Transactions on*, vol. 54, no. 3, pp. 1025–1032, Mar. 2006.
- [27] V. N. Kourkoulos and A. C. Cangellaris, “Accurate approximation of green’s functions in planar stratified media in terms of a finite sum of spherical and cylindrical waves,” *Antennas and Propagation, IEEE Transactions on*, vol. 54, no. 5, pp. 1568–1576, May 2006.
- [28] L. Zhuang, G. Zhu, Y. Zhang, and B. Xiao, “An improved discrete complex image method for green’s functions in multilayered media,” *Microwave and Optical Technology Letters*, vol. 49, no. 6, pp. 1337–1340, 2007.
- [29] R. R. Boix, F. Mesa, and F. Medina, “Application of total least squares to the derivation of closed-form green’s functions for planar layered media,” *Microwave Theory and Techniques, IEEE Transactions on*, vol. 55, no. 2, pp. 268–280, Feb. 2007.
- [30] A. G. Polimeridis, T. V. Yioultsis, and T. D. Tsiboukis, “An efficient pole extraction technique for the computation of green’s functions in stratified media using a sine transformation,” *Antennas and Propagation, IEEE Transactions on*, vol. 55, no. 1, pp. 227–229, Jan. 2007.

-
- [31] F. Mesa, R. R. Boix, and F. Medina, "Closed-form expressions of multilayered planar green's functions that account for the continuous spectrum in the far field," *Microwave Theory and Techniques, IEEE Transactions on*, vol. 56, no. 7, pp. 1601–1614, Jul. 2008.
- [32] A. Alparslan, M. I. Aksun, and K. A. Michalski, "Closed-form green's functions in planar layered media for all ranges and materials," *Microwave Theory and Techniques, IEEE Transactions on*, vol. 58, no. 3, pp. 602–613, Mar. 2010.
- [33] B. Hu and W. C. Chew, "Fast inhomogenous plane wave algorithm for electromagnetic solutions in layered media structures: Two-dimensional case," *Radio Science*, vol. 35, pp. 31–43, Jan.-Feb. 2000.
- [34] M. I. Aksun, F. Caliskan, and L. Gurel, "An efficient method for electromagnetic characterization of 2-d geometries in stratified media," *Microwave Theory and Techniques, IEEE Transactions on*, vol. 50, no. 5, pp. 1264–1274, May 2002.
- [35] R.F Harrington, "The method of moments-a personal review," *IEEE Antennas and Propagation Society International Symposium on*, p. 1639, 2000.
- [36] E. P. Karabulut, A. T. Erdogan, and M. I. Aksun, "Spatial error criterion for discrete complex image method," *Antennas and Propagation (EUCAP), Proceedings of the 5th European Conference on*, pp. 2454 – 2458, 11-15 Apr. 2011.
- [37] E. P. Karabulut, A. T. Erdogan, and M. I. Aksun, "Discrete complex image method with spatial error criterion and automatic order selection," *Antennas and Propagation (APSURSI), 2011 IEEE International Symposium on*, pp. 1577 – 1580, 3-8 Jul. 2011.
- [38] E. P. Karabulut, A. T. Erdogan, and M.I. Aksun, "Discrete complex image method with spatial error criterion," *Microwave Theory and Techniques, IEEE Transactions on*, vol. 59, no. 4, pp. 793–802, Apr. 2011.

- [39] E. P. Karabulut, A. T. Erdogan, and M. I. Aksun, "Discrete Complex Image Method With Automatic Order Selection," *Microwave Theory and Techniques, IEEE Transactions on*, vol. 59, no. 10, pp. 2385–2393, Oct. 2011.
- [40] E. P. Karabulut and M.I. Aksun, "An efficient and accurate mom-based method for the analysis of two dimensional dielectric structures," *Progress In Electromagnetics Research Symposium (PIERS) on*, 18-21 Aug. 2009.
- [41] E. P. Karabulut, V. B. Erturk, S. Adanir, L. Alatan, and M. I. Aksun, "A novel approach for the fast evaluation of 1-d and 2-d summations," *The XXX General Assembly and Scientific Symposium of the International Union of Radio Science (Union Radio Scientifique Internationale-URSI) on*, 13-20 Aug. 2011.
- [42] W. C. Chew, *Waves and Fields in Inhomogeneous Media*, New York: Van Nostrand Reinhold, 1990.
- [43] N. Kinayman and M. I. Aksun, *Modern Microwave Circuits*, Artech House, 2005.
- [44] L. Alatan, M. I. Aksun, K. Mahadevan, and T. Birand, "Analytical evaluation of the mom matrix elements," *Microwave Theory and Techniques, IEEE Transactions on*, vol. 44, no. 4, pp. 519–525, Apr. 1996.
- [45] M. J. Tsai, F. D. Flavis, O. Fordharn, and N. G. Alexopoulos, "Modeling planar arbitrarily shaped microstrip elements in multilayered media," *Microwave Theory and Techniques, IEEE Transactions on*, vol. 45, no. 3, pp. 330–337, Mar. 1997.
- [46] M. R. Abdul-Gaffoor, H. K. Smith, A. A. Kishk, and A. W. Glisson, "Simple and efficient full-wave modeling of electromagnetic coupling in realistic rf multilayer pcb layouts," *Microwave Theory and Techniques, IEEE Transactions on*, vol. 50, no. 6, pp. 1445–1457, Jun. 2002.
- [47] T. Onal, M. I. Aksun, and N. Kinayman, "A rigorous and efficient analysis of 3-d printed circuits: vertical conductors arbitrarily distributed in multilayer

- environment,” *Antennas and Propagation, IEEE Transactions on*, vol. 55, no. 12, pp. 3726–3729, Dec. 2007.
- [48] K. A. Michalski, “Extrapolation methods for sommerfeld integral tails,” *Antennas and Propagation, IEEE Transactions on*, vol. 46, no. 10, pp. 1405–1418, Oct. 1998.
- [49] D. C. Fang, J. J. Yang, and G. Y. Delisle, “Discrete image theory for horizontal electric dipoles in a multilayered medium,” *Proceedings, IEE*, vol. 135, no. 5, pp. 297–303, Oct. 1988.
- [50] Y. L. Chow, J. J. Yang, D. G. Fang, and G. E. Howard, “A closed-form spatial green’s function for the thick microstrip substrate,” *Microwave Theory and Techniques, IEEE Transactions on*, vol. 39, no. 3, pp. 588–592, Mar. 1991.
- [51] B. Wu and L. Tsang, “Fast computation of layered medium green’s functions of multilayers and lossy media using fast all-modes method and numerical modified steepest descent path method,” *Microwave Theory and Techniques, IEEE Transactions on*, vol. 56, no. 6, pp. 1446–1454, Jun. 2008.
- [52] A. G. Polimeridis, T. V. Yioultsis, and T. D. Tsiboukis, “A robust method for the computation of green’s functions in stratified media,” *Antennas and Propagation, IEEE Transactions on*, vol. 55, no. 7, pp. 1963–1969, Jul. 2007.
- [53] Y. Hua and T. K. Sarkar, “Generalized pencil-of-function method for extracting poles of an em system from its transient response,” *Antennas and Propagation, IEEE Transactions on*, vol. 37, no. 2, pp. 229–234, Feb. 1989.
- [54] A. Poulraj, Roy R., and Kailath T., “A subspace rotation approach to signal parameter estimation,” *Proceedings, IEEE*, vol. 74, no. 7, pp. 1044–1045, Jul. 1986.
- [55] T. M. Apostol, *Mathematical Analysis*, Reading, MA: Addison-Wesley, 1974.

-
- [56] F. Bowman, *Introduction to Bessel Functions*, New York: Dover, 1958.
- [57] A. Alparslan, *Study of Green's functions of potentials and fields in layered media composed of left-handed and right-handed materials*, MS in electrical and electronics engineering, Koc University, Istanbul, Turkey, 2008.
- [58] A.D. Polyanin and A.V. Manzhirov, *Handbook of Integral Equations*, Boca Raton: CRC Press, 1998.
- [59] J. Rissanen, "Modeling by shortest data description," *Automatica*, vol. 14, no. 5, pp. 465–471, Sept. 1978.
- [60] J. Rissanen, "Estimation of structure by minimum description length," *Circuits, Systems, and Signal Processing*, vol. 1, no. 3, pp. 395–406, Sept. 1982.
- [61] P.D. Grünwald, *The minimum description length principle*, The MIT Press, 2007.
- [62] H. Akaike, "A new look at the statistical model identification," *Automatic Control, IEEE Transactions on*, vol. 19, no. 6, pp. 716–723, Dec. 1974.
- [63] Clifford M. Hurvich and Chih-Ling Tsai, "A corrected akaike information criterion for vector autoregressive model selection," *Journal of Time Series Analysis*, vol. 14, no. 3, pp. 271–279, May 1993.
- [64] Petre Stoica and Yngve Selen, "Model-order selection," *IEEE Signal Processing Magazine*, vol. 21, no. 4, pp. 36–47, Jul. 2004.
- [65] L. G. Kraft, "A device for quantizing, grouping, and coding amplitude-modulated pulses," M.S. thesis, Massachusetts Institute of Technology, Massachusetts Institute of Technology. Dept. of Electrical Engineering, 1949.
- [66] Thomas M. Cover and Joy A. Thomas, *Elements of Information Theory*, Wiley-Interscience, 2006.

-
- [67] Steven M. Kay, *Fundamentals of Statistical Signal Processing, Volume I: Estimation Theory*, Prentice Hall, 1993.
- [68] R. Roy and T. Kailath, “Esprit-estimation of signal parameters via rotational invariance techniques,” *IEEE Trans. on ASSP*, vol. 37, no. 7, pp. 984–995, Jul. 1989.
- [69] K. M. Leung and Y. F. Liu, “Full vector wave calculation of photonic band structures in face-centered-cubic dielectric media,” *Physical Review Letters*, vol. 65, pp. 2646–2649, Nov. 1990.
- [70] Ze Zhang and Sashi Satpathy, “Electromagnetic wave propagation in periodic structures: Bloch wave solution of Maxwell’s equations,” *Physical Review Letters*, vol. 65, pp. 2650–2653, Nov. 1990.
- [71] K. M. Ho, C. T. Chan, and C. M. Soukoulis, “Existence of a photonic gap in periodic dielectric structures,” *Physical Review Letters*, vol. 65, no. 25, pp. 3152–3155, Dec. 1990.
- [72] J. D. Shumpert, *Modeling of Periodic Dielectric Structures (Electromagnetic Crystals)*, Ph.D. thesis, The University of Michigan, MI, 2001.
- [73] Y. Hua and T.K. Sarkar, “Generalized pencil-of-function method for extracting poles of an em system from its transient response,” *IEEE Trans. on Antennas and Propagation*, vol. 37, no. 2, pp. 229–234, Feb 1989.
- [74] M. I. Aksun and R. Mittra, “Choices of expansion and testing functions for the method of moments applied to a class of electromagnetic problems,” *Microwave Theory and Techniques, IEEE Transactions on*, vol. 41, no. 3, pp. 503–509, Mar. 1993.

-
- [75] F. Vanpoucke, M. Moonen, and Y. Berthoumieu, “An efficient subspace algorithm for 2-D harmonic retrieval,” *Acoustics, Speech, and Signal Processing, IEEE International Conference on*, vol. 4, pp. 461–464, 1994.
- [76] Y. Hua, “Estimating two-dimensional frequencies by matrix enhancement and matrix pencil,” *Signal Processing, IEEE Transactions on*, vol. 40, no. 9, pp. 2267–2280, Sept. 1992.
- [77] J. J. Sacchini, W. M. Steedly, and R. L. Moses, “Two-dimensional Prony modeling and parameter estimation,” *Signal Processing, IEEE Transactions on*, vol. 41, no. 11, pp. 3127–3137, Nov. 1993.
- [78] S. Rouquette and M. Najim, “Estimation of frequencies and damping factors by two-dimensional ESPRIT type methods,” *Signal Processing, IEEE Transactions on*, vol. 49, no. 1, pp. 237–245, Jan. 2001.
- [79] S. Oroskar, D. R. Jackson, and D. R. Wilton, “Efficient computation of the 2d periodic green’s function using the ewald method,” *Journal of Computational Physics*, vol. 219, no. 2, pp. 899–911, Dec. 2006.
- [80] P. P. Ewald, “Die Berechnung optischer und elektrostatischer Gitterpotentiale,” *Annalen der Physik*, vol. 369, no. 3, pp. 253–287, 1921.

Vita

EMiNE PINAR KARABULUT was born in Izmir, Turkey on March 10, 1981. She received her B.Sc. degree in Electrical and Electronics Engineering from Middle East Technical University, Ankara, Turkey, in 2004 and the M.Sc. degree in Electrical and Computer Engineering from Koc University, Istanbul, Turkey, in 2006. She is currently a Ph.D candidate supported by the TUBITAK Ph.D. scholarship, and working towards the Ph.D. degree in Electrical Engineering at Koc University, Istanbul, Turkey, as a research assistant. Her research interests include numerical methods for electromagnetics, computational aspects of layered media and periodic structures including photonic band-gap materials and metamaterials, and nano-photonics. She has four journal publications and several conference papers about layered media Green's functions, photonic crystals and MoM-based methods.